



UCTEA Turkish Chamber of Civil Engineers
TMMOB İnşaat Mühendisleri Odası

Turkish Journal of Civil Engineering

formerly
Teknik Dergi

Volume 36
Issue 1
January 2025



Turkish Journal of Civil Engineering (formerly Teknik Dergi) Publication Principles

Turkish Journal of Civil Engineering (TJCE), a non-profit, open access scientific and technical periodical of UCTEA Chamber of Civil Engineers, publishes papers reporting original research work and major projects of interest in the area of civil engineering. TJCE annually publishes six issues and is open to papers in English and Turkish. It should be noted that TJCE (formerly, Teknik Dergi/ Technical Journal of Turkish Chamber of Civil Engineers) is being published regularly for more than 30 years since 1990. Main publication principles of TJCE are summarized below:

1. Articles reporting original scientific research and those reflecting interesting engineering applications are accepted for publication. To be classified as original, the work should either produce new scientific knowledge or add a genuinely new dimension to the existing knowledge or develop a totally new method or substantially improve an existing method.
2. Articles reporting preliminary results of scientific studies and those which do not qualify as full articles but provide useful information for the reader can be considered for publication as technical notes.
3. Discussions received from the readers of the published articles within three months from publication are reviewed by the Editorial Board and then published together with the closing remarks of the author.
4. Manuscripts submitted for publication are evaluated by two or three reviewers unknown to the authors. In the light of their reports, final decision to accept or decline is taken by the Editorial Board. General policy of the Board is to get the insufficient manuscripts improved in line with the reviewers' proposals. Articles that fail to reach the desired level are declined. Reasons behind decisions are not declared.
5. A signed statement is taken from the authors, declaring that the article has not been published as a "journal article or book chapter". In case the Editorial Board is in the opinion that the article has already been published elsewhere with minor changes or suspects plagiarism or a similar violation of ethics, then not only that article, but none of the articles of the same authors are published.
6. Papers reporting works presented as conference papers and developed further may be considered for publication. The conference it was presented to is given as a footnote in the first page.
7. Additionally, a document signed by all authors, transferring the copyright to UCTEA Chamber of Civil Engineers is submitted together with the manuscript.



UCTEA Turkish Chamber of Civil Engineers
TMMOB İnşaat Mühendisleri Odası

Turkish Journal of Civil Engineering

formerly
Teknik Dergi

Volume 36
Issue 1
January 2025



UCTEA Turkish Chamber of Civil Engineers
TMMOB İnşaat Mühendisleri Odası

Necatibey St. No: 57, Kızılay 06440 Ankara, Turkey
Tel: +90.312.294 30 00 - Faks: +90.312.294 30 88
E-mail: imo@imo.org.tr - www.imo.org.tr

Publisher (Sahibi):

Nusret SUNA

On behalf of UCTEA Turkish Chamber of Civil Engineers

Administrative Officer (Yazı İşleri Müdürü):

Bülent TATLI

Volume 36 - Issue 1 - January 2025 (*Cilt 36 - Sayı 1 - Ocak 2025*)

Published bi-monthly. Local periodical. (*İki ayda bir yayınlanır, yerel süreli yayın*)

Date of Print: January 1, 2025 (*Baskı Tarihi: 1 Ocak 2025*)

Quotations require written approval of the Editorial Board.
(*Yayın Kurulunun yazılı onayı olmaksızın alıntı yapılamaz.*)

ISSN: 2822-6836

Turkish Journal of Civil Engineering (formerly Teknik Dergi) is indexed by

- Science Citation Index Expanded
- Scopus
- Journal Citation Reports / Science Edition
- Engineering Index
- Concrete Abstracts (American Concrete Institute)
- National Technical Information Service (US NTIS)
- CITIS
- Ulrich's International Periodical's Directory
- Google Scholar
- TRDizin

Turkish Journal of Civil Engineering (formerly Teknik Dergi) is a peer reviewed open access periodical publishing papers of original research and interesting practice cases. It addresses both the research community and the practicing engineers.

Printed by (Baskı):

Ankamat Matbaacılık San.

İvedik OSB. 1344. Sok. Yenimahalle / Ankara - Tel: 0.312.394 54 64

Sertifika No: 46700

Turkish Journal of Civil Engineering (formerly Teknik Dergi)

Editor-in-Chief:

Alper İLKİ

Editors:

İsmail AYDIN

Özer ÇİNİCİOĞLU

Metin GER

Gürkan Emre GÜRCANLI

Kutay ORAKÇAL

İsmail ŞAHİN

Özkan ŞENGÜL

Tuğrul TANKUT

Ufuk YAZGAN

Emine Beyhan YEĞEN

Drafting Language Check:

Metin GER

Polat GÜLKAN

İsmail ŞAHİN

Özkan ŞENGÜL

Mehmet UTKU

Editorial Assistant:

Çağlar GÖKSU AKKAYA

Secretary:

Cemal ÇİMEN

Advisory Board:

Prof. M. Aral, USA

Prof. D. Arditi, USA

Prof. A. Aydilek, USA

Prof. K. Beyer, Switzerland

Prof. N. Çatbaş, USA

Prof. M. Çetin, USA

Prof. M. Dewoolkar, USA

Prof. T. Edil, USA

Prof. K. Elwood, New Zealand

Prof. M. Fardis, Greece

Prof. G. Gazetas, Greece

Prof. P. Gülkan, Türkiye

Prof. J. Han, USA

Prof. I. Hansen, Netherlands

Prof. T. Hartmann, Germany

Prof. F. Imamura, Japan

Prof. T. Kang, Korea

Prof. K. Kusunoki, Japan

Prof. S. Lacasse, Norway

Prof. R. Al-Mahaidi, Australia

Prof. K. Özbay, USA

Prof. H. Özer, USA

Prof. S. Pampanin, Italy

Prof. A. J. Puppala, USA

Prof. M. Saatçioğlu, Canada

Prof. C. Santamarina, Saudi Arabia

Prof. S. Sheikh, Canada

Prof. E. C. Shin, South Korea

Prof. J. Smallwood, South Africa

Prof. M. Sümer, Türkiye

Dr. H. A. Şentürk, Türkiye

Dr. S. S. Torisu, Japan

Prof. E. Tutumluer, USA

Prof. M. Tümay, USA

Reviewers:

This list is renewed each year and includes reviewers who served in the last two years of publication.

Suman Kumar ADHIKARY	Niyazi Özgür BEZGİN Ozan BİLAL	Esra Ece ESELLER BAYAT	Esat Selim KOCAMAN Salih KOÇAK	Nuri SERTESER Emel SEYHAN
Kamil Bekir AFACAN Ayda Şafak AĞAR ÖZBEK	Turhan BİLİR Senem BİLİR MAHÇİÇEK	Müberra ESER AYDEMİR Tuğba ESKİŞAR TEFCİ Abdullah GEDİKLİ	Niyazi Uğur KOÇKAL Baha Vural KÖK Metin KÖKEN	Halil SEZEN Alper SEZER Metin SOYCAN
Elif AĞCAKOCA Bülent AKBAŞ	Barış BİNİCİ Jitendra BOTHARA	Ergun GEDİZLİOĞLU Mehmet GENES	Özgür KURÇ Ali Osman KURUŞÇU	Kurtuluş SOYLUK Serdar SOYÖZ
Sami Oğuzhan AKBAŞ Zülal AKBAY ARAMA Rifat AKBİYİKLİ	İlker BOZ İlknur BOZBEY Ali BOZER	Ahmet Talha GEZGİN Sadık Can GİRGİN Zehra Canan GİRGİN	Muhammed Emin KUTAY Akif KUTLU Merih KÜÇÜKLER	Tayfun Altuğ SÖYLEV Haluk SUCUOĞLU Erol ŞADOĞLU
Özge AKBOĞA KALE Sarven AKCELYAN Burcu AKÇAY ALDANMAZ	Mehmet Bakır BOZKURT Zafer BOZKUŞ Zekai CELEP	Michele GODIO Saadet Gökçe GÖK Tansu GÖKÇE	Abdullah KÜRKCÜ Erol LALE Jose LEMOS	Zekai ŞEN Burak ŞENGÖZ Gülüm TANIRCAN
Cihan Taylan AKDAĞ Bekir AKGÖZ Cem AKGÜNER	Halim CEYLAN Ömer CİVALEK Barlas Özden ÇAĞLAYAN	Serdar GÖKTEPE Semih GÖNEN Ali GÜL	Todd LITMAN Fağih MAARIF Müslüm Murat MARAŞ	Serhan TANYEL Mucip TAPAN Ergin TARI
Erkan AKPINAR Muhammet Vefa AKPINAR	Ferit ÇAKIR Melih ÇALAMAK Gülben ÇALIŞ	İlgin GÜLER M. Fethi GÜLLÜ Adil GÜLTEKİN	Ali MARDANI Kasım MERMERDAŞ Halit Cenan MERTOL	Yüksel TAŞDEMİR Ali Şahin TAŞLIGEDİK Kerem TAŞTAN
Atakan AKSOY Hafzaullah AKSOY Bekir AKTAŞ	Süheyla Pelin ÇALIŞKANELLİ Serdar ÇARBAŞ	Adil GÜLMGÜM Gürkan GÜNAY Taylan GÜNAY	Mehmet Murat MONKUL Nihat MOROVA Yetiş Şazi MURAT	Hasan TATLI Serdal TERZİ Berrak TEYMUR
Osman AKYÜREK Uğurhan AKYÜZ Alper ALDEMİR	Tevfik Kutay ÇELEBİOĞLU Ahmet Ozan ÇELİK	Lütfullah GÜNDÜZ Samet GÜNER Burcu GÜNEŞ	Fuad OKAY Didem OKTAY Derviş Volkan OKUR	Ömer Onur TEZCAN Mesut TİGDEMİR Salih TİLEYLİOĞLU
Cenk ALHAN Kayran ALTAN Gülşay ALTAY	Ozan Cem ÇELİK Hilmi Berk ÇELİKOĞLU Mecit ÇETİN	Oğuz GÜNEŞ Oğuz GÜNEŞ Mehmet Şükri GÜNEY	Meral OLTULU Şeref ORUÇ Okan ÖNAL	Onur Behzat TOKDEMİR Nabi Kartal TOKER Ali TOPAL
Muhammet Gökhan ALTUN Adlen ALTUNBAŞ	Elif ÇİÇEK Emin ÇİFTÇİ Hüseyin ÇİLSALAR	Aslı Pelin GÜRGÜN Ercan GÜRSER Tefarruk HAKTANIR	Akan ÖNALP Bihret ÖNÖZ Cihan ÖSER	Cenk TORT Hasan TOSUN Kamile TOSUN
Yalçın ALVER Mustafa M. ARAL Ahmet ARGEŞO	Erdal ÇOKÇA Turgay ÇOŞGUN Ayşe DALOĞLU	Soner HALDENBİLEN Ömer Faruk HALICI Hussein HAMADA	Türkan ÖZBALTA Yiğit ÖZÇELİK Gökhan ÖZDEMİR	FELEKİOĞLU Gökçe TÖNÜK Kemal Dingen TÖZER
Erdiç ARICI Yalın ARICI Musa Hakan ARSLAN	Yakup DARAMA Kutlu DARILMAZ Alper DEMİR	Ingo A. HANSEN Emre HASPOLAT Mustafa HATİPOĞLU	Zuhal ÖZDEMİR Murat ÖZEN Pelin ÖZENER	Nursu TUNALIOĞLU Gürsoy TURAN Kaan TÜRKER
Okan ARSLAN Deniz ARTAN İLTER Deepankar Kumar ASHISH	Cem DEMİR Hacımurat DEMİR Selçuk DEMİR	Lucas HOGAN Sabriye Banu İKİZLER Okan İLHAN	Hasan ÖZER Hakkı Oral ÖZHAN Hulusi ÖZKUL	Hasan Nuri TÜRKMEÑOĞLU Cüneyt TUZÜN Mehmet Baran ULAK
Ayşegül ASKAN GÜNDOĞAN Ali Osman ATAHAAN	Uğur DEMİR Ender DEMİREL Mehmet Cüneyd DEMİREL	Erol İSKENDER Medine İSPİR ARSLAN Recep İYİSAN	Hakim ÖZKUL Zeynep Huri ÖZKUL BİRGÖREN	Berna UNUTMAZ Mehmet UTKU Volkan Emre UZ
Hakan Nuri ATAHAAN Güzide ATASOY ÖZCAN Ali Osman ATEŞ	Murat DİCLELİ Seyyit Ümit DİKMEN Ahmet Anıl DİNDAR	Nuray Işık KABDAŞLI Mehmet Rifat KAHYAOĞLU	Aşkın ÖZOCAK Sadık ÖZTOPRAK Baki ÖZTÜRK	Mehmet Şeçil UZUNER Deniz ÜLGEN Mehmet Barış Can ÜLKER
Mustafa ATMACA Özgür AVŞAR Cem AYDEMİR	Gamze DOĞAN Mustafa DOĞAN Ünal DOĞAN	Özkan KALE Volkan KALPAKÇI Muhammed KAMAL	Gözde Başak ÖZTÜRK Onur ÖZTÜRK Mustafa ÖZUYSAL	Ali ÜNAY Cüneyt VATANSEVER Oral YAĞCI
Ersin AYDIN Serdar AYDIN Ülker Güner BACANLI	Marco DOMANESCHI Gökhan DÖK Cemalettin DÖNMEZ	Reza KAMGAR Hakan Alper KAMILOĞLU	Nilüfer ÖZYURT ZİHNİOĞLU Erhan Burak PANCAR	Ahmet YAKUT Seval PINARBAŞI Aslı YALÇIN
Mehmet Nurullah BALCI Selim BARADAN Eray BARAN	İsmail DURANYILDIZ Cengiz DÜNDAR Özgür EKİNCİOĞLU	Fatih KANTARCI Armağan Fatih KARAMANLI	Elifhan Filiz PİROĞLU Bora POLATSU Shehata E. Abdel RAHEEM	DAYIOĞLU Amel YAZICI Gökhan YAZICI Cem YENİDOĞAN
Türkan BARAN Efe BARBAROS Bekir Oğuz BARTIN	Serkan ENGİN Murat Altuğ ERBERİK Ali ERCAN	Saeid KAZEMZADEH AZAD Mustafa Kubilay KELEŞOĞLU	Mehmet SAATÇI Selman SAĞLAM Mehmet SALTAN	Mehmet YETMEZ Mehmet YILMAZ Berivan YILMAZER
Zeynep BAŞARAN BUNDUR İrfan BATUR	Şakir ERDOĞDU Esin ERGEN PEHLEVAN Uğur ERSOY	Veysel Şadan Özgür KIRCA Mehmet Anıl KIZILASLAN	Afşin SARITAŞ Altuğ SAYGILI Serdar SELAMET	POLAT Ercan YÜKSEL Ahmet Şahin ZAİMOĞLU
Cüneyt BAYKAL Mehmet BERLİGEN Önder Halis BETTEMİR Katrin BEYER	Yusuf Çağatay ERŞAN	Sercan SERİN	Abdullah Can ZÜLFİKAR	Abdullah Can ZÜLFİKAR

CONTENTS

RESEARCH ARTICLE

Comparative Analysis of Frequency Ratio, Logistic Regression and Deep Learning Methods for Landslide Susceptibility Mapping in Tokat Province on the North Anatolian Fault Zone (Turkey)..... 1
Ayhan BAŞALAN, Gökhan DEMİR

Earthquake Performance Analysis of a Masonry School Building's Retrofitted State by the Equivalent Frame Method 29
Vefa OKUMUS, Atakan MANGIR

Mixed Finite Elements for Higher-order Laminated Cylindrical and Spherical Shells..... 51
Yonca BAB, Akif KUTLU

A Critical Evaluation of the Coefficient Method, Capacity Spectrum Method and Modal Pushover Analysis for Irregular Steel Buildings in Seismic Zones..... 75
Vahid MOKARRAM, Mahmoud Reza BANAN, Mohammad Reza BANAN, Abdollah KHEYRI

TECHNICAL NOTE

Determination of Ungated Ogee Spillway Length so as to Pass Design Flood Safely..... 109
Tefaruk HAKTANIR

DISCUSSION

Seismic Assessment of Electrical Equipment in Power Substations: A Case Study for Circuit Breakers..... 123
Discussion by Eray BARAN

Comparative Analysis of Frequency Ratio, Logistic Regression and Deep Learning Methods for Landslide Susceptibility Mapping in Tokat Province on the North Anatolian Fault Zone (Turkey)

Ayhan BAŞALAN^{1*}
Gökhan DEMİR²



ABSTRACT

In the current investigation, a Geographic Information System (GIS) and machine learning-based software were employed to generate and compare landslide susceptibility maps (LSMs) for the city center of Tokat, which is situated within the North Anatolian Fault Zone (NAFZ) in the Central Black Sea Region of Turkey, covering an area of approximately 2003 km². 294 landslides were identified within the study area, with 258 (70%) randomly selected for modeling and the remaining 36 (30%) used for model validation. Three distinct methodologies were used to generate LSMs, namely Frequency Ratio (FR), Logistic Regression (LR), and Deep Learning (DL), using nine parameters, including slope, aspect, curvature, elevation, lithology, rainfall, distance to fault, distance to road, and distance to stream. The susceptibility maps produced in this study were categorized into five classes based on the level of susceptibility, ranging from very low to very high. This study used the area under receiver operating characteristic curve (AUC-ROC), overall accuracy, and precision methods to validate the results of the generated LSMs and compare and evaluate the performance. DL outperformed all validation methods compared to the others. Finally, it is concluded that the generated LSMs will assist decision-makers in mitigating the damage caused by landslides in the study area.

Keywords: Landslide susceptibility, GIS, NAFZ, frequency ratio, logistic regression, deep learning, Turkey.

Note:

- This paper was received on May 1, 2023 and accepted for publication by the Editorial Board on July 19, 2024.
- Discussions on this paper will be accepted by March 31, 2025.
- <https://doi.org/10.18400/tjce.1290125>

1 Tokat Gaziosmanpaşa University, Department of Civil Engineering, Tokat, Türkiye
ayhanbasalan@gmail.com - <https://orcid.org/0000-0002-1342-1336>

2 Ondokuzmayıs University, Department of Civil Engineering, Samsun, Türkiye
gokhandemir61@gmail.com - <https://orcid.org/0000-0002-3734-1496>

* Corresponding author

1. INTRODUCTION

The Earth is a living and dynamic inorganic entity akin to the living organisms that inhabit it. This dynamism of the Earth manifests itself in the form of natural events such as earthquakes, volcanic activity, tsunamis, floods, and landslides. Among these natural events, earthquakes are the most prevalent. It is well-established that landslides often occur as a result of earthquakes. In addition, landslides can be triggered by other natural processes, such as floods, intense and sudden rainfall, sudden changes in temperature, and human disruption of the natural equilibrium. Landslides significantly threaten life and property in regions characterized by steep topography and high precipitation [1, 2]. Landslides, a ubiquitous phenomenon worldwide, significantly impact the environment and economy in Turkey, particularly in densely populated residential areas, resulting in the loss of life and property. The recurrence and escalation of landslides into natural disasters in Turkey can be attributed to a combination of geological, climatic, and geographical factors and inadequate land management practices. In particular, the Eastern Black Sea region experiences intense landslides with devastating consequences [3]. Given the destructive nature of landslides, identifying and mapping landslide-prone areas is crucial for preventing losses. To this end, various studies, including the production of landslide hazard, risk, and susceptibility maps, have been conducted by researchers to identify and mitigate the potential consequences of landslides [4, 5, 6, 7, 8, 9]. Landslide hazard maps are cartographic representations that assess the probability of landslide occurrence in a specific location, accounting for spatial, temporal, and size-related factors. According to scholars, a practical landslide hazard map should encompass a comprehensive inventory assessment, a thorough analysis of the factors that lead to and trigger landslides, their spatial distribution, and information on their probability, nature, and magnitude [5, 10]. In addition, landslide risk maps comprise assessments of probable losses and destruction and financial and ecological consequences. To create accurate landslide hazard maps, it is necessary to have detailed information on the population, settlement, and economic conditions of the region. The production of such maps requires the expertise of experts from both social and natural sciences, as well as a multidisciplinary approach to planning and research [3, 11]. In addition, sensitivity maps are necessary for creating hazard and risk maps [12, 13]. LSMs are thematic representations that classify the relative susceptibility of areas to landslides in the future, considering factors that are believed to play a role in landslide formation in a specific location. In LSMs, research areas are typically divided into five classes of susceptibility, ranging from very low to very high [14, 15, 16]. In recent years, the study of landslide susceptibility has gained significance because it serves as a means of minimizing the damage caused by landslides and providing guidance for land-use planning [5, 17]. Advances in GIS, remote sensing techniques, computer technology, and software have enabled the storage and statistical analysis of large amounts of data, leading to increased use of artificial intelligence and non-empirical statistical methods in landslide susceptibility assessments. These studies are precious for disaster prevention and mitigation [18, 19]. Furthermore, the prevalence of these studies has increased in recent years because of technological advancements, which suggests a higher level of sophistication in this field. This study aimed to generate and contrast high-resolution LSMs of Tokat province, which is located in the North Anatolian Fault Zone (NAFZ), by employing FR, LR, and DL techniques in a GIS environment. The absence of previous research on landslide susceptibility mapping in the provincial center of Tokat and the area's location within the NAFZ provided the impetus for this study to be conducted in the region.

2. STUDY AREA

The Turkish province of Tokat is geographically situated within the Central Black Sea Region on the NAFZ, a seismically active zone that is notorious for frequently generating devastating earthquakes. The population of the central district of Tokat, which includes 12 districts, including the city center, was recorded as 204.907 in 2022 [20]. The topography of the provincial capital is characterized by cliffs and hills in the east-west direction and mountains and hills with gentle slopes in the north direction. The district center of the province, which spans an area of approximately 2003 km², is located between 36°25' and 37°00' east longitude and 39°55' and 40°35' north latitude (Figure 1). Tokat is a transitional climate between the Black Sea and Central Anatolian steppe. While the northern regions of the study area exhibit the characteristics of the Black Sea climate, the southern regions display the characteristics of the Central Anatolian Steppe. The elevation of the study area above sea level ranged between 585 m and 2079 m, and the maximum slope value was recorded as 80.3°. The Yeşilirmak River traverses the study area, and landslides in the region can be induced by factors such as unanticipated earthquakes, anthropogenic activities, changes in groundwater level, or a combination of these factors. Field observations have shown that landslides predominantly occur in thick, weathered topsoil areas.

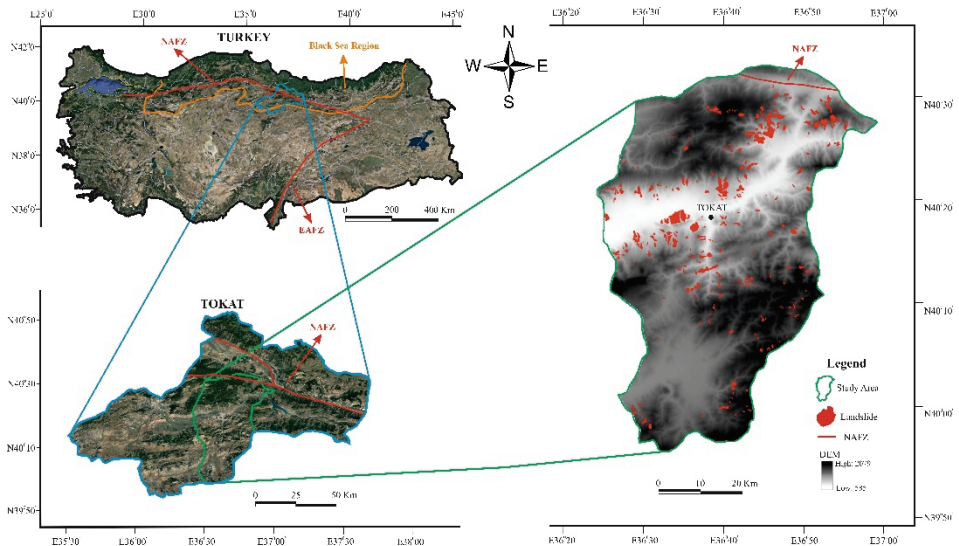


Figure 1 - Location map of the study area

3. MATERIALS AND METHODS

The process of assessing landslide susceptibility is highly dependent on the compilation of reliable and relevant data and parameters related to landslides in the study area. Thus, any errors or deficiencies in the data and parameters used can significantly affect the accuracy of the resultant LSMs [13, 21]. Several techniques have been developed in recent years to create landslide susceptibility and hazard maps using statistical models and GIS tools. Some studies have used statistical models such as logistic regression, bivariate and multivariate analysis,

and probabilistic models such as frequency ratio and weight of evidence. In addition, other approaches, including analytical hierarchy process, index of entropy model, certainty factor model, artificial neural network model, spatial multicriteria decision analysis approach, fuzzy logic and neuro-fuzzy, deep learning, decision-tree methods, and support vector machine model have been applied for landslide susceptibility mapping [22, 23, 24, 25, 26, 27]. Previous research on landslide susceptibility mapping was reviewed as part of this study to inform the selection of relevant data and parameters [19, 24]. This review comprehensively discusses the data, parameters, and methodologies integral to creating LSMs [28, 29, 30]. The present study adopted a combined approach incorporating the widely used FR and LR statistical techniques and the DL machine learning algorithm to produce LSMs. A schematic representation of the methodology used in this study is shown in Figure 2. This flowchart shows the sequence of procedures and processes used throughout the study.

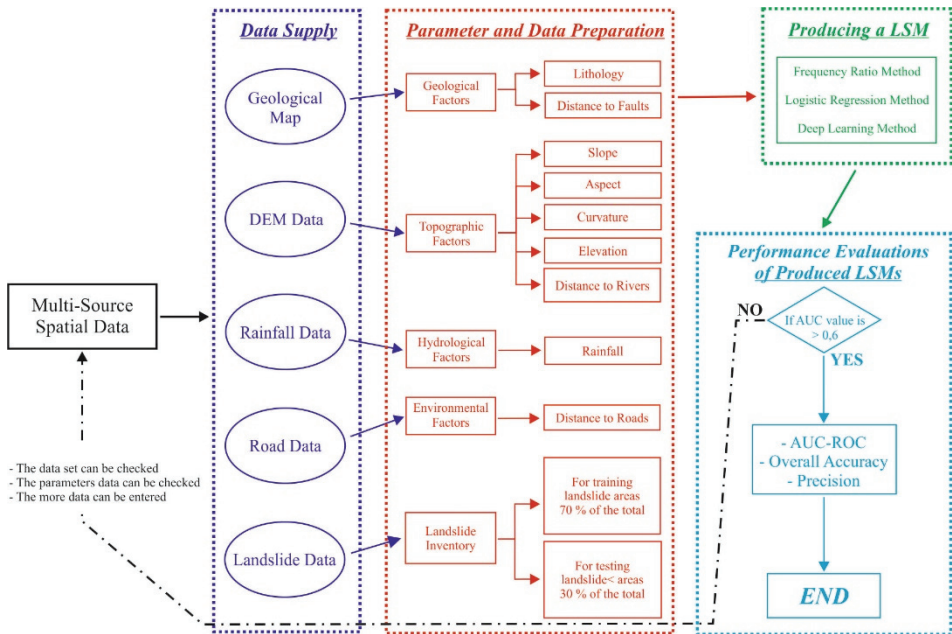


Figure 2 - Workflow chart of the study

3.1. Landslide Inventory

Landslide inventory maps represent the location of landslides, typically containing details on the type, date, and location of landslides [24]. These maps are crucial for creating accurate inventory, landslide, hazard, and risk maps. Compiling a comprehensive landslide inventory is essential in evaluating previous landslide assessment maps [31]. Various sources, such as literature, field studies, digital maps, aerial photographs, and satellite images, can be used to gather information for the landslide inventory. In the present research, a combination of field investigations (Figure 3a, 3b, 3c, and 3d), aerial photographs (Figure 3e, 3f, and 3g), and printed and digital maps developed by the Mineral Research and Exploration Department were employed to acquire the landslide inventory for the study region [32]. Because of the

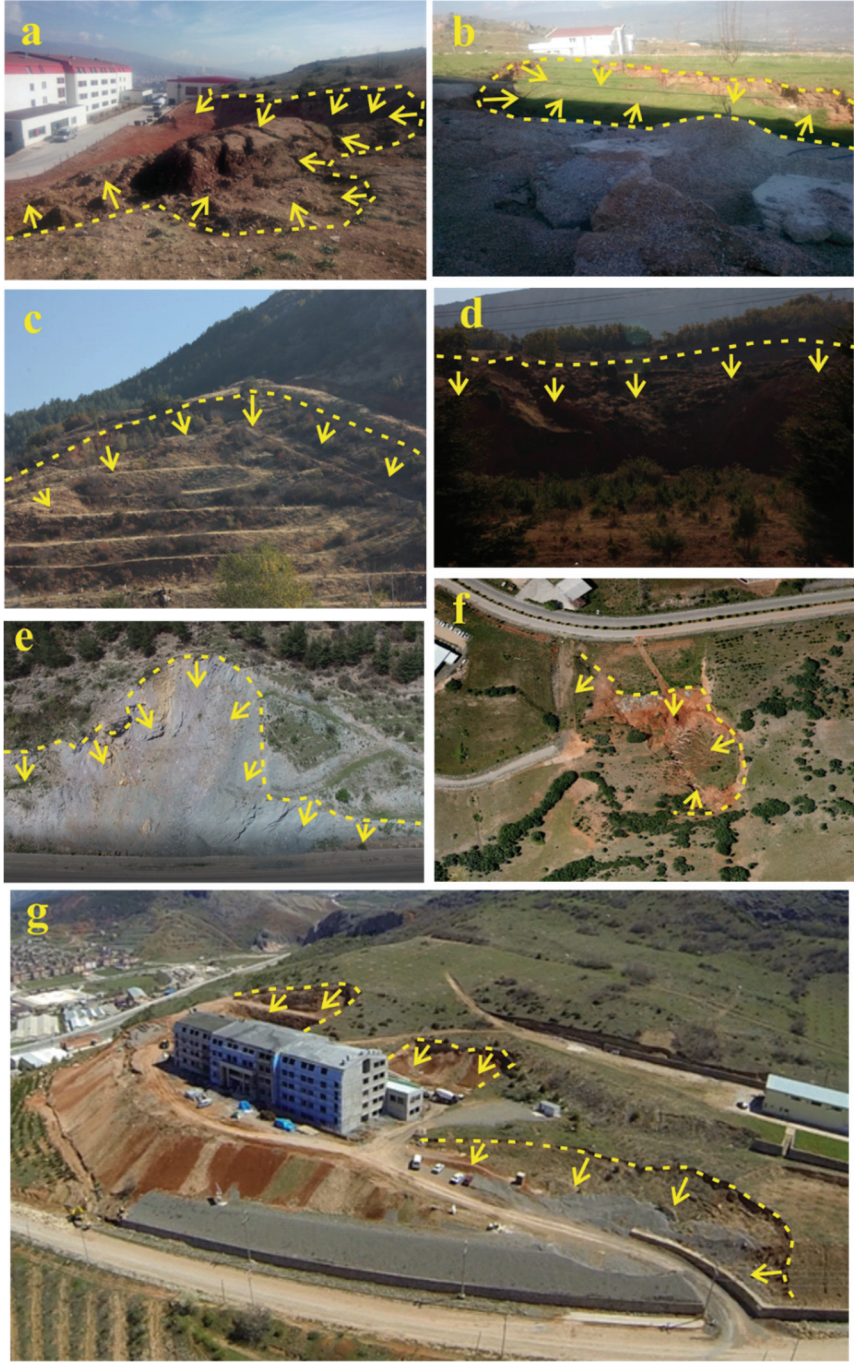


Figure 3 - Images of some landslides in the study area: a, b, c, and d images, e, f, and g aerial images (arrows show the direction of movement of landslides)

collection of historical landslide data, interpretation of remote sensing images, and field survey, 294 landslides were identified within the study area (Figure 4). According to the data, these 294 landslide areas comprise 482.649 pixels (12.5 m x 12.5 m) and cover approximately 3.76% of the study area. Approximately 70% of the landslide areas (314.019 pixels) were used for analysis in the applications, whereas the remaining 30% (141.630 pixels) were used to test the performance of the generated landslide susceptibility models. The landslides allocated for analysis and performance testing were chosen at random.

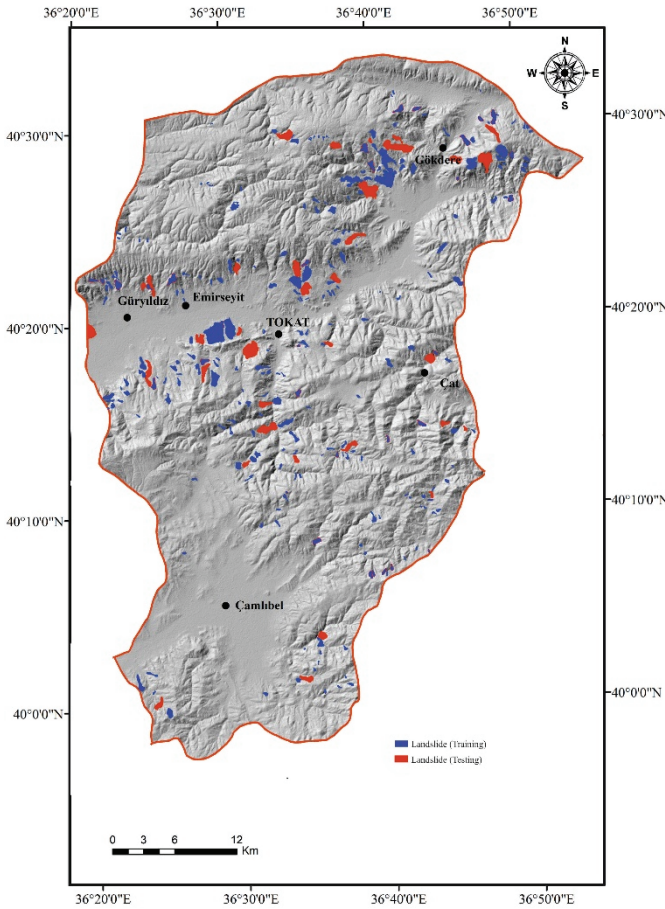


Figure 4 - Landslide inventory map of the study area

3.2. Data Preparation

Determining factors affecting landslides is mainly driven by their significance to the incidence of landslides in a particular region and the accessibility of related data [17, 33]. The factors chosen for GIS-based research should be operational, comprehensive, irregular, measurable, and non-redundant [15, 34, 35]. This study produced nine data layers based on a review of relevant literature and field investigations to identify the significant factors

influencing landslide occurrences within the study area. The generated data layers included slope, aspect, curvature, elevation, rainfall, lithology, distance to faults, distance to roads, and distance to streams (Figure 5). The slope is one of the most critical parameters in forming landslides because of its high level of influence and ease of mapping [36, 37, 38]. Researchers often use slope as a parameter for generating LSMs. The slope is defined as the angle of inclination of a surface relative to the horizontal plane, expressed in degrees [39]. Alterations in the slope and the destabilization of materials on a slope are considered the most fundamental factors leading to landslides [7]. Nine distinct slope categories ranging from 0° to 80.3° were established for the study area, and it was observed that most slopes fell within the 0° to 30° range (Figure 5a). The parameter aspect holds significant importance in landslide susceptibility research, as it denotes the orientation of the land surface and can be characterized by the direction of the tangent plane at any given location on the surface [40, 41]. In the study area, the values of the aspect were segregated into nine distinct directional categories. The study area had the most significant percentage of area facing the east direction, 12.68%, and the most minor area facing the north direction, 9.76% (Figure 5b). Curvature, defined as the rate at which the angle or direction of the land slope changes in a particular, is found to reach high and wide-range values in narrow areas [34]. The map depicting the curvature of the study area was categorized into three classes: flat, concave, and convex. A significant proportion of the study area was classified as concave (34.47%), followed by convex (33.77%), and flat (31.76%) (Figure 5c). Elevation, another commonly used parameter in landslide susceptibility studies [16, 42, 43], was found to vary between 575 m and 2079 m in the study area. It has been observed that landslides occur at almost all elevation values but with a higher concentration between 755 m and 1410 m (Figure 5d). Rainfall is widely recognized as a trigger for landslides on slopes [44, 45]. The annual average rainfall values in the study area vary between 765 and 1115 mm. It has been observed that landslides occur at almost all rainfall values, with a higher concentration observed between 765 mm and 899 mm (Figure 5e). The lithology parameter, which refers to the physical properties of rock units such as color, texture, and grain size, is commonly used in landslide susceptibility studies [46, 47, 48]. In this study area, lithology classes were divided into eight different classes, and landslides were observed in all units except the alluvial unit. It was also observed that most landslide areas were concentrated in the Tokat metamorphics (Pztm) and Haydaroğlu formation (Teh) (Figure 5f). In the landslide susceptibility analysis, the distance from faults is a crucial parameter. This is because such proximity may result in rock fragmentation, adversely impacting slope stability [49, 50]. Structural elements can weaken the surrounding materials and increase the likelihood of landslides. Similarly, proximity to roads is also considered a significant factor in landslide susceptibility analysis, as they can cause loss of heel support or additional load on sensitive slopes [23, 51, 52, 53, 54]. The degree of saturation of slopes, which is determined by the distance between slopes and streams, is a critical factor in landslides [33]. Therefore, the distance to faults, roads, and streams are deemed significant parameters in evaluating landslide susceptibility and are commonly referred to as stream density, distance to the drainage network, and drainage density [55]. Buffer analysis created maps for these parameters at 100 m intervals. According to the obtained data, it has been observed that landslide areas are concentrated in areas farther than 900 meters away from the three parameters mentioned above (Figure 5g, 5h, and 5i).

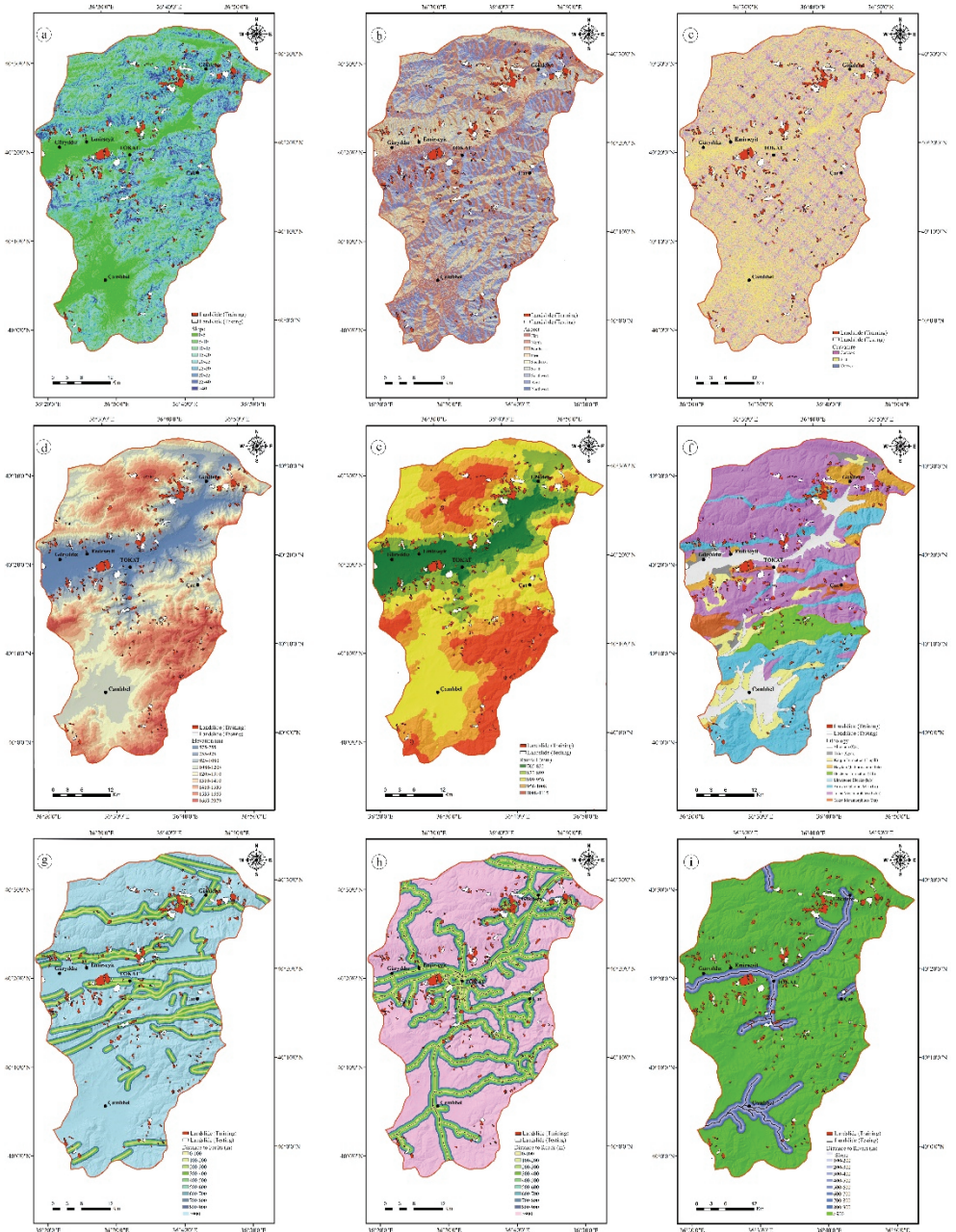


Figure 5 - Landslide conditioning factors: (a) slope, (b) aspect, (c) curvature, (d) elevation, (e) rainfall, (f) lithology, (g) distance to faults, (h) distance to roads and (i) distance to streams

3.3. Landslide Susceptibility Assessment Methods

This study employed FR, LR, and DL methods for landslide susceptibility assessment.

3.3.1. Frequency Ratio Method

The FR method, which computes the observation frequency of parameter sublayers within landslide zones, facilitates the objective weighting of parameter maps and their respective sublayers while estimating areas prone to landslide susceptibility. Using the FR method, the sublayers of parameter maps within the study area can be correlated with the sublayers of actual landslide areas. This approach relies on a probability model that evaluates the likelihood of a particular event occurring [56, 57, 58, 59]. The following is the formula for this method (Eq. 1);

$$FR = \frac{PLO}{PIF}, \quad (1)$$

PLO refers to the percentage of each substrate affecting landslides in the formula, and PIF refers to the percentage of each substrate causing landslides in the parameter map. The parameter maps were assigned weights based on the FR determined using the above formula [60, 61].

The summation of the frequency ratio values belonging to each factor category was used to calculate the landslide susceptibility index (LSI), as expressed in equation 2;

$$LSI = \sum_{i=1}^n FR, \quad (2)$$

Because of reclassifying the LSI map using the equal interval methodology in GIS, the study region was partitioned into five susceptibility categories: very low, low, moderate, high, and very high. Weighted parameter maps were generated by assigning lower values to areas with lower landslide susceptibility and higher values to regions with higher susceptibility. These maps were then combined to produce an LSM. To determine the final state of the LSM, these values were grouped into classes of equal intervals [62].

3.3.2. Logistic Regression Method

Regression analysis is a statistical method that involves explaining or understanding a variable based on one or more other variables. The variable being explained is referred to as the dependent or response variable, while the different variables used to predict or explain the response are known as independent variables or predictors. LR is a statistical technique that researchers and statisticians extensively employ for analyzing binary and proportional response data [63]. In the production of LSMs, LR, a multiple logistic regression method, is commonly used [64]. LR permits the development of a multivariate regression model that establishes a relationship between a dependent variable and multiple independent variables. The dependent variable can be binary, whereas the independent variables may assume

interval, binary, or categorical forms [65, 66]. When performing the LR analysis, the numerical values of the dependent variable should be 0 or 1. The LR coefficients obtained from the analysis can be used to generate independent variables. The relationship between the data in the LR analysis is expressed by the formula provided below [23, 66, 67];

$$p = \frac{1}{(1+e^{-z})} = \frac{e^z}{1+e^z} \quad (3)$$

In the formula, the symbol 'p' represents the probability of a landslide occurrence, which assumes the form of an S-shaped curve ranging from 0 to 1. This probability is estimated using LR;

$$z = \beta_0 + \beta_1x_1 + \beta_2x_2 + \dots + \beta_n \quad (4)$$

and the equation, as mentioned above, yields the value of 'z'. In this equation, β_0 represents the model constant value, $\beta_1, \beta_2, \dots, \beta_n$ represent the coefficients of the independent variables, and x_1, x_2, \dots, x_n are the independent variables. The equation's dependent variable 'z' corresponds to the landslide condition. The model reveals a landslide (1) and no landslide (0) on the independent variables of the landslide.

3.3.3. Deep Learning Method

DL is a subfield of machine learning that leverages multi-layered data representations, commonly using artificial neural networks, to attain cutting-edge performance in tasks such as image classification, object detection, speech recognition, and document classification [68]. DL incorporates self-learning artificial neural networks, called deep learning neural networks (DNNs) or stacked artificial neural networks [69], to process and analyze data through multiple layers. The depth of these networks, represented by the number of hidden layers, distinguishes DNNs from other types of neural networks, such as multi-layer perceptron networks. The complexity of DNNs is characterized by the intricate patterns in which information flows throughout the network, as evidenced by the increasing number of hidden layers and nodes in more advanced architectures. Despite this complexity, the fundamental concept of DNNs remains unchanged. Deep neural networks (DNNs) possess a unique characteristic known as feature hierarchy, a hierarchical structure of increasing complexity and abstraction. This feature enables DNNs to handle vast, high-dimensional datasets with billions of parameters passing through nonlinear functions. As a result, unlike traditional machine learning algorithms, DNNs can perform automatic feature extraction without human intervention. Given that feature extraction is a task that can take years for data scientist teams to accomplish, DNNs provide a means to circumvent the bottleneck of limited expertise and enhance the capabilities of small data science teams, which inherently do not scale. Over time, various types of neural networks have been developed, such as convolutional neural networks (CNNs) and recurrent neural networks (RNNs), which are thought to emulate the human visual system and interpret sequential data. Despite their complexity, these networks can be considered variations of the same concept, as evidenced by the fact that all types of neural networks can use the same learning algorithms, such as

gradient descent using backpropagation [70, 71, 72]. The present research uses the obtained data to employ a deep neural network (DNN) architecture for text classification.

3.3.3.1. Deep neural Networks (DNN)

The networks used in this system are similar to the human brain's neurons (Figure 6). When a stimulus is presented, the networks undergo a process. The networks can be connected and signed or unconnected and unsigned but are generally organized into layers. To perform a task, the network system must process data through the layers between the input and output. The depth of the network, or the number of layers required for processing, increases with the complexity of the task. A deep neural network is beneficial when it is necessary to replace human labor with autonomous processes without compromising efficiency. These types of networks have several real-world applications across various fields [70, 71, 72, 73].

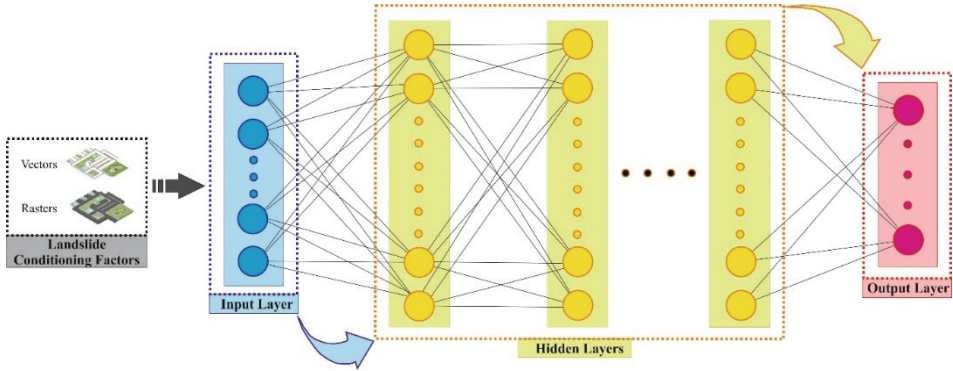


Figure 6 - DL architecture

4. RESULTS

4.1. Results of the Frequency Ratio Method

The frequency ratio value represents the degree of association between the incidence of landslides and the factors under consideration. After creating maps for all the analyzed parameters, the FR formula was used to determine the FR values for the sublayers of each parameter. The data obtained for the sublayers are tabulated in Table 1 and presented visually.

Table 1 - Frequency ratio analysis of landslide conditioning factors

Parameters	Pixel Number of Total Areas	Ratio (% PIF)	Pixel Number of Landslide Areas	Ratio (% PLO)	FR % (PLO/PIF)
Slope (°)	0-5	1.783.389	16.991	4,98	0,359
	5-10	2.104.818	51.534	15,11	0,921
	10-15	1.941.286	59.845	17,55	1,161

Comparative Analysis of Frequency Ratio, Logistic Regression and Deep Learning ...

	15-20	2.161.598	16,84	66.239	19,42	1,153
	20-25	1.834.237	14,29	56.117	16,46	1,152
	25-30	1.371.765	10,69	41.253	12,1	1,132
	30-35	9483.59	7,39	28.170	8,26	1,118
	35-40	524.359	4,08	15.804	4,63	1,135
	>40	167.209	1,30	5.065	1,49	1,146
Aspect						
	Flat	1.508.203	11,75	31.152	9,13	0,777
	North	1.252.408	9,76	36.161	10,60	1,086
	Northeast	1.274.841	9,93	37.461	10,99	1,107
	East	1.627.760	12,68	47.100	13,81	1,089
	Southeast	1.535.651	11,96	43.477	12,75	1,066
	South	1.434.310	11,17	37.957	11,13	0,996
	Southwest	1.325.321	10,32	33.118	9,71	0,941
	West	1.533.674	11,95	39.712	11,65	0,975
	Northwest	1.344.852	10,48	34.880	10,23	0,976
Curvature						
	Concave	2.637.812	20,55	74.056	21,72	1,057
	Flat	7.529.587	58,66	192.899	56,57	0,964
	Convex	2.669.621	20,80	74.064	21,72	1,044
Elevation (m)						
	585-755	1.181.322	9,20	27.549	8,08	0,878
	755-925	1.080.062	8,41	72.923	21,38	2,542
	925-1080	1.161.953	9,05	76.338	22,39	2,474
	1080-1205	2.168.970	16,90	52.517	15,40	0,911
	1205-1310	2.038.691	15,88	35.687	10,46	0,659
	1310-1410	1.702.050	13,26	34.597	10,15	0,765
	1410-1535	1.494.245	11,64	18.123	5,31	0,456
	1535-1665	1.423.232	11,09	13.219	3,88	0,350
	1665-2079	586.495	4,57	10.066	2,95	0,646
Rainfall (mm)						
	765-832	1.634.940	12,74	55.027	16,14	1,267
	832-899	1.769.073	13,78	121.075	35,50	2,576
	899-956	4.109.114	32,01	86.352	25,32	0,791
	956-1008	2.782.311	21,67	46.057	13,51	0,623
	1008-1115	2.541.582	19,80	32.508	9,53	0,481
Lithology						
	Qal	1.295.659	10,09	0	0	0
	Teh	715.302	5,57	64.139	18,81	3,377
	Tmplb	936.363	7,29	12.689	3,72	0,510
	Qym	215.382	1,68	602	0,18	0,107

Kb	69.8017	5,44	18.741	5,50	1,011
Ka	3.172.178	24,71	81.432	23,88	0,966
Pz _{tm}	5.420.494	42,23	153.683	45,07	1,067
Pz _t	383.625	2,99	9.733	2,85	0,953
Distance to faults (m)					
0-100	436.276	3,40	21.707	6,37	1,874
100-200	441.502	3,44	20.452	6,00	1,744
200-300	445.504	3,47	18.736	5,49	1,582
300-400	440.711	3,43	17.660	5,18	1,510
400-500	416.917	3,25	15.148	4,44	1,366
500-600	390.348	3,04	13.681	4,01	1,319
600-700	372.137	2,90	12.708	3,73	1,286
700-800	359.890	2,80	12.458	3,65	1,304
800-900	350.501	2,73	13.034	3,82	1,399
>900	9.183.234	71,54	195.434	57,31	0,801
Distance to roads (m)					
0-100	731.747	5,70	22.022	6,46	1,133
100-200	658.299	5,13	19.442	5,70	1,111
200-300	618.216	4,82	18.064	5,30	1,100
300-400	586.494	4,57	17.033	4,99	1,092
400-500	559.658	4,36	17.782	5,21	1,195
500-600	534.901	4,17	17.492	5,13	1,230
600-700	508.530	3,96	17.055	5,00	1,263
700-800	485981	3,79	15.917	4,67	1,232
800-900	465.282	3,62	13.976	4,10	1,133
>900	7.687.912	59,89	182.236	53,44	0,892
Distance to streams (m)					
0-100	195.815	1,53	931	0,27	0,176
100-200	189.891	1,48	1.458	0,43	0,291
200-300	185.427	1,44	2.090	0,61	0,424
300-400	180.924	1,41	2.444	0,72	0,511
400-500	177.600	1,38	2.676	0,78	0,565
500-600	176.103	1,37	2.498	0,73	0,533
600-700	175.520	1,37	2.689	0,79	0,577
700-800	175.228	1,37	3.010	0,88	0,642
800-900	175.167	1,36	3.252	0,95	0,699
>900	11.205.345	87,29	31.9971	93,83	1,075

The study area exhibits high occurrences of landslides in slope classes between 5° and 25°. Lower slope classes are generally expected to have lower landslide frequencies because of reduced shear stresses. The gentle slopes of the study area may be susceptible to landslides

because of the rapid melting of snow. An analysis of the slope aspect reveals that slopes facing east and southeast are particularly vulnerable to frequent landslides. Flat areas experience high landslide frequencies in terms of curvature, while the intensity of landslides is highest between 755 and 1080 m elevation, followed by 1205 to 1410 m elevation. Precipitation falling in the 832-956 mm range is associated with high landslide intensity. The evaluation of distances to faults, rivers, and roads indicates that distances exceeding 900 m significantly correlate with landslide occurrence. After the computation of FR values, the parameter maps underwent reclassification within the GIS software using its corresponding modules. This results in the generation of updated classified parameter maps. The Raster Calculator process was used to create a novel LSM. After its creation, the map, as mentioned above, was subjected to a reclassification process, ultimately resulting in developing a new map representing landslide susceptibility in the study area using the FR method (Figure 7). The LSM generated using the FR method categorized 26.40% of the study area as having a very low susceptibility to landslides.

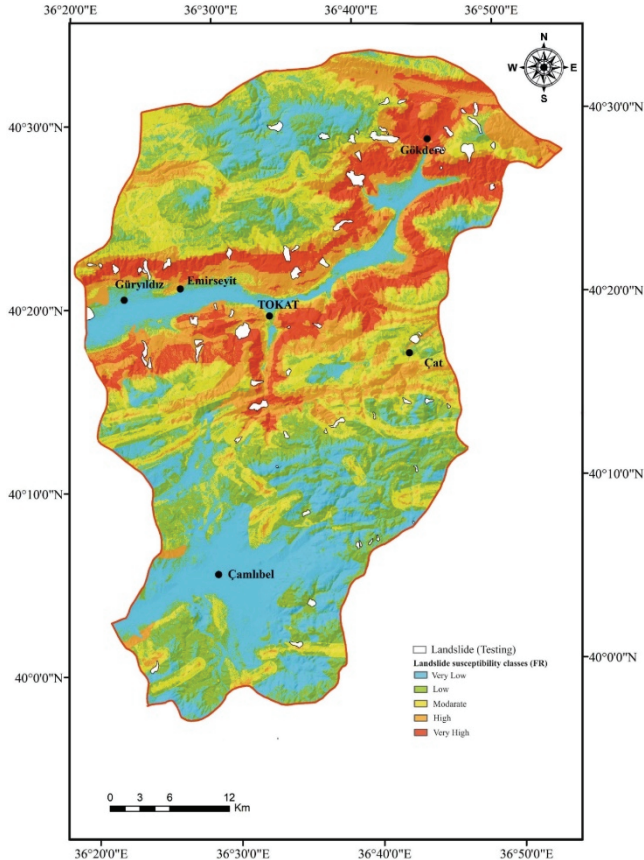


Figure 7 - Landslide susceptibility map produced by FR method

The remaining area is classified into five categories: very low, low, medium, high, and very high susceptibility. The low, medium, and high susceptibility categories cover 23.92%, 20.72%, and 16.93% of the study area, respectively. The very high susceptibility category comprises 12.03% of the total study area.

4.2. Results of the Logistic Regression Method

The present study employed the LR method as a secondary approach to generate LSMs. The LR method uses pre-existing parameter maps to create such maps. To develop the LSM via the LR method, the data of landslides and parameters obtained through the FR method were transformed into "TXT (ASCII)" format using GIS software modules. The converted data were transferred to the relevant GIS software for LR analysis and then back to raster format. Parameter data and landslide data were standardized in the range 0-1 using the "FUZZY" module and introduced into the GIS software. The data were then analyzed using the "LOGISTICREG" module in the GIS software to generate an LR equation and statistical data. The LR equation and related data are presented in Table 2. Table 2 displays the pseudo- R^2 value, which indicates the model's goodness of fit concerning the dataset in the logit model [74]. A pseudo R^2 value greater than 0.2 is considered a satisfactory match. Table 3 shows the LR equation that includes the regression coefficient and individual coefficients for each parameter to generate LSMs using the LR method.

Table 2 - Coefficients in the LR equation

Variables	Regression Coefficients
Regression Coefficient	3,8577
Aspect	3,9821
Curvature	1,5355
Distance to fault	0,5618
Distance to road	1,9804
Distance to stream	-0,2214
Elevation	-3,5103
Lithology	-1,2303
Rainfall	-0,1821
Slope	0,3579

Table 3 - Statistical summaries of the LR method

Statistics	Value
Total number of pixels	12.837.020
-2logL0	297.093,9400
-2log (possible)	162.258,7882
Goodness of fit	1.086.878,7391
Pseudo R^2	0,4538

The coefficients were aggregated using relevant modules in other GIS software to apply to previously generated parameters. The Raster Calculator was employed to create a fresh LSM, which was reclassified to obtain the final LSM of the study area using the LR method (Figure 8). The LSM generated using the LR method was categorized into five classes: very low, low, moderate, high, and very high susceptibility, similar to the FR method. The resultant LSM obtained through the LR method revealed that 28.06% of the study area was categorized as having very low susceptibility, 24.46% as having low susceptibility, 22.07% as having moderate susceptibility, 16.56% as having high susceptibility, and 8.85% as having very high susceptibility.

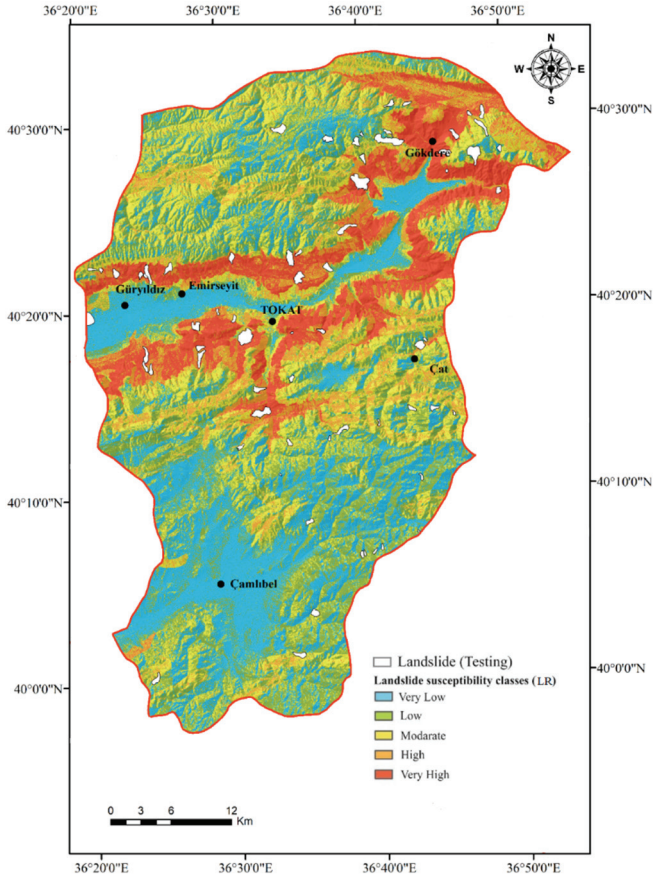
































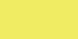




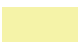





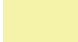









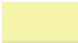




















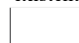


Figure 8 - Landslide susceptibility map produced by LR method

4.3. Results of Deep Learning Method

Within the scope of this study, an LSM of the study area was generated using the DNN algorithm, a DL architecture, in the final phase employing the DL method (Figure 6). The open-source ML software Weka 3.9.5 was used to execute the algorithm. The landslide and parameter map data that were employed to create LSMs through the FR and LR methods

Table 4 - Classification of landslides with the colors obtained for the parameters and the numbers assigned for analysis

PARAMETERS	FEATURES OF PARAMETERS									
Slope (°)	0-5	5-10	10-15	15-20	20-25	25-30	30-35	35-40	>40	
										
	1	2	3	4	5	6	7	8	9	
Aspect	Flat	N	NE	E	SE	S	SW	W	SW	
										
	1	2	3	4	5	6	7	8	9	
Curvature	Concave	Flat	Convex							
										
	1	2	3							
Elevation (m)	585-755	755-925	925-1080	1080-1205	1205-1310	1310-1410	1410-1535	1535-1665	1665-2079	
										
	1	2	3	4	5	6	7	8	9	
Rainfall (mm)	765-832	832-899	899-956	956-1008	1008-1115					
										
	1	2	3	4	5					
Lithology	Qal	Qym	Tmplb	Teh	Kb	Ka	Pztm	Pzt		
										
	1	2	3	4	5	6	7	8		
Distance to Faults (m)	0-100	100-200	200-300	300-400	400-500	500-600	600-700	700-800	800-900	>900
										
	1	2	3	4	5	6	7	8	9	10
Distance to Roads (m)	0-100	100-200	200-300	300-400	400-500	500-600	600-700	700-800	800-900	>900
										
	1	2	3	4	5	6	7	8	9	10
Distance to Streams (m)	0-100	100-200	200-300	300-400	400-500	500-600	600-700	700-800	800-900	>900
										
	1	2	3	4	5	6	7	8	9	10
Landslide	CLASS									
	Existent	No existent								
										
	1	0								

were also used in the DL method. To generate the LSM using the DL method, the landslide and parameter map data developed in the CBS software were initially transformed into the "TXT" format using relevant modules. The converted "TXT" data consists of a total of 12.837.020 pixels with a size of 12.5 m x 12.5 m, starting from the upper left corner of the study area and ending in the lower right corner for each parameter, including the selected 70% landslides for the application. The data were then processed in SPSS statistical software to create a dataset with each parameter's "TXT" data in a single column to be transferred to Weka for analysis. For each subparameter, numeric values ranging from 1 to 10 and class values of "1" if there is a landslide and "0" if there is no landslide were assigned to create the dataset (Table 4).

Table 5 - Classifier functions organized in the D14jMlpClassifier submodule

No	Parameters	Functions
1	layer specification	1 weka.dl4j.layers.Layer
2	Preview zoo model layer specification in GUI	False
3	number of epochs	10
4	instance integrator	Default
5	network configuration	Neural Net Configuration
6	set the iteration listener	Epoc Listener
7	zooModel	Custom Net
8	attribute normalization	Normalize training data
9	data queue size	0
10	resume	False
11	Preserve filesystem cache	False
12	batchSize	100
13	debug	False
14	doNotCheckCapalities	False
15	numDecimalPlaces	2
16	seed	1

Table 6 - Summary of DL analysis data

Summary		
Correctly Classified Examples	12.323.846	% 96.0024
Average Absolute Error	0.0727	
Mean Square Root of Errors	0.1942	
Relative Absolute Error	% 94,7029	
Relative Root Square Error	% 99,129	
Total Number of Samples	12.837.020	

The edited dataset was then transferred to Weka software to perform the DL analysis. The classifier functions of the D14jMlpClassifier sub-module were edited before DL analysis (Table 5). The software then produced the landslide susceptibility data in "TXT" format using the DL method (Table 6). The collected data underwent further processing using SPSS software before being imported into GIS software to produce an updated LSM. This newly generated map was subsequently subjected to reclassification procedures using the DL method, which divided its five distinct categories: very low, low, moderate, high, and very high susceptibility (Figure 9).

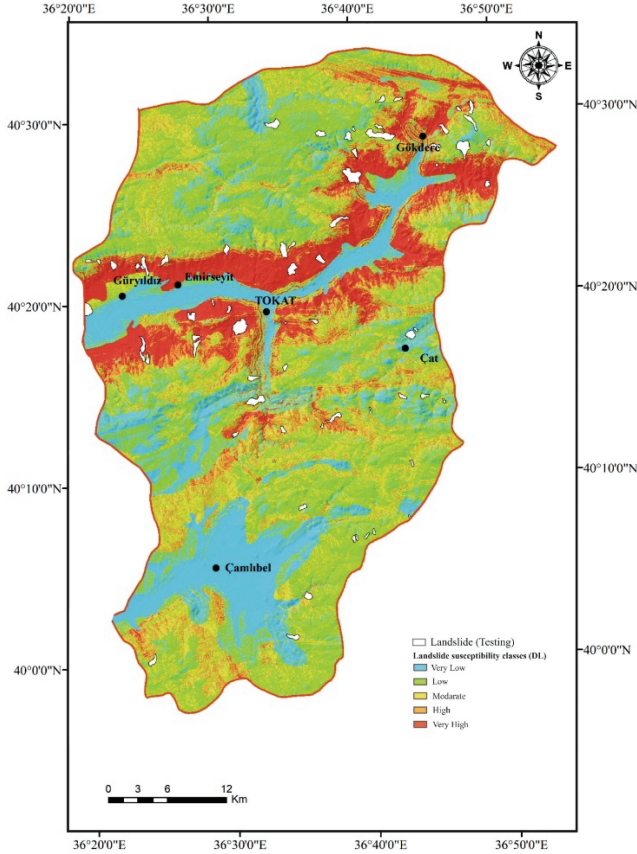


Figure 9 - Landslide susceptibility map produced by LR method

As depicted in Figure 9, the resulting susceptibility map revealed that 28.19% of the total area under study was categorized as very low susceptibility. In comparison, 34.24% was classified as low susceptibility, 20.07% as moderate susceptibility, 9.98% as high susceptibility, and 7.53% as very high susceptibility.

4.4. Performance Evaluation Methods

It has been claimed that a landslide susceptibility map (LSM) without validation lacks scientific validity, and validation's necessity in evaluating model performance has been underlined [75]. This study used the area under the receiver operating characteristic curve (AUC-ROC), overall accuracy, and precision to validate the results and compare the performance of three different methods. The performance evaluation data detailed in Table 7 are derived from the components of the confusion matrix. In Table 7, true positive (TP) and true negative (TN) indicates the number of pixels correctly classified as landslide and non-landslide, respectively, while false positive (FP) and false negative (FN) indicates the number of pixels incorrectly classified as landslide and non-landslide, respectively [76].

Table 7 - Performance assessment metrics

Metrics	Equation
ROC (AUC)	$\text{True Positive Rate (TPR)} = \frac{TP}{TP+FN}$ $\text{False Positive Rate (FPR)} = \frac{FP}{FP+TN}$
Overall Accuracy (OA %)	$OA = \frac{TP+TN}{TP+TN+FP+FN}$
Precision	$\text{Precision} = \frac{TP}{TP+FP}$

The ROC curve depicts the false positive rate (FPR) on the X-axis and the actual positive rate (TPR) on the Y-axis, illustrating the trade-off between these two rates [77]. The area under the ROC curve (AUC) is a metric for evaluating the model's predictive performance [78]. ROC curve method is based on the creation of curves on a graph through the tabulation of sensitivities and specificities for various values of a continuous test measure [79]. The values obtained from the tabulation are plotted on a coordinate plane with sensitivity (the actual positive rate) depicted on the y-axis and specificity (the false positive rate) on the x-axis to represent the ROC curve graphically. The AUC metric, the most commonly used performance evaluation metric in landslide susceptibility mapping studies, was employed in this study. Figure 7 presents the ROC curves and AUC values of the models. As illustrated in Figure 7, the DL method achieved the highest AUC value (0.858), followed by the FR (0.803) and LR (0.783) methods. Consistent with other evaluation criteria, LR lagged behind the different methods in terms of AUC (Figure 10).

Overall accuracy (OA) reflects the likelihood that a test will accurately classify an individual, calculated as the sum of true positives (TP) and true negatives (TN) divided by the total number of individuals tested. OA is the weighted average of sensitivity and specificity [80] Utilizing the performance matrix aids in determining the reliability of the classifier under evaluation. Model evaluation metrics were used during both the training and validation phases. When assessing overall accuracy (OA), it was found that the method with the lowest accuracy in both phases was logistic LR. DL demonstrated higher accuracy During the training and validation phases than the other methods.

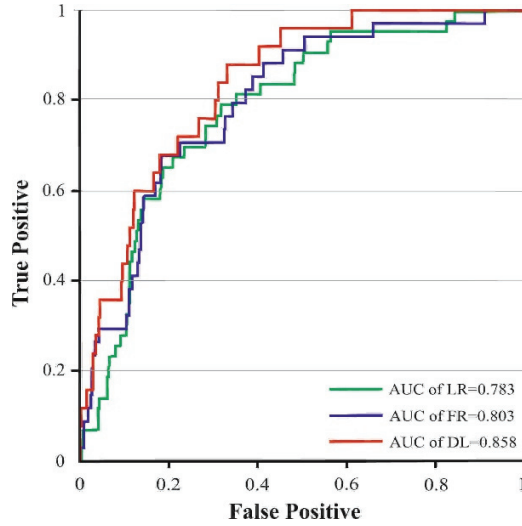


Figure 10 - ROC curves of the methods

Precision, also known as positive predictive value, is the proportion of actual positive instances among all instances identified as positive (Table 8), [81].

Table 8 - The performance of the methods applied in this study during the training and validation phase

Phase	Metrics	FR	LR	DL
Training	Accuracy (%)	81,060	80,025	84,368
	Precision	0,783	0,772	0,815
Validation	Accuracy (%)	80,329	78,811	82,340
	Precision	0,772	0,759	0,793

When the performance of the generated LSMs was evaluated, it was observed that the DL method exhibited superior sensitivity compared to the other methods. However, it is well acknowledged that the efficacy of these methods may vary depending on the specific characteristics of the study area and the conditioning factors employed.

5. CONCLUSIONS

This study applied the FR, LR, and DL methods, which are recognized as the most prevalent techniques for generating landslide susceptibility maps (LSMs), and assessed their performances. LSMs were categorized into five distinct landslide susceptibility levels. The overall accuracy, precision, and AUC-ROC metrics were employed to evaluate the validity of the generated LSMs. Across all three metric assessments, the DL method consistently

exhibited the highest performance, followed by FR and LR, respectively. Consequently, it was observed that LSMs produced by all three methods yielded satisfactory and effective results.

The outcome of the FR analysis illustrates that the category of very high susceptibility exhibits the most significant occurrence of landslides in all three maps, with subsequent classes in order of decreasing frequency being the high, moderate, low, and very low susceptibility categories. This demonstrates that the FR method effectively categorizes the study area into various landslide susceptibility classes by considering prior landslide occurrences. This implies that the method can consider previous landslide events when classifying the study area.

Furthermore, the DL method can specifically identify the features of the data through the model. For instance, in a classification problem, the features obtained manually through various methods are less likely to accurately depict the data model than the features identified by the DL method. Prior studies have indicated that the DL technique produces more accurate outcomes than other methodologies. Based on this knowledge, the outcomes of the present investigation, which were inferred from the calculated OA, precision and AUC values, imply that the LSM created by the DL approach demonstrates superior effectiveness compared to the maps generated by the FR and LR methods.

In conclusion, a comprehensive evaluation suggests that the generation of LSMs, their application in future engineering studies, and the identification of new settlements are crucial to mitigate or eliminate the detrimental effects of landslides. Additionally, developing new LSMs using various techniques and incorporating additional parameters in the map-generation process can aid in advancing scientific knowledge and the economic development of the region and country under study.

Contributions

This article is derived from the doctoral thesis titled “TOKAT İL MERKEZİNİN HEYELAN DUYARLILIK ANALİZİ” (<https://tez.yok.gov.tr/UlusalTezMerkezi/tezSorguSonucYeni.jsp-761579>).

References

- [1] Hungr, O., Leroueil, S., Picarelli, L., The Varnes classification of landslide types, an update. *Landslides*, 11, 167-194, 2014.
- [2] Jakob, M., Chapter 14 - Landslides in a changing climate, *Landslide Hazards, Risks, and Disasters (Second Edition)*. Hazards and Disasters Series, 505-579, 2022.
- [3] AFAD, *Landslide-Rockfall Basic Guide*. Ministry of Interior Disaster and Emergency Management Presidency, Ankara, Turkey, 2018.
- [4] Yalcin, A., Reis, S., Aydinoglu, A.C., Nadirli, S.A., A GIS-based comparative study of frequency ratio, analytical hierarchy process, bivariate statistics, and logistics regression methods for landslide susceptibility mapping in Trabzon, NE Turkey. *Catena*, 2011.

- [5] Guzzetti, F., Mondini, A.C., Cardinali, M., Fiorucci, F., Landslide inventory maps: New tools for an old problem. *Earth-Science Reviews*, 112, 42-66, 21, 2012.
- [6] Bhandari, B.P., Dhakal, S., Topographical and geological factors on gully-type debris flow in Malai River catchment, Siwaliks, Nepal. *Journal of Nepal Geological Society*, 59, 2019.
- [7] Gariano, S.L., Melillo, M., Peruccacci, S., How much does the rainfall temporal resolution affect rainfall thresholds for landslide triggering? *Natural Hazards*, 100, 655-670, 2020.
- [8] Kumi-Boateng, B., Peprah, M.S., Larbi, E.K., Prioritization of forest fire hazard risk simulation using hybrid grey relativity analysis (HGRA) and fuzzy analytical hierarchy process (FAHP) coupled with multicriteria decision analysis (MCDA) techniques - a comparative study analysis. *Geodesy and Cartography* 47, 3, 2021.
- [9] Wubalem, A., Landslide Inventory, Susceptibility, Hazard and Risk Mapping. Submitted: June 25th, 2021 Reviewed: September 17th, 2021 Published: November 20th, 2021.
- [10] Shano, L., Raghuvanshi, T.K., Meten, M., Landslide susceptibility evaluation and hazard zonation techniques - a review. *Geoenvironmental Disasters*, 7, 18, 2020.
- [11] Turan, I.D., Ozkan, B., Turkes, M., Deniz, O., Landslide susceptibility mapping for the Black Sea Region with spatial fuzzy multi-criteria decision analysis under semi-humid and humid terrestrial ecosystems. *Theoretical and Applied Climatology*, 140, 1233-1246, 2020.
- [12] Marker, B.R., Hazard and Risk Mapping, First Online: 01 January 2016, Citations Part of the Encyclopedia of Earth Sciences Series book series (EESS), 2016.
- [13] Reichenbach, P., Rossi, M., Malamud, B.D., Mihir, M., Guzzetti, F., A review of statistically-based landslide susceptibility models. *Earth-Science Reviews* 180, 60-91, 2018.
- [14] Pradhan, B., A comparative study on the predictive ability of the decision tree, support vector machine, and neuro-fuzzy models in landslide susceptibility mapping using GIS. *Computer and Geosciences*, 51, 350-365, 2013.
- [15] Chen, T., Niu, R., Du, B., Landslide spatial susceptibility mapping using GIS and remote sensing techniques: a case study in Zigui County, the Three Georges reservoir, China. *Environmental Earth Sciences*, 73, 5571-5583, 2015.
- [16] Saleem, N., Huq, E., Twumasi, N.Y.D., Javed, A., Sajjad, A., Parameters Derived from and/or Used with Digital Elevation Models (DEMs) for Landslide Susceptibility Mapping and Landslide Risk Assessment: A Review. *Geospatial Approaches to Landslide Mapping and Monitoring*, 8, 545, 2019.
- [17] Pourghasemi, H.R., Yansari, Z.T., Panagos, P., Pradhan, B., Analysis and evaluation of landslide susceptibility: a review of articles published during 2005-2016 (periods of 2005-2012 and 2013-2016). *Arabian Journal of Geosciences*, 11, 193, 2018.

- [18] Bui, D.T., Tuan, T.A., Klempe, H., Pradhan, B., Revhaug, I., Spatial prediction models for shallow landslide hazards: a comparative assessment of the efficacy of support vector machines, artificial neural networks, kernel logistic regression, and logistic model tree. *Landslides*, 13, 361-378, 2016.
- [19] Yong, C., Jinlong, D., Fei, G., Bin, T., Tao, Z., Hao, F., Li, W., Qinghua, Z., Review of landslide susceptibility assessment based on knowledge mapping. *Stochastic Environmental Research and Risk Assessment*, 36, 2399-2417, 2022.
- [20] NVİ, Tokat Provincial Directorate of Population and Citizenship, Tokat, Turkey, 2022.
- [21] Ayele, S., Raghuvanshi, T.K., Kala, P.M., Application of Remote Sensing and GIS for Landslide Disaster Management: A Case from Abay Gorge, Gohatsion–Dejen Section, Ethiopia. *Landscape Ecology and Water Management*, 15-32, 2014.
- [22] Althuwaynee, O.F., Pradhan, B., Park, H.J., Lee, J.H., A novel ensemble bivariate statistical evidential belief function with knowledge-based analytical hierarchy process and multivariate statistical logistic regression for landslide susceptibility mapping. *Catena*, 114, 21-36, 2014.
- [23] Chen, W., Xie, X., Peng, J., Shahabi, H., Hong, H., Bui, D.T., Duan, Z., Li, S., Zhu, A., GIS-based landslide susceptibility evaluation using a novel hybrid integration approach of bivariate statistical based random forest method. *Catena*, 164, 135-149, 2018.
- [24] Lee, S., Current and Future Status of GIS-based Landslide Susceptibility Mapping: A Literature Review. *Korean Journal of Remote Sensing*, 1, 179-193, 2019.
- [25] Meng, Q., Miao, F., Zhen, J., Wang, X., Wang, A., Peng, Y., Fan, Q., GIS-based landslide susceptibility mapping with logistic regression, analytical hierarchy process, and combined fuzzy and support vector machine methods: a case study from Wolong Giant Panda Natural Reserve, China. *Bulletin of Engineering Geology and the Environment*, 75, 923-944, 2016.
- [26] Kavzoglu, T., Teke, A., Predictive Performances of Ensemble Machine Learning Algorithms in Landslide Susceptibility Mapping Using Random Forest, Extreme Gradient Boosting (XGBoost) and Natural Gradient Boosting (NGBoost). *Arabian Journal for Science and Engineering*, 47, 7367-7385, 2022.
- [27] Zhang, H., Song, Y., Xu, S., He, Y., Li, Z., Yu, X., Liang, Y., Wu, W., Wang, Y., Combining a class-weighted algorithm and machine learning models in landslide susceptibility mapping: A case study of Wanzhou section of the Three Gorges Reservoir, China. *Computer and Geosciences*, 158, 2022.
- [28] Chung, C.F., Fabbri, A.G., Validation of spatial prediction models for landslide hazard mapping. *Natural Hazards*, 30, 451-472, 2003.
- [29] Ohlmacher, G.C., Davis, J.C., Using multiple logistic regression and GIS technology to predict landslide hazard in northeast Kansas, USA. *Engineering Geology*, 69, 3-4, 331-343, 2003.
- [30] Nachappa, T.G., Kienberger, S., Meeana, S.R., Hölbling, D., Blaschke, T., Comparison and validation of per-pixel and object-based approaches for landslide susceptibility mapping. *Geomatics, Natural Hazards and Risk*, 572-600, 2020.

- [31] Ercanoglu, M., Gokceoglu, C., Use of fuzzy relations to produce landslide susceptibility map of a landslide prone area (West Black Sea Region, Turkey). *Engineering Geology*, 75:229-250, 2004.
- [32] MTA, General Directorate of Mineral Research and Exploration, Ankara, Turkey, 2020.
- [33] Tsangaratos, P., Ilia, I., Comparison of logistic regression and Naïve Bayes classifier in landslide susceptibility assessments: The influence of models complexity and training dataset size. *Catena*, 145, 164-179, 2016.
- [34] Sun, D., Wen, H., Wang, D., Xu, J., A random forest model of landslide susceptibility mapping based on hyperparameter optimization using Bayes algorithm. *Geomorphology*, 362, 2020.
- [35] Conforti, M., Letto, F., Modeling Shallow Landslide Susceptibility and Assessment of the Relative Importance of Predisposing Factors, through a GIS-Based Statistical Analysis. *Geosciences*, 11, 8, 2021.
- [36] Siddique, T., Pradhan, S.P., Stability and sensitivity analysis of Himalayan road cut debris slopes: an investigation along NH-58, India. *Natural Hazards*, 93, 577-600, 2018.
- [37] El-Magd, S.A.A., Eldosouky, A.M., An improved approach for predicting the groundwater potentiality in the low desert lands; El-Marashda area, Northwest Qena City, Egypt. *Journal of African Earth Sciences*, 179, 2021.
- [38] Qin, Z., Lai, Y., Tian, Y., Study on failure mechanism of a plain irrigation reservoir soil bank slope under wind wave erosion. *Natural Hazards*, 109, 567-592, 2021.
- [39] Akgun, A., GIS-based erosion and landslide susceptibility assessment of the Ayvalık and surroundings. Ph.D. Thesis, Dokuz Eylül University, İzmir, Turkey, 2007.
- [40] Dai, F.C., Lee, C.F., Landslide characteristics and slope instability modeling using GIS. Lantau Island, Hong Kong. *Geomorphology*, 42, 213-228, 2002.
- [41] Liu, Q., Tang, A., Exploring aspects affecting the predicted capacity of landslide susceptibility based on machine learning technology. *Geocarto International*, 14547-14569, 2022.
- [42] Gokceoglu, C., Sonmez, H., Nefeslioglu, H.A., Duman, T.Y., Can, T., The 17 March 2005 Kuzulu landslide (Sivas, Turkey) and landslide-susceptibility map of its near vicinity. *Engineering Geology*, 81, 1, 65-83, 2005.
- [43] Duman, T.Y., Can, T., Gokceoglu, C., Application of logistic regression for landslide susceptibility zoning of Cekmece Area, Istanbul, Turkey. *Environmental Geology*, 51, 241-256, 2006.
- [44] Gokceoglu, C., Ercanoglu, M., Uncertainties on the parameters employed to prepare landslide susceptibility maps. *Bulletin of Earth Sciences Application and Research Centre of Hacettepe University Critical Review*, 2001.
- [45] Terranova, O.G., Garaino, S.L., Bruno, C., Greco, R., Pellegrino, A.D., Iovine, G.G.R., Landslide-risk scenario of the Costa Viola mountain ridge (Calabria, Southern Italy). *Journal of Maps*, 12, 261-270, 2016.

- [46] Clerici, A., Perego, S., Vescovi, P., A procedure for landslide susceptibility zonation by the conditional analysis method. *Geomorphology*, 48 (4): 349-364, 2002.
- [47] Ayalew, L., Yamagishi, H., The application of GIS-based logistic regression for landslide susceptibility mapping in the Kakuda-Yahiko Mountains (Central Japan). *Geomorphology*, 65, 15-31, 2005.
- [48] Ermini, L., Catani, F., Casagli, N., Artificial Neural Networks applied to landslide susceptibility assessment. *Geomorphology*, 66, 327-343, 2005.
- [49] Luzi, L., Pergalani, F., Slope Instability in Static and Dynamic Conditions for Urban Planning: the 'Oltre Po Pavese' Case History (Regione Lombardia- Italy), *Natural Hazards*, 20, 57-82, 1999.
- [50] Wachal, D.J., Hudak, P.F., Mapping landslide susceptibility in Travis County. Texas, USA, *GeoJournal*, 51, 245-253, 2000.
- [51] Siahkamari, S., Haghizadeh, A., Zeinivand, H., Tahmasebipour, N., Rahmati, O., Spatial prediction of flood-susceptible areas using frequency ratio and maximum entropy models. *Geocarto International*, 33, 927-941, 2017.
- [52] Huang, F., Yao, C., Liu, W., Li, Y., Liu, X., Landslide susceptibility assessment in the Nantian area of China: a comparison of frequency ratio model and support vector machine. *Geomatics, Natural Hazards and Risk*, 9, 919-938, 2018.
- [53] Khan, H., Shafique, M., Khan, M.A., Bacha, M.A., Shah, S.U., Calligaris, C., Landslide susceptibility assessment using Frequency Ratio, a case study of northern Pakistan. *The Egyptian Journal of Remote Sensing and Space Sciences*, 22, 11-24, 2018.
- [54] Gholami, M., Ghachkanlu, M.E., Khosravi, K., Pirasteh, S., Landslide prediction capability by comparison of frequency ratio, fuzzy gamma and landslide index method. *Journal of Earth System Sciences*, 128, 42, 2019.
- [55] Lee, S., Ryu, J., Won, J., Park, H., Determination and application of the weight for landslide susceptibility mapping using an artificial neural network. *Engineering Geology*, 71-80, 2004.
- [56] Ataol, M., Yesilyurt, S., Identification of landslide risk zones along the Çankırı-Ankara (Between Akyurt and Çankırı) state road. *Journal of Geography*, 0, 51-69, 2014.
- [57] Pham, B.T., Bui, D.T., Indra, P., Dholakia, M., Landslide Susceptibility Assessment at a Part of Uttarakhand Himalaya, India using GIS-based Statistical Approach of Frequency Ratio Method. *International Journal of Engineering Research and Technology*, 11, 338-344, 2015.
- [58] Demir, G., GIS-Based Landslide Susceptibility Mapping for a Part of the North Anatolian Fault Zone between Reşadiye and Koyulhisar (Turkey). *Catena*, 183, 104211, 2019.
- [59] Silalahi, F.E.S., Arifianti, P.Y., Hidayat, F., Landslide susceptibility assessment using frequency ratio model in Bogor. West Java, Indonesia. *Geoscience Letter*, 6, 10, 2019.

- [60] Erener, A., Lacasse, S., Landslide susceptibility mapping using GIS, 28th Asian Conference on Remote Sensing, 2007, Kuala Lumpur, Malaysia, 2007.
- [61] Demir, G., Landslide Susceptibility Mapping by Using Statistical Analysis in the North Anatolian Fault Zone (NAFZ) on the Northern Part of Suşehri Town, Turkey. *Natural Hazard*, 92, 133-154, 2018.
- [62] Karaman, M.O., Cabuk, S.N., Pekkan, E., Utilization of Frequency Ratio Method for the Development of Landslide Susceptibility Maps: Karaburun Peninsula Case, Turkey. *Research Square*, 2022.
- [63] Hilbe, J.M., *Logistic Regression Models*. 1st edition, New York, 2009.
- [64] Kleinbaum D.G., Kupper, L.L., Muller, K.E., *Applied regression analysis and other multivariable methods*. 3rd Edition, Duxbury Press, California, 798, 1998.
- [65] Atkinson, P.M., Massari, R., *Generalized Linear Modelling of Susceptibility to Attributes*. *Engineering Geology*, 32, 81-100, 1998.
- [66] Bui, D.T., Lofman, O., Revhaug, I., Landslide susceptibility analysis in the Hoa Binh province of Vietnam using statistical index and logistic regression. *Natural Hazards*, 59, 1413-144, 2011.
- [67] Das, I., Sahoo, S., van Westen, C., Stein, A., Haçık, R., Landslide susceptibility assessment using logistic regression and its comparison with a rock mass classification system, along a road section in the northern Himalayas (India). *Geomorphology*, 114, 1, 627-637, 2010.
- [68] Lang, S., Marquez, F.M., Beckham, C., Hall, M., Frank, E., WekaDeepLearning4j: A deep learning package for Weka based on DeepLearning4j. *Knowledge-Based Systems*, 178, 48-50, 2019.
- [69] Bengio, Y., *Deep learning of representations: looking forward*, Part of the Lecture Notes in Computer Science Book Series. Montreal University, Canada, 1-2, 2013.
- [70] LeCun, Y., Bengio, Y., Hinton, G., *Deep learning*. *Nature*, 521, 436-444, 2015.
- [71] Schmidhuber, J., *Deep learning in neural networks: An overview*. *Neural Networks*, 61, 85-117, 2015.
- [72] Goodfellow, I., Bengio, Y., Courville, A., *Deep learning*. MIT Press, 2016.
- [73] Jordan, M.I., Mitchell, T.M., *Machine learning: Trends, perspectives, and prospects*. *Science*, 349, 255-260, 2015.
- [74] Clark, W.A.V., Hosking, P.L., *Statistical Methods for Geographers*, John Wiley and Sons. 518, New York, 1991.
- [75] Akinci, H.A., Akinci, H., *Machine learning based forest fire susceptibility assessment of Manavgat district (Antalya)*. *Turkey Earth Science Informatics*, 16(1):397-414, 2023.

- [76] Ye, P., Yu, B., Chen, W., Liu, K., Ye, L., Rainfall-induced landslide susceptibility mapping using machine learning algorithms and comparison of their performance in Hilly area of Fujian Province. *China Nat. Hazards*, 113:965-995, 2022.
- [77] Pourghasemi, H.R., Pradhan, B., Gokceoglu, C., Moezzi, K.D., Landslide susceptibility mapping using a spatial multi criteria evaluation model at Haraz watershed, Iran. In *Terrigenous Mass Movements*; Pradhan, B., Buchroithner, M., Eds.; Springer: Berlin/Heidelberg, Germany, pp. 23-49. ISBN 978-3-642-25495-6, 2012.
- [78] Yilmaz, I., Landslide susceptibility mapping using frequency ratio, logistic regression, artificial neural networks and their comparison: A case study from Kat landslides (Tokat-Turkey). *Comput Geosci* 35(6):1125–1138, 2009.
- [79] Hoo, H.Z, Candlish, J., Teare, D., What is an ROC curve? *Emergency Medicine Journal*, 34, 6, 2017.
- [80] Aggarwal, C. C., *Neural Networks and Deep Learning*, Vol. 497, Springer, 2018.
- [81] Azarafza, M., Akgun, H., Atkinson, P.M., Derakhshani, R., Deep learning-based landslide susceptibility mapping. *Sci Rep* 11:24112, 2021.

Earthquake Performance Analysis of a Masonry School Building's Retrofitted State by the Equivalent Frame Method

Vefa OKUMUS^{1*}
Atakan MANGIR²



ABSTRACT

Nonlinear analyses of masonry structures are frequently used in both engineering practice and academic studies. Due to the dominant nonlinear behaviour of masonry structures, complex and extensive finite element models are required to obtain accurate analysis results. While masonry walls are usually modelled using fine-meshed shells or solid elements in such structures, high computing power in modelling, analyzing, and post-processing results is necessary for the analyses of large structures. In recent years, the equivalent frame method, as a solution to this problem has been developed and presented in the literature. In this study, the equivalent frame method is used in a masonry structure modelling, and the axial force-bending relationship is represented by force-based fiber elements. The multi-linear load-deformation relationship reflects the shear behaviour of the walls. Within the scope of the study, an existing masonry school building is modelled using the equivalent frame elements with OpenSees software. Seismic performance analyses are done considering the existing and retrofitted states of the structure, and the results are discussed in a comparative manner.

Keywords: Equivalent frame model, masonry structures, OpenSees, seismic performance analysis, retrofit.

1. INTRODUCTION

There are many techniques in the field of structural engineering that facilitate the analysis and understanding of existing masonry structures. Modelling the masonry elements with shell (plate), solid or frame members are among the finite element modelling methods used in the analysis of masonry structures. Engineers can gain crucial insights into the behaviour of

Note:

- This paper was received on November 17, 2023 and accepted for publication by the Editorial Board on July 19, 2024.
 - Discussions on this paper will be accepted by March 31, 2025.
- <https://doi.org/10.18400/tjce.1392529>

1 Istanbul Medipol University, Department of Civil Engineering, Istanbul, Türkiye
vefa.okumus@medipol.edu.tr - <https://orcid.org/0000-0002-4105-8423>

2 Istanbul Medipol University, Department of Civil Engineering, Istanbul, Türkiye
amangir@medipol.edu.tr - <https://orcid.org/0000-0003-4668-3938>

* Corresponding author

masonry buildings, aiding in the assessment of their structural integrity, retrofitting strategies, and overall safety by utilizing these methods. Equivalent Frame Modelling (EFM) and Solid Finite Element Modelling (SFEM) are two valuable methods that are frequently used in the current practice. These techniques enable engineers to simulate and evaluate the structural response of masonry buildings, providing precision in the assessment of their stability, strength, and overall performance.

EFM is a simplified approach that represents a masonry structure as an equivalent system of interconnected beams and columns which allows the approximation of the complex masonry system behaviour with a more manageable frame model, making it easier to analyze and understand the structural response. Bending moments, shear forces, and axial forces can be obtained from the interconnected beams and columns directly within the prescribed methodology. These internal forces and moments can further be used in identifying shear stresses, strains, and shear deformations. If fiber-based cross-sections are employed, stresses, strains and deformations can be obtained directly. EFM provides valuable insights into the load distribution, internal forces, and deformations of the structure and requires less computer power in terms of solution time by employing well-established principles of structural mechanics. It is particularly useful for preliminary assessments, predetermination of retrofitting strategies, and analyzing the global behaviour of masonry buildings under different loading conditions.

On the other hand, SFEM offers a more detailed and comprehensive approach to studying masonry structures. SFEM involves discretizing the structure into numerous solid finite elements, which are interconnected to simulate the behaviour of the entire system. Each element represents a small portion of the masonry, considering its material properties, geometry, and boundary conditions. SFEM allows for a more accurate analysis of stress distribution, strain concentrations, and failure mechanisms within the masonry elements by numerically solving the governing equations of structural mechanics. This method is particularly useful for investigating local phenomena, such as cracking, localized damage, and interaction between masonry units.

Both EFM and SFEM have their unique advantages and limitations when used in the analysis of existing masonry structures. EFM offers simplicity and efficiency in capturing the overall behaviour of the structure, making it suitable for preliminary assessments and initial design considerations with requiring considerably less computer power and solution time. Besides, SFEM provides a more detailed and realistic representation of the masonry behaviour, enabling the evaluation of the complex phenomena and assessment of the structural performance under various loading scenarios. However, it should be noted that SFEM requires more computational resources and expertise in numerical analysis.

There are many studies in the literature on the validation and application of these modelling techniques. Moreover, these methods are used on actual masonry buildings in some case studies with various analysis software. Some of these works are explained in this section for a better understanding of this study. Degli Abbati et al. [1] investigated the reliability of equivalent frame models (EFMs) by analyzing a 2-story masonry building, inspired by Pizzoli's town hall in Italy. EFMs were calibrated elastically using ambient vibration test results and then validated in the nonlinear range by simulating the dynamic response during the mainshocks of the 2016/2017 Central Italy earthquake. Camata et al. [2] presented a comparison between finite element models and EFMs for the analysis of seven two-story

masonry walls with asymmetric arrangements of openings using the Scientific Toolkit for OpenSees (STKO) and the OpenSees framework. They found good agreement in the numerical comparisons between the EFMs and finite element models for irregular walls. However, discrepancies are raised for walls with mixed compression-shear damage mechanisms, as the simplified frame model tends to prioritize one behaviour over the other. Cattari et al. [3] conducted the seismic analysis of masonry structures by comparing two modelling techniques: Continuum Constitutive Laws Models (CCLM) belonging to Finite Element (FE) models and Equivalent Frame (EF) models. They discussed the calibration of constitutive laws for single panels and validated the simplifications made in EF models using a 2D regular Unreinforced Masonry (URM) wall. In their work, the use of CCLM provided accurate results but came with computational challenges and required extensive input data. Besides, EF models offered computational efficiency and required fewer mechanical parameters. Cattari et al. [4] also investigated the reliability of four existing rules for the a priori identification of pier geometry in the equivalent frame (EF) idealization of unreinforced masonry walls, focusing on irregular walls with different height openings at the same storey or small openings. The findings of their study provided practical recommendations for EF wall idealization, indicating that some existing rules work well, while others require precautions or modifications in specific cases. They suggested neglecting small openings in the EF idealization process. D'Altri et al. [5] provided a comprehensive review of existing modelling strategies for masonry structures and introduced a novel classification of these strategies. They categorized those into four main categories as block-based, continuum, geometry-based and macroelement models. Each category is thoroughly reviewed, and the future challenges in the computational analysis of masonry structures are discussed in their work. Gunes et al. [6] focused on the seismic assessment of a reconstructed historic ruined mosque located in a castle. Their study comprises four stages: on-site examinations, laboratory tests, reconstruction process, and seismic performance analyses. The presented methodology and findings in their study provide valuable information for the literature on reconstructing the structural integrity of deteriorated historic structures. Gunes et al. [7] also presented a seismic performance evaluation methodology and retrofitting proposal for masonry-infilled reinforced concrete (RC) buildings using nonlinear analyses. The methodology is illustrated using a case study of a university building constructed in the 1940s., which is significant for seismic analysis of masonry-infilled RC dual system buildings, both before and after retrofitting. Lagomarsino et al. [8] emphasized that the equivalent frame approach is an attractive modelling strategy as it enables the analysis of complete 3D buildings with reasonable computational effort, aligning with practical engineering needs and recommendations in national and international codes. They discussed the implementation of the equivalent frame model in the TREMURI program, which is used for nonlinear seismic analysis of masonry buildings. Liberatore and Addessi [9] discussed the equivalent frame model used for assessing in-plane mechanisms of masonry walls by employing a 2-node force-based finite element with a linear elastic element, two flexural hinges, and a shear link with elastic-perfectly plastic behaviour. For reflecting the lumped plasticity, a return algorithm based on the Haar-Kármán principle and the gradient projection method is used, which ensure good convergence properties and optimal characteristics of the solution. Marano et al. [10] conducted quasi-static nonlinear analyses on two masonry buildings by discretization of walls to an equivalent frame using a macroelement (force-based beam-column element with fiber-based cross-section discretization and a shear hinge at the mid-span) that combines the bending and in-plane shear responses. The

analyzed buildings in their study represent examples of unreinforced and reinforced masonry from the Italian heritage, including a strategically monitored building damaged during the seismic events in Central Italy in 2016. Marino et al. [11] analyzed two unreinforced masonry buildings that were damaged during the Canterbury earthquake sequence in 2010/2011 using static and dynamic nonlinear analyses based on the equivalent frame approach. This approach's seismic response predictions are compared to observed building damage and time-history records from the earthquake sequence. They concluded that the equivalent frame method accurately predicts the seismic response of the clay brick URM buildings, providing valuable evidence for its use in the professional structural engineering community. Nicola et al. [12] provided a comprehensive review of nonlinear modelling techniques for analyzing the structural behaviour of masonry infills and their interaction with frame structures under in-plane loads. They discussed micro, meso, and macro approaches in detail where the macro approach combines frame elements with equivalent struts for the infill panel and is popular due to its simplicity and computational efficiency. Petracca et al. [13] proposed a continuous micro-model for analyzing masonry walls based on damage mechanics and compared this model with two existing discrete micro-models that use nonlinear interfaces for mortar joints and continuum elements for units. They analyzed critical aspects such as predicting failure load, collapse mechanism, computational efficiency, and the 2D plane-stress assumption in their work, which contributes to the understanding and comparison of different micro-modelling approaches for masonry analysis. Raka et al. [14] presented a model for seismic analysis of masonry structures based on the equivalent frame idealization, which builds upon previous research on force-based frame elements and considers axial, bending, and shear deformations using the Timoshenko beam theory. In their work, the shear panel response is set by incorporating a phenomenological cyclic section law, which is coupled with a fiber-section model that considers axial and bending responses. They concluded that the proposed panel model is computationally efficient, numerically stable, and suitable for analyzing multi-floor buildings with regular openings and box-like behaviour under seismic loads. Requena-Garcia-Cruz et al. [15] compared different equivalent frame (EF) modelling approaches for unreinforced masonry (URM) buildings with OpenSees software. They analyzed the Benchmark cases from the literature to test the reliability of the alternative approaches and compared results with a commonly used software in engineering practice. They emphasized that OpenSees can accurately analyze masonry structures with the EF approach, opening possibilities for further research on challenging phenomena like soil-foundation-structure interaction. Roca et al. [16] introduced an efficient method for assessing large historical masonry buildings which effectively models the complex geometries and nonlinear material behaviour by treating the load-bearing walls as equivalent frame systems composed of one-dimensional elements that incorporate biaxial constitutive equations to capture the nonlinear response of the material. The method they presented provides accurate predictions of the structural response and failure condition with computational efficiency which can be used to analyze real historical constructions and simulate repair and restoration operations. Shabani and Kioumars [17] developed a new macroelement, called the double modified MVLEM (DM-MVLEM) element, based on the multiple vertical line element method (MVLEM) in the OpenSees software platform for the computational analysis of unreinforced masonry (URM) buildings. The DM-MVLEM captures axial-flexural interaction with reduced computational effort compared to finite element models. They conducted experimental validation and comparisons with existing EFM methods (Unified Method and Composite Spring Method) to demonstrate the DM-MVLEM's ability in the

prediction of damage patterns and simulation of nonlinear behaviour in URM walls, including spandrels. Siano et al. [18] examined the application of the Equivalent-Frame Method (EFM) in modelling existing unreinforced masonry (URM) buildings. They conducted a comparative study with the more accurate Finite Element Method (FEM) in the linear domain by analyzing regular and irregular geometrical configurations to measure the modelling accuracy of EFM. Siano et al. [19] also investigated the accuracy of the Equivalent Frame Method (EFM) in modelling the seismic nonlinear behaviour of unreinforced masonry (URM) buildings. They examined two variations of the EFM approach, including a fiber discretized beam element and a traditional beam element with lumped plasticity and tested the models using static nonlinear analyses under equivalent loading and boundary conditions with the evaluation based on a comparative simulation of a two-storey URM wall experiment. Vanin et al. [20] proposed a new three-dimensional macroelement for modelling the dynamic in-plane and out-of-plane behaviour of masonry panels in unreinforced masonry buildings which is implemented in the OpenSees software and validated with experimental results from shear-compression and free vibration tests of masonry panels. This macroelement extends a previously developed approach to incorporate both in-plane and out-of-plane behaviour, including second-order geometrical effects and a coupled shear/flexural response.

This study involves modelling an existing masonry structure using the equivalent frame elements within the OpenSees software. A comprehensive analysis is conducted to compare the effectiveness of strengthening using existing and retrofitted models of the building. The primary focus is on the application of the EFM and the results obtained for the specific case study. The study aims to demonstrate the practical use of EFM in analyzing and retrofitting masonry structures rather than providing a validation of the EFM method.

2. DESCRIPTION OF THE STRUCTURE

The structure analyzed within the scope of this study is the Gazi Mustafa Kemal Primary School building located in Karatay, Konya. The history, plan dimensions, geometric properties, materials, and structural system of this building are presented in the following sub-sections.

2.1. Historical Background

Gazi Mustafa Kemal Primary School is located in the Şems-i Tebrizi Neighborhood, the historical city center of Karatay district, Konya province. One side of the building is adjacent to Alaeddin Boulevard Street, and the building is situated in proximity to Dar-ül Muallimat School in the northern direction. The Cultural and Natural Heritage Preservation Board registered the building on November 13, 1982. The map and facet views of the building are given in Figure 1.

The Gazi Mustafa Kemal Primary School project is one of the standard designs drawn by Mukbil Kemal Taş, the architect of Gazi and Latife Schools in Ankara. Konya Governor İzzet Bey deemed the location of the Kazanlı Medrese, situated in the vicinity of Alaeddin Hill, suitable for constructing the school. The construction was initiated by the German company Lenc (Leno) in 1926, and the structure was opened for education in 1927 (Figure 2).

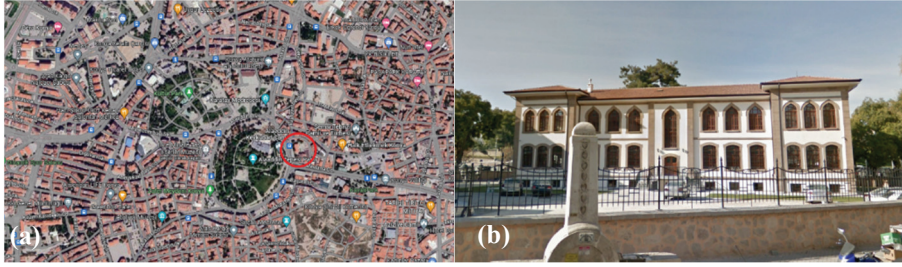


Figure 1 - (a) Map, (b) Facet views of Gazi Mustafa Kemal Primary School Building [21]



Figure 2 - Archive photos of Gazi Mustafa Kemal Primary School [22]

The building has undergone several functional and name changes over the years. After Gazi Mustafa Kemal Primary School moved to a larger building, it was used as Gazi Mustafa Kemal Anatolian Hospitality and Tourism Vocational High School from 1998 to 2006. In 2006, the Hospitality and Tourism Vocational High School relocated to a new building, and the structure was used as the Karatay District National Education Directorate and Public Education Center until 2015 [22]. The structure was restored by Konya Metropolitan Municipality within the scope of the Mevlana Culture Valley Urban Regeneration and Transformation Project in 2018. The building is now in the service of the Konya Technical University Continuing Education Application and Research Centre Directorate.

2.2. Geometric and Material Properties

The structure follows a common type of story plans for educational buildings during the First National Architecture Period of Türkiye, as it is one of the standard designs prepared by Mukbil Kemal Taş for the Ministry of Education. It has a symmetrical rectangular plan (14.5 m x 36.3 m) and an I-shaped corridor scheme, positioned along the north-south axis. The corridor scheme connected to the external facade, has windows that provide natural lighting. The stairs providing vertical circulation are located on the symmetry axis, directly opposite the main entrance. The central part of the building consists of the entrance and core, with corridors and spaces arranged around them. The building has two floors above the basement

floor as the ground and first floors. Floor heights are 2.9, 3.9 and 4.5 m from basement to first floors, respectively.

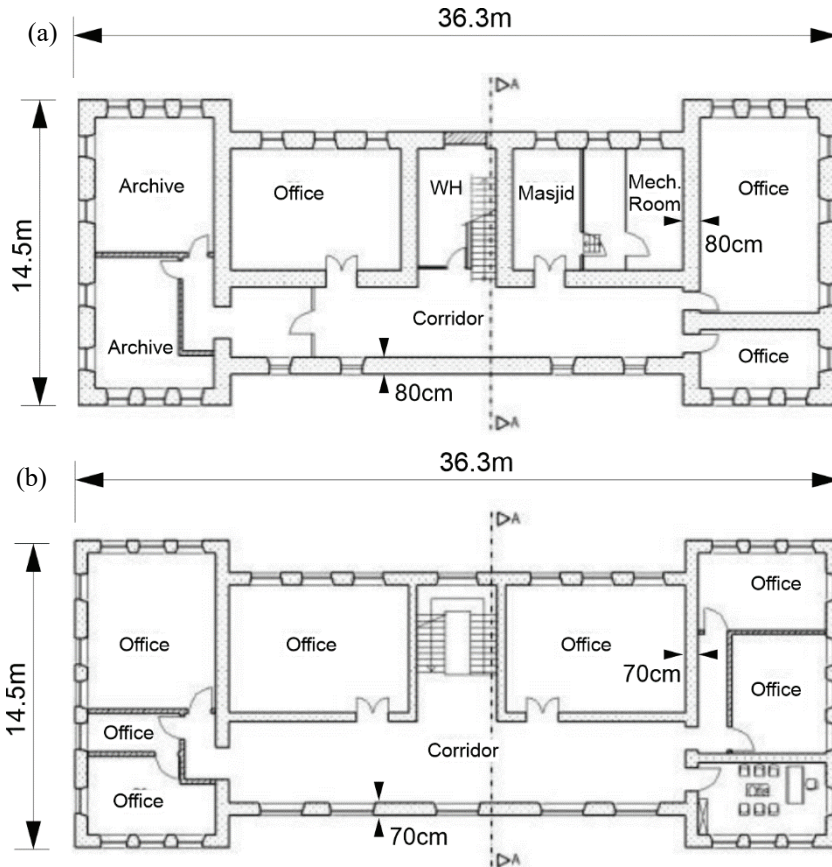


Figure 3 - (a) Basement and (b) first-floor plan drawings of the building [22]



Figure 4 - Elevation drawing of the building [22]

Gazi Mustafa Kemal Primary School is constructed using the masonry construction technique, with reinforced concrete slabs. Cut stones are used in the walls with varying thicknesses from 60 cm to 80 cm with approximately 70 cm wall thickness average. The stones of the arches used around the windows and doors on the facades are extended from the wall surface, preserving their original form and providing a dynamic appearance to the facade. Example floor plans and elevation drawings of the structure are presented in Figure 3 and Figure 4.

3. METHODOLOGY

The details of the equivalent frame method and the prepared finite element model are presented in the following sections.

3.1. Equivalent Frame Method and Software

The method specified by Lagomarsino et al. [8] is adopted for the formation of the equivalent frame model. In the relevant model, the structural elements of the masonry structure are idealized as wall (vertical) and spandrel beam (horizontal) elements, while the intermediate regions between them are modelled as rigid zones with linear-elastic rigid elements. Figure 5 presents the schematic representation of the relevant modelling technique. In our modelling approach, the assumptions and methodologies presented in the relevant literature, particularly Lagomarsino et al. [8], are thoroughly examined, providing a fundamental framework for our methodology. The objective of mitigating potential limitations related to our model assumptions is pursued by incorporating established principles and methodologies. However, the necessity of additional validation to bolster the credibility of our numerical model is acknowledged. Further validation methods will be explored in future research, including comparing our model predictions with experimental data and benchmarking against alternative modelling approaches to achieve this.

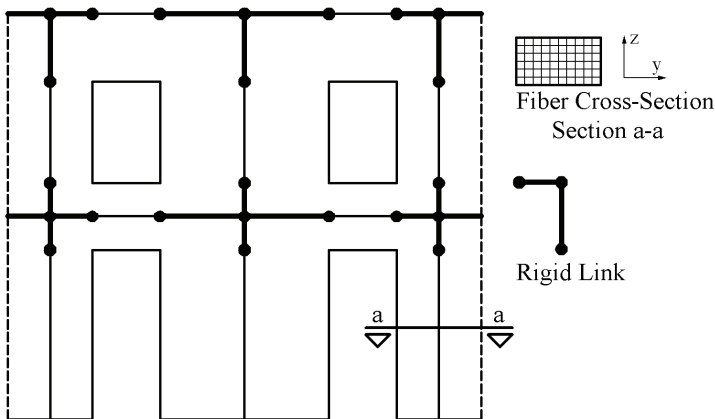


Figure 5 - Schematic representation of the equivalent frame modelling

An open-source structural analysis platform, OpenSees [23], is used in this study. The finite element model of the structure is prepared using Midas Gen [24] software and the prepared model is converted to the OpenSees' data type through object-oriented software developed by the authors. The analysis results are post-processed using the Scientific ToolKit for OpenSees, STKO [25].

In masonry structural elements, the axial force-bending behaviour is coupled and implemented through force-based elements and fiber sections. The *DamageTCID* material model [13] is used, which considers strength degradation in compression and tension states based on fracture energy in fiber sections. The concept of "damage index" is defined within the range of 0 to 1, considering failure criteria for the relevant material. A value of 0 represents a material state with no strength loss, while a value of 1 represents a completely damaged material that has lost its strength.

In vertical elements, shear deformations are considered using a multi-linear shear deformation-shear force relationship. The total shear capacity, V_t , of the vertical elements is obtained as follows [26]:

$$V_t = B \cdot t \frac{f_{tu}}{1.5} \sqrt{1 + \frac{\sigma}{f_{tu}}} \quad (1)$$

In this equation, B represents the wall length, t is the wall thickness, f_{tu} is the tensile strength, and σ is the vertical stress. The axial force acting on the members may vary throughout the analysis. Within the current capabilities, it is not possible to account for the effect of this variability on shear behaviour. Thus, the axial force on members has been considered constant, which is used in calculating the shear capacity of members. The vertical stresses due to the resulting axial forces are obtained from the vertical load analysis. The shear behaviour is determined based on this stress and remains unchanged throughout the analysis, which is defined using the *ModIMKPinching* [27] material model.

The material properties of the Textile Reinforced Mortar (TRM) elements used for retrofitting are represented by elastoplastic materials. The retrofitting elements are modelled by including additional fiber elements on the inner and outer faces of the piers and spandrels. While the focus of our study was primarily on axial and shear behaviours at the cross-section level, a kinematic analysis incorporating well-known failure modes for masonry walls is not conducted. This aspect will be addressed in our future endeavors.

3.2. Finite Element Model

The 3D analysis model prepared in accordance with the previously described method is shown in Figure 6. The material and soil property values recommended in TBEC-2018 [28] are relied upon due to the lack of available material and soil test data for this specific structure.

Since there is no available data of any specific study determining the mechanical material properties of the structure, the material properties are determined using the data provided for cut stones in TBEC-2018 [28]. Some of the material properties are given in Table 1.

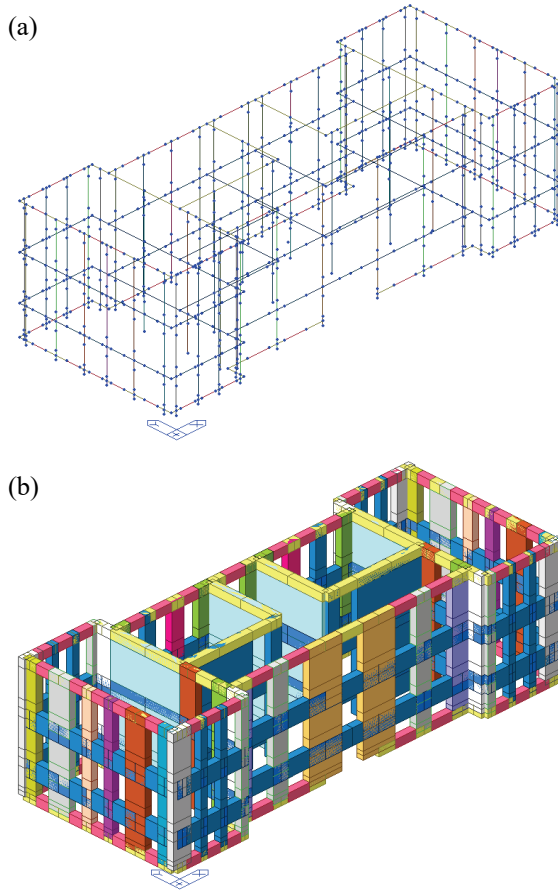


Figure 6 - (a) Frame, (b) extruded views of the 3D analysis model

Table 1 - Masonry material properties

Material Property	Symbol	Value
Block unit compressive strength	f_b	10.00 MPa
Mortar compressive strength	f_m	2.50 MPa
Characteristic compressive strength	f_k	3.00 MPa
Initial shear strength	f_{vko}	0.10 MPa
Tensile strength	f_t	0.15 MPa

The stress-strain relationships for the obtained *DamageTCID* material model are shown in Figure 7.

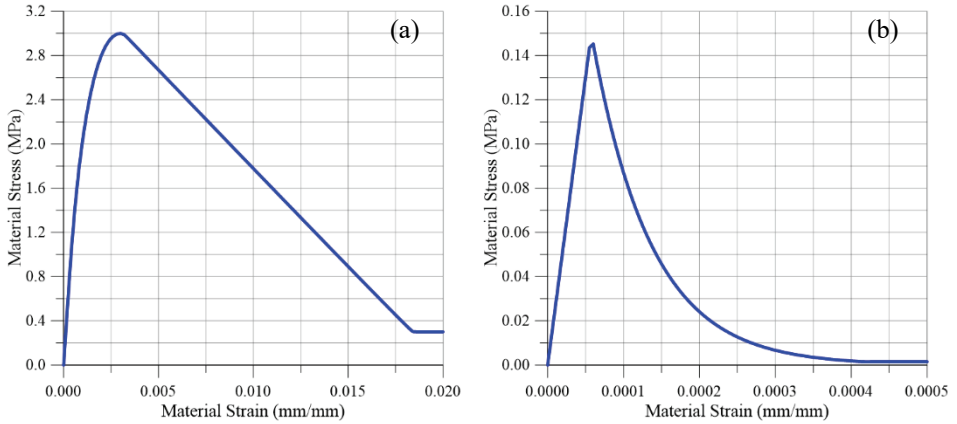


Figure 7 - (a) Compressive, (b) tensile behaviour of DamageTCID material model

The force-deformation curves for shear behaviour vary for each element due to the geometry, material properties, and axial load affecting the element. In Figure 8, an example force-deformation curve is presented for a wall with 6.3 m length, 0.7 m thickness and 210 kN axial compression. The axial behaviour is defined using fiber sections, while shear behaviour is established based on the shear force-shear deformation relationships generated at the cross-section level. These two behaviours are combined for a single section using the "Section Aggregator" feature. However, it's important to note that the shear behaviour within OpenSees does not consider the influence of changes in axial load on shear strength. Therefore, the relationships pertaining to shear deformation are calculated based on the axial forces obtained from the initial gravity analysis (including self-weight, dead and live loads) and remain constant throughout the analysis.

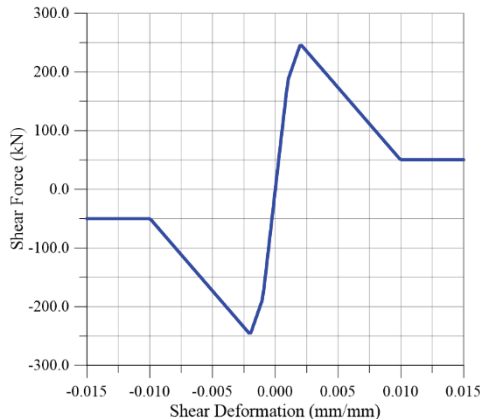


Figure 8 - An example force-deformation relationship for shear behaviour

Carbon fiber polymer grids with a cross-sectional area of $56 \text{ mm}^2/\text{m}$ are employed for the purpose of Textile Reinforced Mortar (TRM) retrofitting. The grids exhibit a tensile strength of 4900 MPa, an ultimate strain of 2%, and an elastic modulus of 245000 MPa. The mortar used for TRM retrofitting possesses a compressive strength of 15 MPa and a tensile strength of 2 MPa. A double-layered TRM application is implemented by applying TRM layers on both sides of all walls, with a layer thickness of 10 mm. The application of double-layered TRM on opposing sides of walls results in a total TRM thickness of 20 mm on each wall surface, thereby increasing the overall wall thickness by approximately 40 mm. In the finite element modelling of TRMs, additional two-layer fiber elements of 10 mm thickness have been added to both sides of each layer of the fiber sections. While the tensile strengths of these elements have been selected to be equivalent to the strength of the TRM grid element utilized, the compressive strengths are equalized to the compressive strength of the mortar used. Fiber elements of wall cross-sections in the finite element modelling of TRMs are presented in Figure 9.

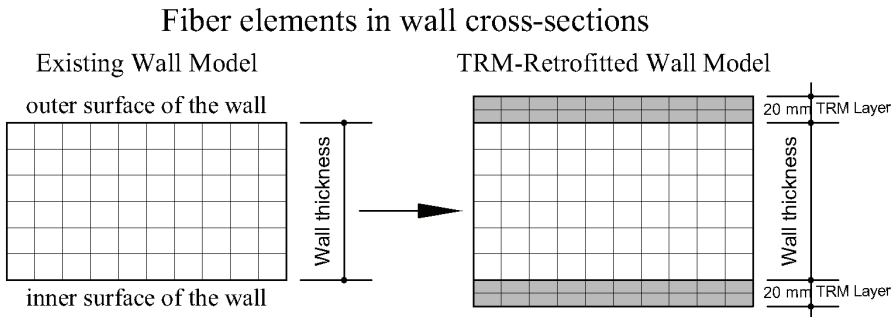


Figure 9 - Fiber elements of wall cross-sections in the finite element modelling of TRMs (not to scale)

Since the structure is a school building, the "Collapse Prevention" performance level according to GMERHB-2016 [29] is selected as the target performance level, specifically for the DD-1 seismic design level (earthquake with a 2% probability of being exceeded in 50 years). The soil class is assumed to be "ZC" because there is not any available specific study on the soil properties of the site. Table 2 summarizes the seismic parameters of the structure.

Table 2 - Seismic parameters of the structure

Parameter	Symbol	Value
Short period spectral acceleration coefficient	S_s	0.686
1.0 sec period spectral acceleration coefficient	S_1	0.148
Short period site coefficient	F_s	1.230
1.0 sec period site coefficient	F_1	1.500

Performance points are determined according to the criteria outlined in TBEC-2018 [28]. The relative lateral drift of the walls should not exceed 1% and the strains of the materials can exceed the strain limits by a maximum of 1.2 times for structures to satisfy the "Collapse Prevention" performance level as defined in GMERHB-2016 [29]. Since the structure has reinforced concrete slabs, a rigid diaphragm assumption is made for the floor slabs. Pinned boundary conditions are assumed at the base supports of unreinforced masonry walls due to the potential for significant stress imbalances resulting from uncertainty regarding whether the walls are fully embedded in the base. The mortar's low tensile strength compared to the masonry's compressive strength means that only very small strains are needed to induce "failure" in the mortar, particularly in the absence of reinforcement to help balance. This approach is accepted in the study of Aviram et al. [30]. Nonlinear static pushover analysis is performed in two stages: in the first stage, the structure is analyzed under gravity loads, and in the second stage, a horizontal pushover analysis is conducted in two orthogonal (x+ and y+) earthquake directions.

4. RESULTS AND DISCUSSION

The analysis results of the existing and retrofitted states of the structure are presented and discussed in detail in the following sections. Specific elements throughout the structure are selected, and their deformation and drift values are compared with the limit values specified in the regulation for historical structures GMERHB-2016 [29]. Furthermore, due to the utilization of the damage model in the study, damage indices for the selected elements are compared between the non-retrofitted and retrofitted states to observe changes in the damage incurred by the elements on a cross-sectional basis.

4.1. Existing State Results

Following the vertical (gravity) loading analysis, pushover analyses are performed for the application of horizontal seismic effects in both orthogonal directions. The displacement contours obtained from the horizontal pushover analyses are presented in Figure 10.

The damage indexes for fiber elements are provided for two different walls in Figure 11. Widespread tensile damage is observed in both vertical and horizontal elements throughout the structure with tensile damage indexes reaching a value of 1.0. Additionally, it is noted that damage indexes related to compressive stresses remain below the value of 0.24, indicating slight damage due to compressive stresses.

The seismic capacity diagrams for both directions are shown in Figure 12. Top displacement - base shear diagrams obtained from the pushover analyses for the existing state of the structure are presented in the next section (Figure 13).

The structural assessment is made at the performance point of the structure. It is observed that the behaviour of the masonry walls on the first floor is dominated by shear deformations. When the structural behaviour in the upper floors is examined, it is seen that the damages due to tensile stresses in the walls arise along with decreasing axial forces, and bending behaviour becomes more prominent, especially in walls with a low length-to-height ratio.

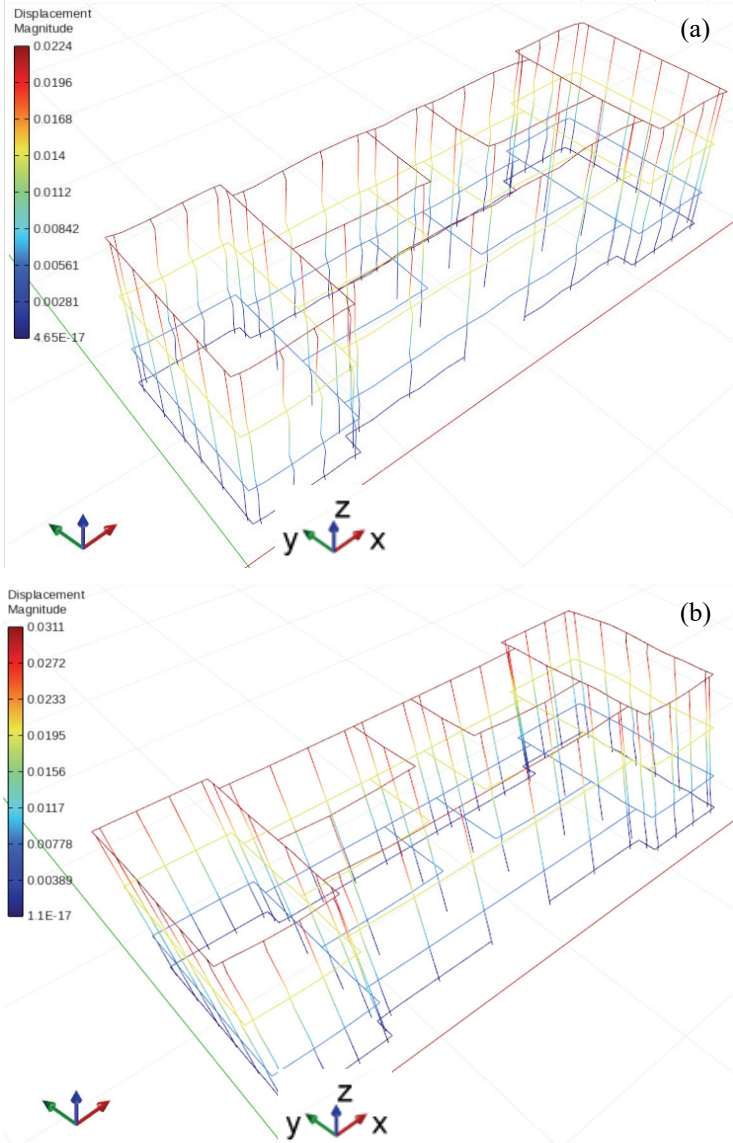


Figure 10 - Deformation magnitude contours of (a) x+ direction (b) y+ direction (units in m)

In Figure 15, the shear force-shear deformation relationship is given for an example wall. Although the wall has not reached its ultimate shear force capacity, the elastic limit is reached at the structural performance level. Although the relative drifts of walls meet the requirement

of 1% relative drift criteria, many elements, especially spandrels, fail to satisfy the strain limit conditions at the performance point for the existing state of the structure.

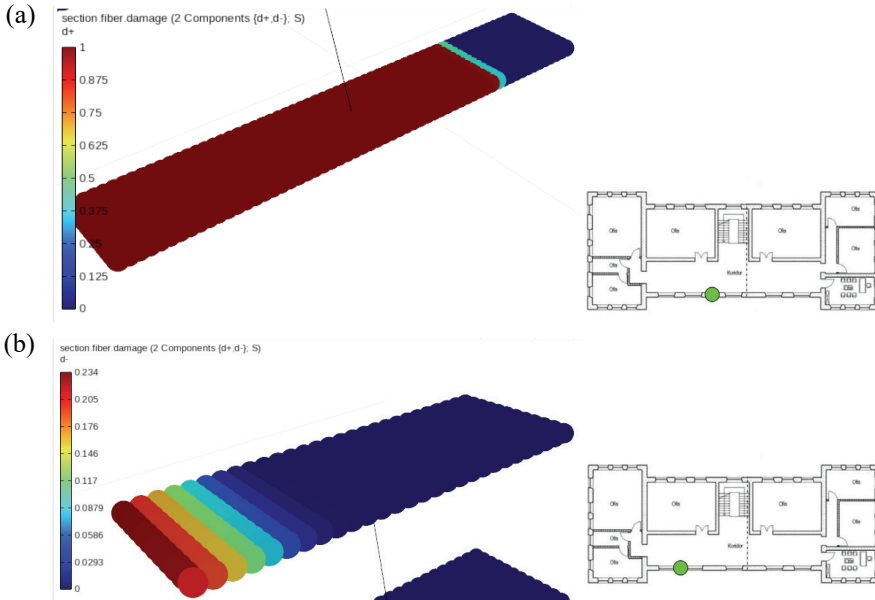


Figure 11 - Example damage indexes of two example walls for (a) tension, and (b) compression in the existing state

4.2. Retrofitted State Results

The seismic capacity diagrams for existing and retrofitted states for both directions are shown in Figure 12. The top displacement - base shear curves obtained from the pushover analyses for the retrofitted state of the structure are presented and compared with the curves of the existing state in Figure 13. In the $x+$ direction, the performance point of the structure is decreased from 22 mm to 13 mm. The base shear value corresponding to the performance point of the existing state is 4900 kN, which is increased to 6900 kN in the retrofitted state. In the $y+$ direction, the performance point of the structure is decreased from 24 mm in the existing state to 22 mm in the retrofitted state. The base shear value corresponding to the performance point in the existing state is 6050 kN, which is increased to 7250 kN in the retrofitted state. As seen from the top displacement - base shear diagrams, there has been a significant increase in the lateral load capacity of the structure. While the building's initial stiffness seems higher in the x direction compared to the y direction, the holes on the walls are more predominant on the structural behaviour in the x direction. Four main walls in y direction have no significant openings. Thus, retrofitting directly affects the initial stiffness and results in an increase in the x direction. This discrepancy in the distribution of openings leads to a lesser increase in stiffness in the y direction following the retrofitting process, resulting in the observed behaviour of the curves. The rapid onset of nonlinear behaviour is attributed to the relatively low strength of the masonry walls. It is believed that nonlinearity begins early in the analysis due to this factor.

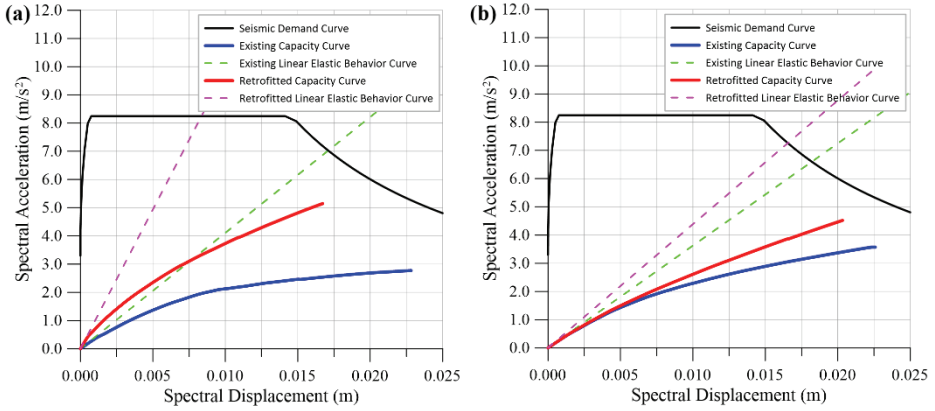


Figure 12 - Modal capacity diagrams for (a) $x+$, and (b) $y+$ directions for the existing and retrofitted states of the structure

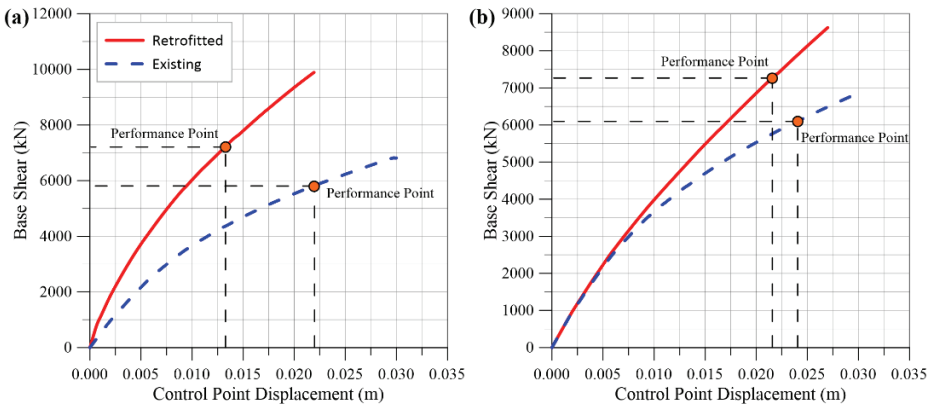


Figure 13 - Comparison of top displacement – base shear diagrams for (a) $x+$, and (b) $y+$ directions

In Figure 14, the fiber damage indexes in the retrofitted state for the two example walls previously provided in Figure 11 are presented. Due to the high tensile strength of the TRM elements, the tensile capacities of the walls subjected to bending are significantly increased in many cases, and in some walls, tensile damages are completely prevented. The compressive damage indexes are also reduced to much lower levels, such as 0.10, from the initial values of 0.24.

The shear force - shear deformation relationships for an example wall (with 6.3 m length and 0.7 m thickness) in the existing and retrofitted states are shown in Figure 15. The wall shear deformations exceeded the elastic limit significantly in the existing state, reaching a value of 0.002. In the retrofitted state, the shear deformations slightly exceeded the elastic limit, reducing to a value of 0.0011.

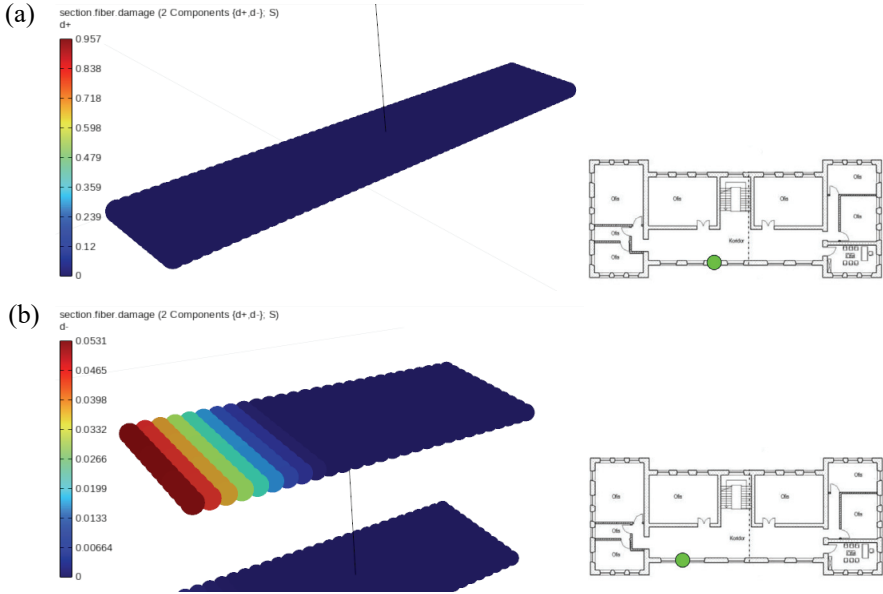


Figure 14 – Example damage indexes of two example walls for (a) tension, and (b) compression in the retrofitted state

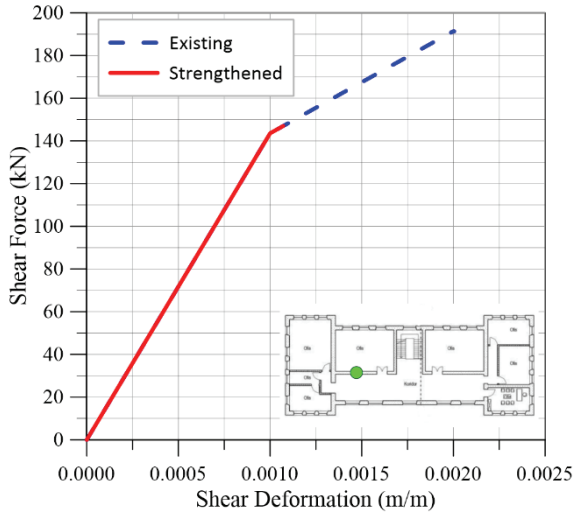


Figure 15 - Shear force – shear deformation diagrams comparison for an example wall

The retrofitted state of the structure satisfies both the drift and strain limit criteria for the target performance level. This indicates that the retrofitting measures are successful in improving the structural behaviour and meeting the required performance objectives.

5. CONCLUSION

The reliability of the equivalent frame method for masonry structures has been discussed in various studies, which requires less computing power in structural analysis with respect to solutions with solid and plane elements. In this study, the seismic performance analysis of an existing masonry structure and its retrofitted state is performed using the equivalent frame method. The primary focus of this study is on the application of the Equivalent Frame Method (EFM) and the results obtained from the specific case study, rather than on the validation of the EFM itself. The objective is to demonstrate the practical utility of EFM in the analysis and retrofitting of masonry structures.

Modelling, discretization, and the significant nonlinear behaviour of masonry structures make the determination of seismic performance quite challenging. In this context, the use of the equivalent frame model for masonry structures that can be modelled only through vertical and horizontal frame elements is presented as an alternative to plane and solid element models. A retrofitting study is conducted using this method, and the results are evaluated.

Textile-reinforced mortar retrofitting elements are applied on both the vertical (walls) and horizontal (spandrel beams) elements from their inner and outer faces. The seismic performance of the structure is significantly improved in the retrofitted model. It is observed that the tensile force capacities of elements with tensile damage are significantly increased. Similarly, the compressive damage indexes of masonry elements are significantly reduced. Moreover, the shear deformations in the existing state are reduced by almost half. It is concluded that the structure, which could not achieve the target performance level in the existing state, can achieve it in the case of retrofitting with the proposed method. Modelling masonry walls in such structures typically requires fine-meshed shells or solid elements, necessitating significant computing power for modelling, analysis, and post-processing of results and higher solution time, particularly in the analysis of large structures. Since the modelling was done only by frame elements in EFM, the analyses performed in this study indicate that the equivalent frame method has the potential to provide a streamlined modelling and analysis process and a faster solution for both existing and retrofitted states of these structures.

The application of the equivalent frame model in seismic analysis of masonry structures is addressed in our study by presenting a detailed analysis of a modelling and analysis approach for both existing and retrofitted states, thereby extending the understanding of the capabilities and limitations of this method. The challenges associated with modelling masonry structures, particularly regarding computational efficiency and accuracy, are addressed using the equivalent frame model. The use of this model in capturing the seismic behaviour of masonry structures is demonstrated, showcasing the method's potential as a viable alternative to traditional solid and plane element models. Additionally, the benefits of using the equivalent frame model for retrofitting studies, which include the modelling of fiber TRM layers are highlighted in our study, as it enables a streamlined approach to assess the seismic performance of retrofitted structures. Overall, the presented methodology in this study shows the alternative modelling and analysis steps that may be followed, paving the way for further advancements in applying the equivalent frame model in seismic analysis and retrofitting of masonry structures.

A parametric study considering various earthquake and retrofitting levels for the forthcoming research as a natural extension of the current work, as well as the comparison using a different finite element modelling method, is highly valued by the authors. Furthermore, comprehensive time-history analyses with the most up-to-date seismic records from recent Maraş earthquakes is recommended by the authors as future work.

References

- [1] Degli Abbati, S., Morandi, P., Cattari, S., & Spacone, E. (2022). On the reliability of the equivalent frame models: the case study of the permanently monitored Pizzoli's town hall. *Bulletin of Earthquake Engineering*, 20(4), 2187-2217.
- [2] Camata, G., Marano, C., Sepe, V., Spacone, E., Siano, R., Petracca, M., ... & Pelà, L. (2022). Validation of nonlinear equivalent-frame models for irregular masonry walls. *Engineering Structures*, 253, 113755.
- [3] Cattari, S., Camilletti, D., D'Altri, A. M., & Lagomarsino, S. (2021). On the use of continuum Finite Element and Equivalent Frame models for the seismic assessment of masonry walls. *Journal of Building Engineering*, 43, 102519.
- [4] Cattari, S., D'Altri, A. M., Camilletti, D., & Lagomarsino, S. (2022). Equivalent frame idealization of walls with irregular openings in masonry buildings. *Engineering Structures*, 256, 114055.
- [5] D'Altri, A. M., Sarhosis, V., Milani, G., Rots, J., Cattari, S., Lagomarsino, S., ... & de Miranda, S. (2020). Modeling strategies for the computational analysis of unreinforced masonry structures: review and classification. *Archives of computational methods in engineering*, 27, 1153-1185.
- [6] Gunes, B., Cosgun, T., Sayin, B., Ceylan, O., Mangir, A., & Gumusdag, G. (2021). Seismic assessment of a reconstructed historic masonry structure: A case study on the ruins of Bigali castle mosque built in the early 1800s. *Journal of Building Engineering*, 39, 102240.
- [7] Gunes, B., Mangir, A., Cosgun, T., Sayin, B., & Akcay, C. (2022). Seismic performance assessment of a historical masonry-infilled RC building located in the historical peninsula of Istanbul (1940s). In *Structures* (Vol. 45, pp. 951-968). Elsevier..
- [8] Lagomarsino, S., Penna, A., Galasco, A., & Cattari, S. (2013). TREMURI program: an equivalent frame model for the nonlinear seismic analysis of masonry buildings. *Engineering structures*, 56, 1787-1799.
- [9] Liberatore, D., & Addessi, D. (2015). Strength domains and return algorithm for the lumped plasticity equivalent frame model of masonry structures. *Engineering Structures*, 91, 167-181.
- [10] Marano, C., Petracca, M., Camata, G., & Spacone, E. (2021). Equivalent frame method combining flexural and shear responses of masonry buildings. In *12th International Conference on Structural Analysis of Historical Constructions (SAHC)*.

- [11] Marino, S., Cattari, S., Lagomarsino, S., Dizhur, D., & Ingham, J. M. (2019, June). Post-earthquake damage simulation of two colonial unreinforced clay brick masonry buildings using the equivalent frame approach. In *Structures* (Vol. 19, pp. 212-226). Elsevier.
- [12] Nicola, T., Leandro, C., Guido, C., & Enrico, S. (2015). Masonry infilled frame structures: state-of-the-art review of numerical modelling. *Earthquakes and structures*, 8(3), 733-759.
- [13] Petracca, M., Pelà, L., Rossi, R., Zaghi, S., Camata, G., & Spacone, E. (2017). Micro-scale continuous and discrete numerical models for nonlinear analysis of masonry shear walls. *Construction and Building Materials*, 149, 296-314.
- [14] Raka, E., Spacone, E., Sepe, V., & Camata, G. (2015). Advanced frame element for seismic analysis of masonry structures: model formulation and validation. *Earthquake Engineering & Structural Dynamics*, 44(14), 2489-2506.
- [15] Requena-Garcia-Cruz, M. V., Cattari, S., Bento, R., & Morales-Esteban, A. (2023). Comparative study of alternative equivalent frame approaches for the seismic assessment of masonry buildings in OpenSees. *Journal of Building Engineering*, 105877.
- [16] Roca, P., Molins, C., & Marí, A. R. (2005). Strength capacity of masonry wall structures by the equivalent frame method. *Journal of structural engineering*, 131(10), 1601-1610.
- [17] Shabani, A., & Kioumars, M. (2022). A novel macroelement for seismic analysis of unreinforced masonry buildings based on MVLEM in OpenSees. *Journal of Building Engineering*, 49, 104019.
- [18] Siano, R., Sepe, V., Camata, G., Spacone, E., Roca, P., & Pelà, L. (2017). Analysis of the performance in the linear field of equivalent-frame models for regular and irregular masonry walls. *Engineering Structures*, 145, 190-210.
- [19] Siano, R., Roca, P., Camata, G., Pelà, L., Sepe, V., Spacone, E., & Petracca, M. (2018). Numerical investigation of nonlinear equivalent-frame models for regular masonry walls. *Engineering Structures*, 173, 512-529.
- [20] Vanin, F., Penna, A., & Beyer, K. (2020). A three-dimensional macroelement for modelling the in-plane and out-of-plane response of masonry walls. *Earthquake Engineering & Structural Dynamics*, 49(14), 1365-1387.
- [21] Google Maps, 2023. <https://goo.gl/maps/mPTxKffFv2upNPCL8> Retrieved on: 06.07.2023.
- [22] Parlak, Ö., Yaldiz, E. (2017). Konya'da Erken Cumhuriyet Dönemi ilkokul yapıları. *Türk İslam Medeniyeti Akademik Araştırmalar Dergisi*, 12, 24, 175-202.
- [23] Mazzoni, S., McKenna, F., Scott, M. H., and Fenves, G. L. (2006). *OpenSees command language manual*. Pacific Earthquake Engineering Research (PEER) Center.
- [24] Midas Gen. (2020). *Integrated Solution System for Building and General Structures*. MIDAS Information Technology Co., Gyeonggi-do Korea.

- [25] A Petracca, M., Candeloro, F., & Camata, G. (2019). STKO user manual. ASDEA Software Technology, Pescara Italy.
- [26] Turnšek, V., & Čačovič, F. (1971). Some experimental results on the strength of brick masonry walls. Proceedings of the 2nd International Brick Masonry Conference, 149-156.
- [27] Ibarra, L.F., Medina, R. A., & Krawinkler, H. (2005). Hysteretic models that incorporate strength and stiffness deterioration, *Earthquake Engineering and Structural Dynamics*, 34(12), 1489-1511.
- [28] TBEC (2018). Türkiye Building Earthquake Code. Disaster and Emergency Management Presidency, Ministry of Interior, The Republic of Türkiye, Ankara, 2018.
- [29] GMERHB (2016). Guide to Management of Earthquake Risks in Historic Buildings. Directorate General of Foundations, Ministry of Culture and Tourism, The Republic of Türkiye, Ankara, 2018.
- [30] Aviram, A., Badillo, J. W., Prieto, J. A., & Jaramillo, J. D. (2019). Unreinforced brick masonry wall collapse investigation under moderate wind loads, *Revista Ingeniería de Construcción*, 34(1), 65-80.

Mixed Finite Elements for Higher-order Laminated Cylindrical and Spherical Shells

Yonca BAB^{1*}
Akif KUTLU²



ABSTRACT

This paper presents a mixed finite element (MFE) formulation for studying the linear static behavior of both thin and relatively thick laminated composite cylindrical and spherical shells. The method employs the Higher Order Shear Deformation Theory to account for cross-section warping due to transverse shear stress. It ensures the stationarity of the system's functional using the Hellinger-Reissner principle. Finite element discretization is accomplished with four-noded quadrilateral two-dimensional elements. The MFE formulation offers the advantage of directly obtaining displacements and stress resultants at the nodes. Comparison and convergence analyses are performed considering various shear functions, boundary conditions, and geometrical configurations.

Keywords: Higher order shear deformation theory, laminated composite shell, Hellinger-Reissner principle, mixed finite element method, static analysis.

1. INTRODUCTION

Laminated composite shells, as fundamental thin-walled structural elements, find frequent applications in various industries owing to their inherent advantages. These shells are typically composed of different material layers and play a pivotal role in sectors such as construction, aviation, automotive, and marine industries. The history of laminated composite shells dates back to the mid-20th century when researchers began combining diverse materials to attain superior performance characteristics. This includes achieving a high strength-to-weight ratio, robust resistance to corrosion, fatigue, and impact, enhanced design flexibility, improved energy efficiency etc. Load-bearing capacity, damage initiation, and failure load are crucial considerations in the design of composite materials. Thus, ensuring structural integrity necessitates a comprehensive mechanical analysis. Although

Note:

- This paper was received on November 17, 2023 and accepted for publication by the Editorial Board on July 19, 2024.
- Discussions on this paper will be accepted by March 31, 2025.
- <https://doi.org/10.18400/tjce.1396909>

1 Istanbul Technical University, Department of Civil Engineering, Istanbul, Türkiye
bab@itu.edu.tr - <https://orcid.org/0000-0002-1807-9306>

2 Istanbul Technical University, Department of Civil Engineering, Istanbul, Türkiye
kutluak@itu.edu.tr - <https://orcid.org/0000-0001-6865-3022>

* Corresponding author

experimental analyses may be considered as an option for mechanical investigations, due to practical constraints, whether financial or physical, the feasibility of conducting experimental analyses is often limited. Theoretical approaches stand out for the assessment of structural systems as they provide a comprehensive environment regarding various scenarios. Numerous studies in the literature explore the effectiveness of the theories developed for the mechanical analyses of laminated structures and try to improve their accuracy further. Several prominent theories in structural analysis include Classical Lamination Theory (CLT), First-Order Shear Deformation Theory (FSDT), Higher-Order Shear Deformation Theory (HSDT), and Zigzag Theories (ZZ) [1,2].

Reddy and Chandrashekhara [3] employed FSDT to create a finite element for analyzing geometrically non-linear transient responses of laminated composite spherical and cylindrical shells. Hossain et al. [4] examined numerical analysis of laminated spherical shells applying FSDT. Asadi and Qatu [5] examined static response of thick laminated composite cylindrical shells using two First Order Shear Deformation Theories (FSDTs), with results compared to existing literature and 3D analysis for validation. Khdeir [6] obtained exact solutions for the free vibration and static deflection of cross-ply laminated cylindrical panels and circular cylindrical shells using deep FSDT. Mousavi and Aghdam [7] applied the differential cubature method and FSDT to analyze the bending of laminated cylindrical panels with various boundary conditions and loads.

Sobhaniragh et al. [8] employed the thermal response of nanocomposite cylindrical shells reinforced by aggregated Carbon Nanotubes adopting Reddy's Third-Order Shear Deformation Theory (TSDT). Reddy and Liu [9] presented a pioneering study that carried out the static and dynamic analysis of laminated composite spherical and cylindrical shells using HSDT. Sayyad and Ghugal [10] and Mantari et al. [11] obtained analytical solutions for static analyses of laminated spherical shells based on HSDT. Kumar et al. [12] investigated static behavior of laminated composite spherical, cylindrical, conical and hyper shells based on FEM and HSDT. Giunta et al. [13] implemented Carrera's Unified Formulation (CUF) for laminated spherical shells. Asadi et al. [14], Ton-that et al. [15] and Zuo et al. [16] used different theories in the static and dynamic analysis of laminated composite shells. Yaghoobshahi et al. [17] applied HSDT to analyze laminated shells, resulting in a system of 31 differential equations solved numerically for various shell configurations, with results validated against ANSYS software. Groh and Weaver [18] addressed static inconsistencies in certain HSDTs applied to beams, plates, and cylindrical shells with clamped boundaries, highlighting inaccuracies in vanishing Kirchhoff rotation conditions and proposing improved formulations to correct these shortfalls. Bhaskar and Varadan [19] implemented HSDT for analyzing laminated anisotropic cylindrical shells of revolution, based on realistic in-plane displacement approximations, validated against 3D elasticity results, and applied to an isoparametric FEM. Doan et al. [20] explored stress concentration in cylinder laminated shells due to force and structural variations based on Quasi-3D HSDT. Viola et al. [21] presented static behavior of doubly-curved laminated composite shells and panels using a 2D HSDT and Generalized Differential Quadrature (GDQ) technique. Pinto Correia et al. [22] presented an isoparametric FE for static, dynamic and buckling analyses of laminated conical shell panels based on HSDT. It supports static analysis, eigenvalue problems, and demonstrates with illustrative examples. Tornabene et al. [23] investigated the recovery of through-the-thickness transverse strains and stresses in functionally graded doubly-curved sandwich shell structures applying HSDT and CUF.

Yasin and Kapuria [24] employed the ZZ to analyze the static and dynamic behavior of singly- and doubly-curved composite and sandwich shallow shells. Gupta and Pradyumna [25] worked also on ZZ for the bending analysis of variable stiffness laminated spherical, cylindrical and hyperboloid shells. Examples of various studies dealing with different aspects of shell analysis are given next.

Kulikov and Plotnikova [26] extended Sampling Surfaces (SaS) method to cylindrical and spherical laminated composite shells to solve 3D elasticity problems accurately by using strategically placed SaS. Qatu and Algothani [27] employed a consistent set of equations to derive exact solutions for isotropic and laminated composite plates and cylindrical shallow shells. They applied the Ritz method and finite elements to compare the static behavior. Karatas and Yukseler [28] presented the snap-through buckling behavior of rigid vinyl polyethylene shallow spherical shells subjected to static ring loads using finite difference and the Newton-Raphson Method. Sofiyev et al. [29] investigated the torsional stability of non-homogeneous orthotropic composite cylindrical shells within an elastic medium.

Some recent studies on the laminated shell analysis include Yadav et al. [30], where the authors analyzed the dynamic instability and nonlinear vibrations of fluid-filled laminated composite cylindrical shells under harmonic axial loading, considering skew modes and using HSDT. Ray [31] provided three-dimensional exact solutions for the static analysis of spherical, paraboloid and hyperboloid antisymmetric angle-ply composite shells. Alam et al. [32] introduced a modified higher-order zigzag theory for the static analysis of laminated cylindrical and spherical composite/sandwich shells. Arumugam et al. [33] formulated the vibration and damping characteristics of reinforced laminated composite cylindrical sandwich shells adopting HSDT and FE. Within the realm of FE formulations, mixed methodologies have been utilized in numerous investigations on structures in existing literature, and a few of these is provided below.

Ozutok and Madenci [34] combined the mixed finite element method (MFEM) with HSDT for static analysis of laminated composite beams. Kutlu et al. [35–37] and Aribas et al. [38–40] have illustrated the benefits of MFEM-derived formulations while precisely predicting stress resultants and components in diverse structural configurations. Kutlu and Omurtag [41] applied a MFE formulation based on the Hellinger-Reissner principle for the static behavior of elliptic plates under large deflection conditions. Omurtag and Akoz [42] introduced a computational procedure and a mixed finite element (ORTH036) for orthotropic cylindrical shells.

In this study, the mixed finite element formulation for laminated composite beams based on HSDT is extended, as originally derived by Bab and Kutlu [43,44], to perform static analyses on laminated spherical and cylindrical shells. For the higher order terms, shear functions suggested by Touratier [45], Reddy [46], Reissner [47] and Nguyen Xuan et al. [48] are conducted. The Hellinger-Reissner principle is employed to describe the energy expression of the spherical shell and reduced for the cylindrical shell. In the displacement field, three displacement and two rotation terms are taken into account. The generated mixed finite element functional contains quantities in terms of displacements and stress resultants. During the generation of finite element system equations, quadrilateral four-node elements are described with bi-linear shape functions. By solving the finite element equations, displacement and rotation components, as well as force and moment type quantities, are obtained directly at the nodes. In this way, strain measurements are calculated using

compliance matrices without using derivatives at the nodes. Convergence analyses are performed by increasing the element density in the meshes. Comparison analyses are carried out with static solutions in the literature. Several solutions are presented in various lamination, loading and boundary conditions to show the effectiveness of the proposed numerical procedure on the analyses of laminated composite shell structures.

2. FIELD EQUATIONS AND NUMERICAL FORMULATION

Considering the higher order shear effect, the displacement field of the laminated composite spherical shell (Figure 1a) can be described as follows:

$$\begin{aligned}
 u^*(x, y, z) &= \left(1 + \frac{z}{R_x}\right)u(x, y) - z w_{,x}(x, y) + f(z)\theta_x(x, y) \\
 v^*(x, y, z) &= \left(1 + \frac{z}{R_y}\right)v(x, y) - z w_{,y}(x, y) + f(z)\theta_y(x, y) \\
 w^*(x, y, z) &= w(x, y)
 \end{aligned} \tag{1}$$

Here, $u^*(x, y, z)$ and $v^*(x, y, z)$ denote axial displacement field and $w^*(x, y, z)$ denotes the transverse displacement field of the shell. $u(x, y)$ and $v(x, y)$ are the axial displacements and $w(x, y)$ is the deflection of the shell at its mid-surface where x and y are curvilinear orthogonal coordinates defined at the mid-surface of the shell. z is the coordinate in the direction of shell thickness (Figure 1b). Also, $\theta_x(x, y)$ describes the rotation of the section about the y -axis and $\theta_y(x, y)$ describes the rotation of the section about the x -axis. R_x and R_y are the radii of curvatures of the spherical shell. When the formulation is reduced to the cylindrical shell, $R_x = \infty$ is imposed, therefore in Equation (1) only y represent the curvilinear coordinate, x reduces to a straight coordinate axis. In addition, $f(z)$ is called the shear function that configures stress and strain distribution along the thickness of

Table 1 - Shear functions used in this study

Researcher	$f(z)$	Shell type
Touratier [45]	$\frac{h}{\pi} \sin\left(\frac{\pi}{h} z\right)$	Cylindrical+Spherical
Reddy [46]	$z\left(1 - \frac{4z^2}{3h^2}\right)$	Cylindrical+Spherical
Reissner [47]	$\frac{5z}{4}\left(1 - \frac{4z^2}{3h^2}\right)$	Cylindrical
Nguyen-Xuan et al. [48]	$\frac{7}{8}z - \frac{2}{h^2}z^3 + \frac{2}{h^4}z^5$	Cylindrical

the structure. Type of those functions can be noticed as polynomial, exponential or trigonometrical. In the current study, some of those functions used in analyses can be found in Table 1 where h refers to the section thickness:

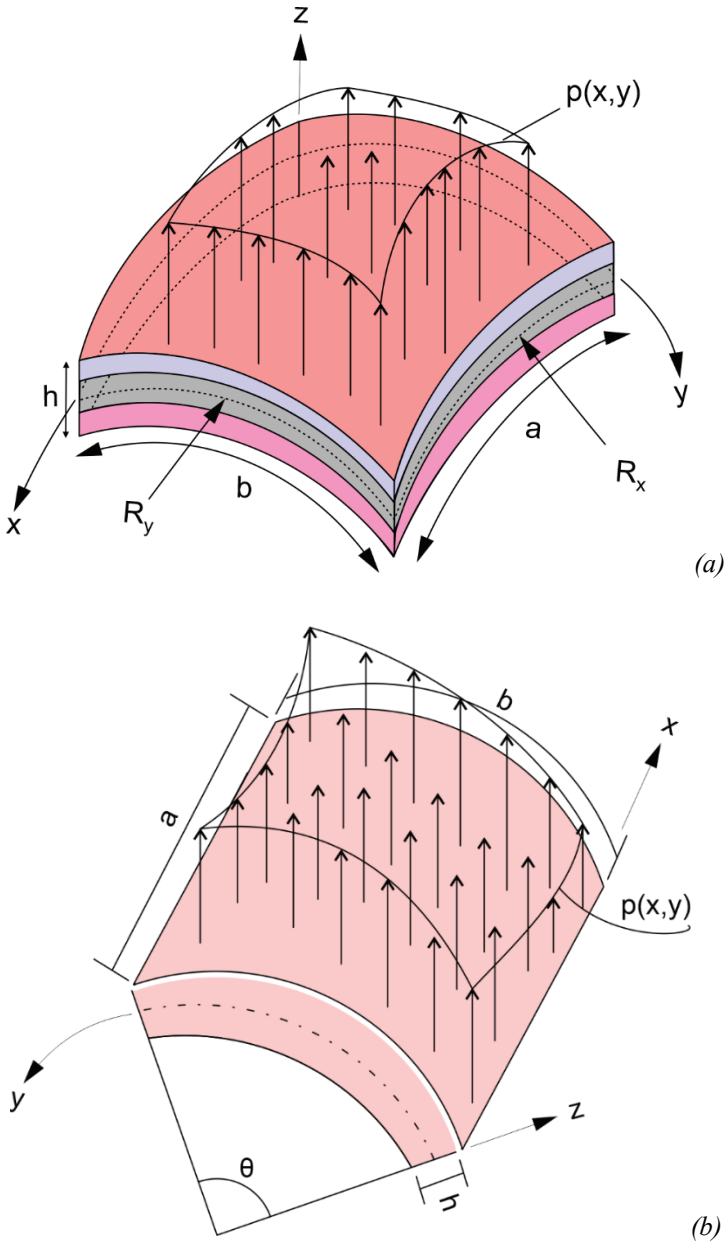


Figure 1 - a) Spherical shell coordinate system b) Cylindrical shell coordinate system

In an orthogonal curvilinear coordinate system, the engineering shear strain and linear normal components are expressed as follows [49]:

$$\begin{aligned}\varepsilon_i &= \frac{\partial}{\partial \xi_i} \left(\frac{u_i}{A_i} \right) + \frac{1}{A_i} \sum_{k=1}^3 \frac{u_k}{A_k} \frac{\partial A_i}{\partial \xi_k} \\ \gamma_{ij} &= \frac{1}{A_i A_j} \left[A_i^2 \frac{\partial}{\partial \xi_j} \left(\frac{u_i}{A_i} \right) + A_j^2 \frac{\partial}{\partial \xi_i} \left(\frac{u_j}{A_j} \right) \right] \quad (i \neq j)\end{aligned}\quad (2)$$

Where

$$\xi_3 = \zeta, \quad A_1 = a_1 \left(1 + \frac{\zeta}{R_1} \right), \quad A_2 = a_2 \left(1 + \frac{\zeta}{R_2} \right) \quad (3)$$

and a_α ($\alpha = 1, 2$) represent the square root of the surface metric tensor ($g_{\alpha\beta}$, $(\alpha, \beta = 1, 2)$), see Equation (4).

$$g_{\alpha\beta} = g_\alpha \cdot g_\beta, \quad a_\alpha = \sqrt{g_{\alpha\alpha}} \quad (4)$$

In Equation (4), g_1 and g_2 represent the tangent lines of the ξ_1 and ξ_2 axes, respectively.

The conversion of Reddy's [49] notation in the Equation (2) to the notation here is:

$$\begin{aligned}\xi_1 = x, \quad \xi_2 = y, \quad \zeta = z, \quad \varepsilon_1 = \varepsilon_{xx}, \quad \varepsilon_2 = \varepsilon_{yy}, \quad \varepsilon_3 = \varepsilon_{zz}, \quad u_1 = u, \quad u_2 = v, \quad u_3 = w \\ \gamma_{12} = \gamma_{xy}, \quad \gamma_{13} = \gamma_{xz}, \quad \gamma_{23} = \gamma_{yz}\end{aligned}\quad (5)$$

As a sum of above equations, the linear strain components are expressed by Equation (6).

$$\begin{aligned}\varepsilon_{xx} &= u_{,x} - z w_{,xx} + \frac{w}{R_x} + f(z) \theta_{x,x} \\ \varepsilon_{yy} &= v_{,y} - z w_{,yy} + \frac{w}{R_y} + f(z) \theta_{y,y} \\ \gamma_{xy} &= u_{,y}^* + v_{,x}^* = u_{,y} + v_{,x} - 2z w_{,xy} + f(z) (\theta_{x,y} + \theta_{y,x}) \\ \gamma_{yz} &= v_{,z}^* + w_{,y}^* = f_{,z}(z) \theta_y(x, y) \\ \gamma_{xz} &= u_{,z}^* + w_{,x}^* = f_{,z}(z) \theta_x(x, y)\end{aligned}\quad (6)$$

The relationship between strain measures and stress resultants is expressed over sectional compliance terms in explicit form as shown in Equation (7).

$$\begin{Bmatrix} u_{,x} + w/R_x \\ v_{,y} + w/R_y \\ u_{,y} + v_{,x} \\ -w_{,xx} \\ -w_{,yy} \\ -2w_{,xy} \\ \theta_{x,x} \\ \theta_{y,y} \\ \theta_{x,y} + \theta_{y,x} \\ \theta_y \\ \theta_x \end{Bmatrix} = \begin{bmatrix} A'_{11} & A'_{12} & A'_{16} & B'_{11} & B'_{12} & B'_{16} & E'_{11} & E'_{12} & E'_{16} & 0 & 0 \\ A'_{12} & A'_{22} & A'_{26} & B'_{12} & B'_{22} & B'_{26} & E'_{12} & E'_{22} & E'_{26} & 0 & 0 \\ A'_{16} & A'_{26} & A'_{66} & B'_{16} & B'_{26} & B'_{66} & E'_{16} & E'_{26} & E'_{66} & 0 & 0 \\ B'_{11} & B'_{12} & B'_{16} & D'_{11} & D'_{12} & D'_{16} & F'_{11} & F'_{12} & F'_{16} & 0 & 0 \\ B'_{12} & B'_{22} & B'_{26} & D'_{12} & D'_{22} & D'_{26} & F'_{12} & F'_{22} & F'_{26} & 0 & 0 \\ B'_{16} & B'_{26} & B'_{66} & D'_{16} & D'_{26} & D'_{66} & F'_{16} & F'_{26} & F'_{66} & 0 & 0 \\ E'_{11} & E'_{12} & E'_{16} & F'_{11} & F'_{12} & F'_{16} & H'_{11} & H'_{12} & H'_{16} & 0 & 0 \\ E'_{12} & E'_{22} & E'_{26} & F'_{12} & F'_{22} & F'_{26} & H'_{12} & H'_{22} & H'_{26} & 0 & 0 \\ E'_{16} & E'_{26} & E'_{66} & F'_{16} & F'_{26} & F'_{66} & H'_{16} & H'_{26} & H'_{66} & 0 & 0 \\ 0 & 0 & 0 & 0 & 0 & 0 & 0 & 0 & 0 & A'^s_{44} & A'^s_{45} \\ 0 & 0 & 0 & 0 & 0 & 0 & 0 & 0 & 0 & A'^s_{45} & A'^s_{55} \end{bmatrix} \begin{Bmatrix} N_{xx} \\ N_{yy} \\ N_{xy} \\ M_{xx} \\ M_{yy} \\ M_{xy} \\ M^f_{xx} \\ M^f_{yy} \\ M^f_{xy} \\ Q_{yz} \\ Q_{xz} \end{Bmatrix} \quad (7)$$

Details about the calculation of the sectional compliance terms ($A'_{ij}, B'_{ij}, D'_{ij}, E'_{ij}, F'_{ij}, H'_{ij}, A'^s_{ij}$) can be found in the laminated composite plate section of Bab [50]. The linear equilibrium equations for the spherical shell are as described below:

$$\begin{aligned} q_x + N_{xx,x} + N_{xy,y} &= 0 \quad ; \quad q_y + N_{xy,x} + N_{yy,y} = 0 \\ q_z + M_{xx,xx} + M_{yy,yy} + 2M_{xy,xy} - \frac{N_{xx}}{R_x} - \frac{N_{yy}}{R_y} &= 0 \end{aligned} \quad (8)$$

$$M^f_{xx,x} + M^f_{xy,y} - Q_{xz} = 0 \quad ; \quad M^f_{yy,y} + M^f_{xy,x} - Q_{yz} = 0$$

The boundary conditions for the spherical shell can be obtained as follows:

$$\begin{aligned} N_{xx}n_x + N_{xy}n_y &= 0 & \text{or } \delta u &= 0 \\ N_{xy}n_x + N_{yy}n_y &= 0 & \text{or } \delta v &= 0 \\ M_{xx,x}n_x + M_{yy,y}n_y + 2M_{xy,x}n_y &= 0 & \text{or } \delta w &= 0 \\ M^f_{xx}n_x + M^f_{xy}n_y &= 0 & \text{or } \delta \theta_x &= 0 \\ M^f_{xy}n_x + M^f_{yy}n_y &= 0 & \text{or } \delta \theta_y &= 0 \end{aligned} \quad (9)$$

According to the Hellinger-Reissner principle, the stationarity condition of the functional of a mechanical problem can be written as in Equation (10).

$$\delta \Pi_{HR} = \int_V (\boldsymbol{\varepsilon}^u - \boldsymbol{\varepsilon}^\sigma)^T \delta \boldsymbol{\sigma}^\sigma dV + \int_V \left((\boldsymbol{\sigma}^\sigma)^T \delta \boldsymbol{\varepsilon}^u - \mathbf{q}^T \delta \mathbf{u} \right) dV - \int_\Gamma \hat{\mathbf{t}}^T \delta \mathbf{u} d\Gamma = 0 \quad (10)$$

In Equation (10), the first integral corresponds to the weak form of the compatibility conditions of the strain field ($\boldsymbol{\varepsilon}$), while the second integral expresses the weak form of the equilibrium equations under external load \mathbf{q} under volume integral V . The last integral

shows the work done by the stresses ($\hat{\mathbf{t}}$) at the boundaries (Γ). As a result of using Equations (7) and (8) in Equation (10) and applying integration by parts to eliminate the doubly-differentiated terms, the final form of the functional becomes as follows:

$$\begin{aligned}
 & \int_A \left[u_x \frac{w}{R_x} - \frac{\left(A'_{11} N_{xx} + A'_{12} N_{yy} + A'_{16} N_{xy} + B'_{11} M_{xx} + B'_{12} M_{yy} + B'_{16} M_{xy} \right)}{\left(+E'_{11} M'_{xx} + E'_{12} M'_{yy} + E'_{16} M'_{xy} \right)} \right] \delta N_{xx} dA \\
 & + \int_A \left[v_y + \frac{w}{R_y} - \frac{\left(A'_{12} N_{xx} + A'_{22} N_{yy} + A'_{26} N_{xy} + B'_{12} M_{xx} + B'_{22} M_{yy} + B'_{26} M_{xy} \right)}{\left(+E'_{12} M'_{xx} + E'_{22} M'_{yy} + E'_{26} M'_{xy} \right)} \right] \delta N_{yy} dA \\
 & + \int_A \left[u_y + v_x - \frac{\left(A'_{16} N_{xx} + A'_{26} N_{yy} + A'_{66} N_{xy} + B'_{16} M_{xx} + B'_{26} M_{yy} + B'_{66} M_{xy} \right)}{\left(+E'_{16} M'_{xx} + E'_{26} M'_{yy} + E'_{66} M'_{xy} \right)} \right] \delta N_{xy} dA \\
 & + \int_A \left[w_{,x} \delta M_{xx,x} - \frac{\left(B'_{16} N_{xx} + B'_{26} N_{yy} + B'_{66} N_{xy} + D'_{16} M_{xx} + D'_{26} M_{yy} + D'_{66} M_{xy} \right)}{\left(+F'_{16} M'_{xx} + F'_{26} M'_{yy} + F'_{66} M'_{xy} \right)} \right] \delta M_{xx} dA \\
 & + \int_A \left[w_{,y} \delta M_{yy,y} - \frac{\left(B'_{12} N_{xx} + B'_{22} N_{yy} + B'_{26} N_{xy} + D'_{12} M_{xx} + D'_{22} M_{yy} + D'_{26} M_{xy} \right)}{\left(+F'_{12} M'_{xx} + F'_{22} M'_{yy} + F'_{26} M'_{xy} \right)} \right] \delta M_{yy} dA \\
 & + \int_A \left[w_{,x} \delta M_{xy,x} + w_{,y} \delta M_{xy,y} - \frac{\left(B'_{16} N_{xx} + B'_{26} N_{yy} + B'_{66} N_{xy} + D'_{16} M_{xx} + D'_{26} M_{yy} \right)}{\left(+D'_{66} M_{xy} + F'_{16} M'_{xx} + F'_{26} M'_{yy} + F'_{66} M'_{xy} \right)} \right] \delta M_{xy} dA \\
 & + \int_A \left[\theta_{x,x} - \frac{\left(E'_{11} N_{xx} + E'_{12} N_{yy} + E'_{16} N_{xy} + F'_{11} M_{xx} + F'_{12} M_{yy} + F'_{16} M_{xy} \right)}{\left(+H'_{11} M'_{xx} + H'_{12} M'_{yy} + H'_{16} M'_{xy} \right)} \right] \delta M'_{xx} dA \\
 & + \int_A \left[\theta_{y,y} - \frac{\left(E'_{12} N_{xx} + E'_{22} N_{yy} + E'_{26} N_{xy} + F'_{12} M_{xx} + F'_{22} M_{yy} + F'_{26} M_{xy} \right)}{\left(+H'_{12} M'_{xx} + H'_{22} M'_{yy} + H'_{26} M'_{xy} \right)} \right] \delta M'_{yy} dA \\
 & + \int_A \left[\theta_{x,y} + \theta_{y,x} - \frac{\left(E'_{16} N_{xx} + E'_{26} N_{yy} + E'_{66} N_{xy} + F'_{16} M_{xx} + F'_{26} M_{yy} + F'_{66} M_{xy} \right)}{\left(+H'_{16} M'_{xx} + H'_{26} M'_{yy} + H'_{66} M'_{xy} \right)} \right] \delta M'_{xy} dA \\
 & + \int_A \left[\theta_y - (A'_{44} Q_{,yz} + A'_{45} Q_{,xz}) \right] \delta Q_{,z} dA + \int_A \left[\theta_x - (A'_{45} Q_{,yz} + A'_{55} Q_{,xz}) \right] \delta Q_{,z} dA - \int_A \delta w q_z dA \\
 & + \int_A \left[N_{xx} \delta u_x + M_{xx,x} \delta w_x + M'_{xx} \delta \theta_{x,x} + N_{yy} \delta v_y + M_{yy,y} \delta w_y + M'_{yy} \delta \theta_{y,y} + N_{xy} \delta u_x \right] \\
 & + \int_A \left[+N_{xy} \delta v_x + M_{xy,x} \delta w_y + M_{xy,y} \delta w_x + M'_{xy} \delta \theta_{x,y} + M'_{xy} \delta \theta_{y,x} + Q_{,z} \delta \theta_y + Q_{,z} \delta \theta_x \right] dA \\
 & + \int_{A_1} (N_{xx} / R_x + N_{yy} / R_y) \delta w dA - \int_{\Gamma} \hat{t}_i \delta u_i d\Gamma = 0
 \end{aligned} \tag{11}$$

Two-dimensional four-node quadrilateral elements (Figure 2) with associated bi-linear shape functions are employed in finite element discretization. The interpolation of field variables occurs through local coordinates, denoted ξ and η , within the master element, where

$-1 \leq \xi \leq 1$ and $-1 \leq \eta \leq 1$. The computation involves numerical integrals over a transformation T_e from the master element domain Ω to the element domain Ω_e . The expression for the shape function family is provided by:

$$\varphi_i(\xi, \eta) = \frac{1}{4}(1 + \xi \xi_i)(1 + \eta \eta_i), \quad i = (1, \dots, 4) \quad (12)$$

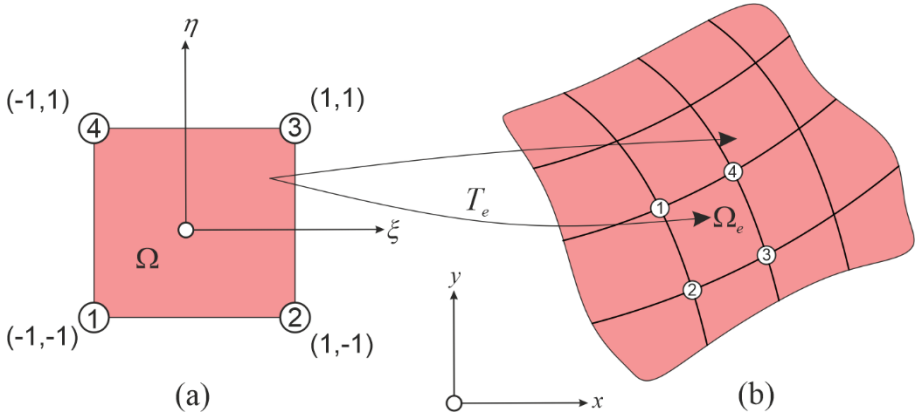


Figure 2 - Discretization of the shell domain (a) Master element in local coordinates (b) Shell domain in global coordinates

The resulting finite element system of equations of the laminated composite spherical shell can be represented in matrix form as follows:

$$\mathbf{KX} = \mathbf{F} \quad (13)$$

In Equation (13), \mathbf{K} denotes the system matrix, \mathbf{F} corresponds to the external force vector and \mathbf{X} is the vector that contains the unknowns.

$$\mathbf{X}^i = [u^i \ v^i \ w^i \ \theta_x^i \ \theta_y^i \ N_{xx}^i \ N_{yy}^i \ N_{xy}^i \ M_{xx}^i \ M_{yy}^i \ M_{xy}^i \ M_{xx}^f \ M_{yy}^f \ M_{xy}^f \ Q_{yz}^i \ Q_{xz}^i]^T \quad (14)$$

When the system equation is solved, both displacement and stress resultant variables can be obtained directly at the nodes without any necessity for any post-processing step.

3. NUMERICAL RESULTS

The mixed finite element formulation proposed for laminated composite spherical and cylindrical shells is named MHST (Mixed Higher-Order Shell Theory), and a series of numerical examples are discussed to demonstrate its performance and effectiveness in stress resultants and displacement calculations under static loading, and the results are evaluated. The solutions are produced through a Fortran-based program developed by the authors. By

making comparisons with Khdeir et al. [51], who analytically solved Higher Order Shear Theory (HSDT), First Order Theory (FSDT) and Classical Theory (CST), Asadi et al. [14], who made FSDT and 3D finite element analysis solutions, analytical HSDT solutions of Sayyad and Ghugal [10] and Mantari et al. [11], CUF by Giunta et al. [13] and numerical FSDT solution of Hossain et al. [4] in the literature; the accuracy of the formulation and the developed program is tested. Various element meshes as $n_e = 8 \times 8, 16 \times 16, 20 \times 20$ and 26×26 were used in the examples. Afterwards, solutions for different loading and support conditions were presented. There are two types of materials (Material A and B) used in the examples. The engineering constants of those materials can be seen in Table 2:

Table 2 - Sample materials and mechanical properties

Engineering Constants	Materials	
	A	B
E_1	132379340029 [Pa]	25[GPa]
E_2	10755821377 [Pa]	1[GPa]
E_3	10755821377 [Pa]	1[GPa]
ν_{12}	0.24	0.25
ν_{13}	0.24	0.25
ν_{23}	0.49	0.25
G_{12}	5653700980.4 [Pa]	0.5[GPa]
G_{13}	5653700980.4 [Pa]	0.5[GPa]
G_{23}	3605958064.3 [Pa]	0.2[GPa]

3.1. [0/90/0] Cylindrical Shell with Various Boundary Conditions under Sinusoidal Load

A symmetrically laminated cylindrical shell is analyzed using the proposed mixed finite element formulation and its results are compared with the literature. The shell is under the influence of transverse load of function $p(x, y) = p_0 \sin(\pi x/a) \sin(\pi y/b)$ distributed over its outer surface (see Figure 1b). Here a and b are the arc-lengths of the shell in the x and y axes directions, respectively (see Figure 3). The curvature in the cylindrical shell is on the y axis, so $R_x = \infty$. The cross section is defined with the [0/90/0] material orientation, and each layer of equal thickness is considered to be formed with material A. The $\rho = a/h = 10$ value is considered as the shell length-thickness ratio.

In Table 3, the SSSS boundary condition (BC) indicates that all four edges of the shell are simply supported. According to SCSC boundary condition, the two edges of the shell in the x -axis direction are simply supported, while the other two edges in the y -axis direction are clamped. In order to evaluate the results presented in Table 3 in a general structure, the following non-dimensionalization process is carried out:

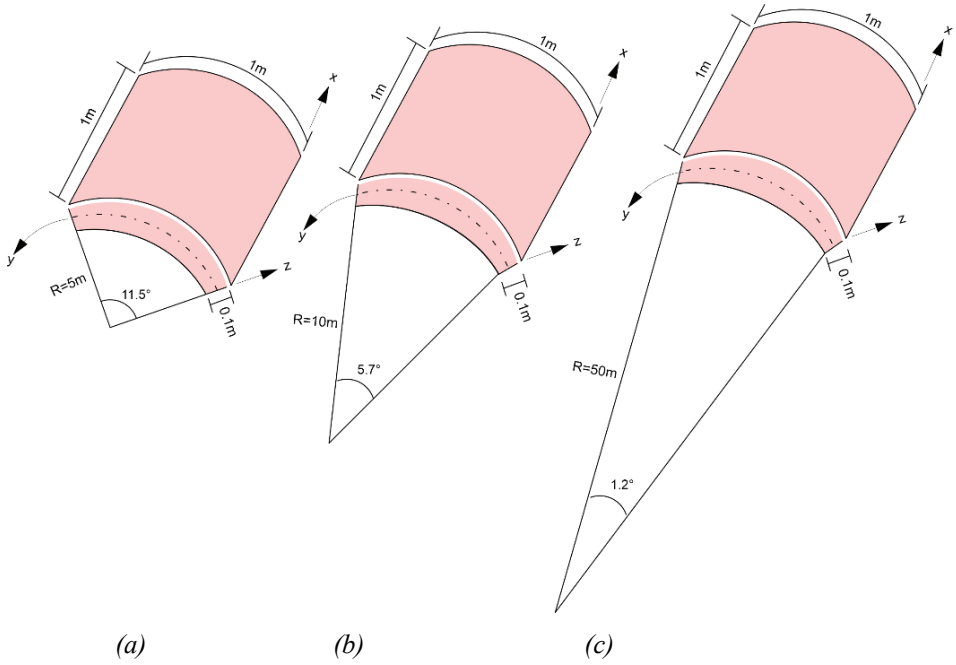


Figure 3 - The geometry of the cylindrical shells for (a) $R/a=5$ (b) $R/b=10$ (c) $R/a=50$

$$\bar{w} = \frac{10^2 E_2 h^3 w(a/2, b/2)}{p_0 a^4} \tag{15}$$

Table 3 - Convergence of laminated symmetrical cylindrical shell deflection under sinusoidal loading

BC'S	R/a	MHST (Touratier)				Khdeir et al. HSDT	HSDT – MHST percent Difference			
		8×8	16×16	20×20	26×26		8×8	16×16	20×20	26×26
SSSS	5	0.9354	0.9543	0.9561	0.9563	0.9524	1.78	-0.20	-0.39	-0.41
	10	0.9473	0.9668	0.9687	0.9689	0.9644	1.77	-0.25	-0.44	-0.47
	50	0.9512	0.9708	0.9728	0.9730	0.9683	1.77	-0.26	-0.46	-0.48
SCSC	5	0.4178	0.4200	0.4388	0.4407	0.4495	7.05	6.56	2.39	1.95
	10	0.4203	0.4346	0.4415	0.4435	0.4523	7.08	3.91	2.39	1.95
	50	0.4211	0.4395	0.4424	0.4444	0.4532	7.09	3.01	2.39	1.95

Table 4 - Deflection of the SSSS symmetrical cylindrical shell for several shear functions under sinusoidal loading

Formulation	Shear Function	R/a			MHST-HSDT percent Difference			
		5	10	50	5	10	50	
MHST (Present)	20×20	Reissner	0.9546	0.9671	0.9711	-0.23	-0.27	-0.29
		Reddy	0.9546	0.9671	0.9711	-0.23	-0.27	-0.29
		Nguyen	0.9573	0.9699	0.9740	-0.51	-0.57	-0.58
Khdeir et al.		HSDT	0.9524	0.9644	0.9683			
		FSDT	0.9432	0.9550	0.9588			
		CST	0.7615	0.7694	0.7720			

Table 5 - Deflection of the SCSC symmetrical cylindrical shell applying several shear functions under sinusoidal loading

Formulation	Shear Function	R/a			MHST-HSDT percent Difference			
		5	10	50	5	10	50	
MHST (Present)	26×26	Reissner	0.4400	0.4427	0.4436	2.12	2.12	2.12
		Reddy	0.4400	0.4427	0.4436	2.12	2.12	2.12
		Nguyen	0.4391	0.4418	0.4427	2.32	2.32	2.32
Khdeir et al.		HSDT	0.4495	0.4523	0.4424			
		FSDT	0.4357	0.4382	0.4391			
		CST	0.2047	0.2053	0.2055			

As can be seen in Table 3, the deflection values of the proposed numerical solution method (MHST) with the shear function of Touratier align very well with the Higher Order Theory (HSDT) results of the compared analytical method [51]. The results show consistent convergence behavior to an asymptotic value for both simply supported (SSSS) and mixed supported (SCSC) cases, however SSSS case demonstrates faster convergence behavior than SCSC (see Figures 4 and 5). The largest differences with the analytical results are seen in mixed supported case. That is why a finer mesh of 26×26 is applied. When the radius of the cylindrical shell increases, the percentage difference increases for the simply supported case, while it remains constant in the mixed supported case for the finer meshes (20×20 and 26×26). In Table 4, the deflection values of the SSSS symmetrical cylindrical shells (20×20) applying several shear functions under sinusoidal loading, are compared with Khdeir et al.'s analytical HSDT results. The percent differences of all the shear functions increase as the radius increases. The maximum MHST-HSDT percent difference (0.58) can be found in Nguyen Xuan et al.'s [48] shear function for the maximum radius. Therefore, 20×20 provides compatible results with the reference solution. In Table 5, the deflection values of the SCSC symmetrical cylindrical shells (26×26) applying several shear functions under sinusoidal loading, are compared with analytical results. Table 5 showed that both Reddy's [46] and Reissner's [47] shear functions produced uniform results (2.12 percent

difference from Khdeir et al. results), whereas the utilization of Nguyen Xuan et al.'s [48] shear function produced 2.32 percent difference for the same comparison parameter.

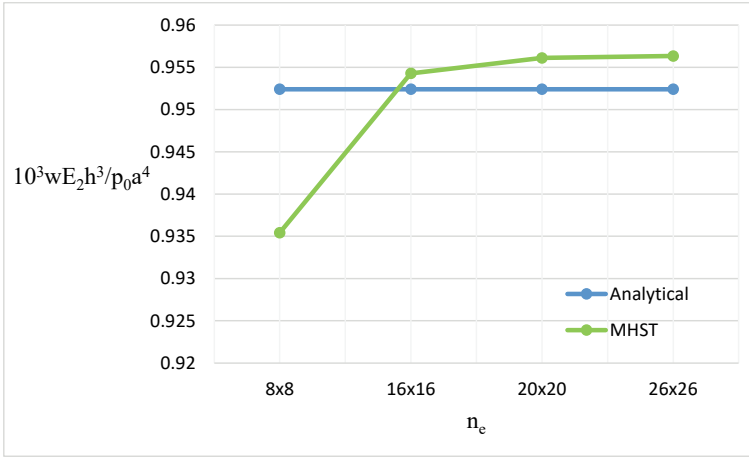


Figure 4 - The convergence behavior for the SSSS case

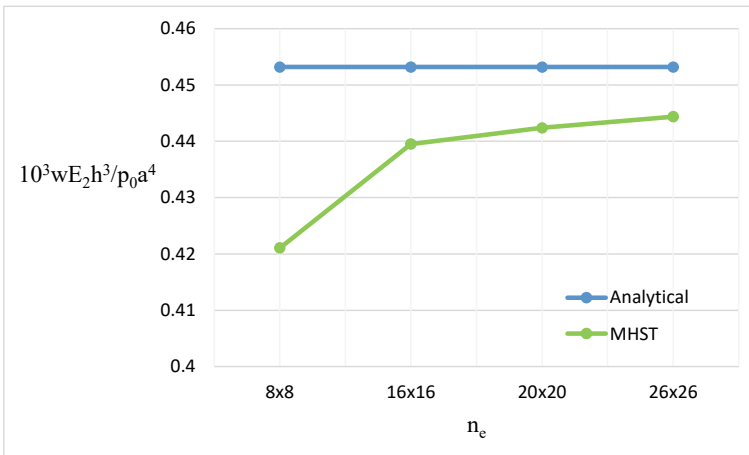


Figure 5 - The convergence behavior for the SCSC case

3.2. [0/90/0] Simply Supported Cylindrical Shell under Uniform Load

Uniformly $p(x) = p_0$ loaded simply supported cylindrical shells with [0/90/0] layouts are discussed in this section. In Table 6, MHST solutions in terms of the displacement, normal force, and moment values at the midpoint of the shell formed with material B are presented. The results obtained with the element meshes of 8x8, 16x16 and 20x20 for various thickness ratios ($\rho = a/h = 10, 20$) (see Figure 6) are compared with the FSDT and ANSYS

3D finite element solutions of Asadi et al. [14]. The non-dimensionalization of the values given in Table 6 is as follows:

$$\bar{w} = \frac{10^3 E_2 h^3 w(a/2, b/2)}{p_0 a^4}, \quad \bar{M} = \frac{10^3 M(a/2, b/2)}{p_0 a^2}, \quad \bar{N} = \frac{10^3 N(a/2, b/2)}{p_0 a^3} \quad (16)$$

Table 6 - Deflection and stress resultants in a uniformly loaded cylindrical shell

a/h	a/R	Theory	\bar{w}	\bar{M}_{xx}	\bar{M}_{yy}	\bar{N}_{xx}	\bar{N}_{yy}	3D-MHST Difference (percent)				
								\bar{w}	\bar{M}_{xx}	\bar{M}_{yy}	\bar{N}_{xx}	\bar{N}_{yy}
20	0.5	8×8	6.2771	104.04	7.41	587.56	576.78	1.57	2.15	4.05	1.43	0.01
		16×16	6.2533	102.76	7.35	583.04	573.50	1.94	0.89	4.72	2.18	0.58
		20×20	6.2477	102.55	7.35	582.54	572.92	2.03	0.68	4.72	2.27	0.68
		FSDT	6.1282	103.42	6.96	571.68	559.67					
		3D	6.3773	101.85	7.72	596.06	576.85					
20	1	8×8	3.9190	64.18	3.36	737.56	723.53	0.29	3.08	13.8	0.08	0.62
		16×16	3.8617	62.77	3.33	723.96	713.41	1.74	0.83	12.7	1.92	0.79
		20×20	3.8551	62.600	3.33	722.75	712.23	1.91	0.55	12.8	2.08	0.95
		FSDT	3.8314	63.908	2.71	718.62	708.66					
		3D	3.9303	62.260	2.95	738.14	719.09					
10	0.5	8×8	10.147	114.89	12.5	237.62	223.68	4.82	2.08	10.0	4.87	0.52
		16×16	10.123	113.46	12.6	236.09	221.92	5.05	0.81	9.20	5.48	0.27
		20×20	10.116	113.26	12.5	235.94	221.69	5.11	0.63	9.27	5.54	0.37
		FSDT	9.5092	115.46	11.3	222.26	202.12					
		3D	10.661	112.55	13.9	249.78	222.52					
10	1	8×8	8.2035	92.73	9.44	385.00	360.39	5.05	1.52	1.21	5.01	0.69
		16×16	8.1411	91.13	9.51	380.49	356.33	5.77	0.23	0.48	6.12	1.81
		20×20	8.1319	90.930	9.50	380.08	355.86	5.88	0.45	0.57	6.22	1.94
		FSDT	7.8418	95.117	7.94	367.19	335.23					
		3D	8.6399	91.340	9.56	405.29	362.88					

Table 6 shows that the results obtained from the current formulation (MHST) are highly compatible with the 3D solution. MHST results also exhibit a consistent convergence behavior depending on the increasing number of elements. It can be pointed out that when the shell becomes thinner, the differences (3D-MHST) in deflection values decrease. Among the stress resultants, the highest correlation is observed between \bar{M}_{xx} values, whereas the

least correlation exists between \overline{M}_{yy} values. This is an expected result because the shell curvature lies on the y -axis. Considering all comparison results, all predictions (except \overline{M}_{yy} at $a/h=20$ and $a/R=1$) of MHST are in a better agreement with 3D solution compared to the predictions of the FSDT.

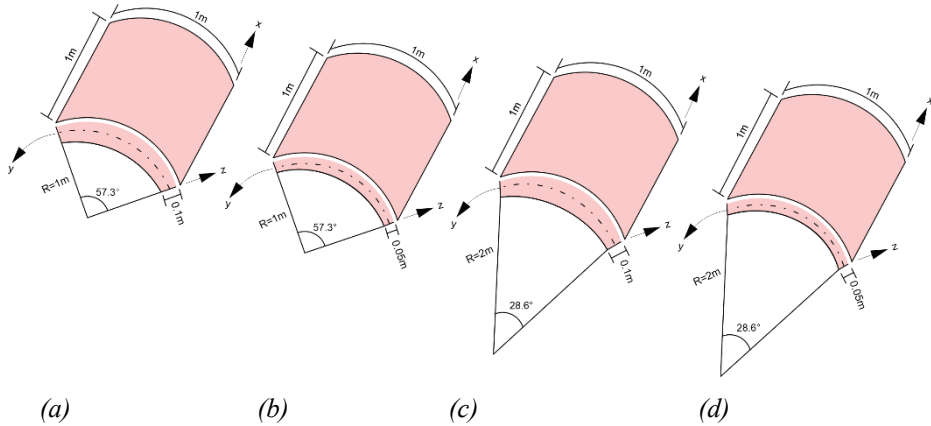


Figure 6 - The geometry of the cylindrical shells for (a) $R/a=1$ and $a/h=10$ (b) $R/a=1$ and $a/h=20$ (c) $R/a=2$ and $a/h=10$ (d) $R/a=2$ and $a/h=20$

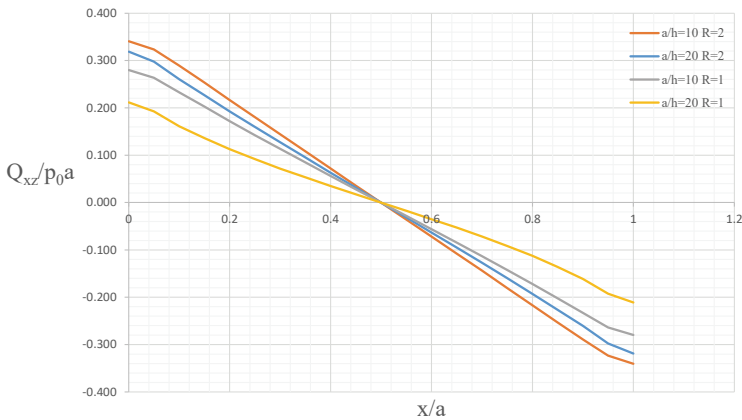


Figure 7 - Shear force distribution along the x -axis ($y=0.5$) in a simply supported symmetrical laminated cylindrical shell under uniform load (material B)

By exploiting the advantage of mixed finite element formulation, stress resultants are directly obtained at the nodes of the shell structures and presented in Figures 7-9. Figure 7 shows the shear force distribution in a uniformly loaded and simply supported laminated composite cylindrical shell discretized with 20×20 elements. The shear force becomes zero at the

symmetry axis as expected and takes varying values depending on the thickness ratio and radius of curvature. With increasing radius of curvature R_y , the shell behaves more like a plate so the absolute value of the shear force increases. Additionally, with increasing thickness, the shear force becomes more effective and has greater absolute values as can be easily followed in Figure 7.

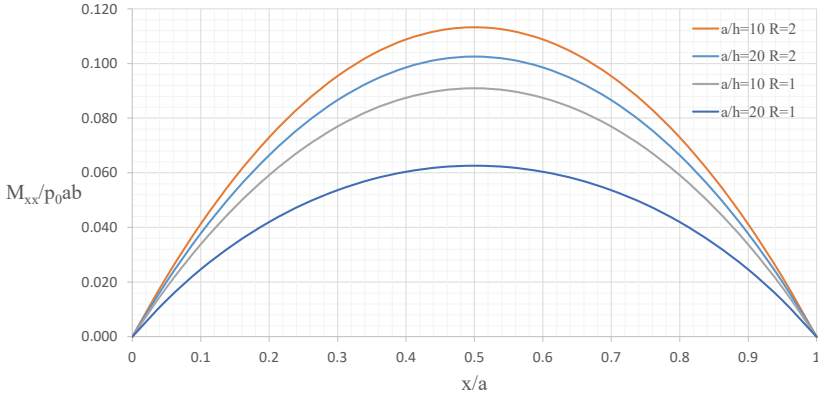


Figure 8 - Moment distribution along the x -axis ($y=0.5$) in a simply supported symmetrical laminated cylindrical shell under uniform load (material B)

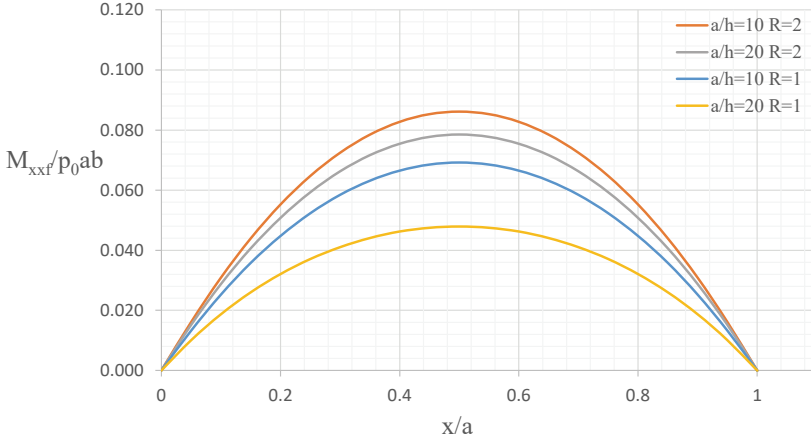


Figure 9 - Higher order moment distribution along the x -axis ($y=0.5$) in a simply supported symmetrical laminated cylindrical shell under uniform load (material B)

In the same shell problem, the moment distribution for different thickness ratios is given in Figure 8. In this distribution, dimensionless moment values for all thickness ratios demonstrate similar behavior to the shear force values given in Figure 7. The highest moment

value is obtained in the shell with the least curvature and the greatest thickness, while the lowest moment value is obtained in the thinnest shell structure with the highest curvature.

Higher-order moment distributions for the same shell with different thickness ratios are presented in Figure 9. High-order moment values along the shell's length are considerably lower than the normal moment values, but their distribution concerning thickness and radius is similar to that of the normal moment.

In Figures 10 and 11, dimensionless moment and shear force distributions for $\rho=10$ and $R=1$ are given for the entire domain. Since the curvature of the cylindrical shell is on the y -axis, the difference between \overline{M}_{xx} and \overline{M}_{yy} in Figure 10 and the difference between \overline{Q}_{xz} and \overline{Q}_{yz} in Figure 11 can be easily seen.

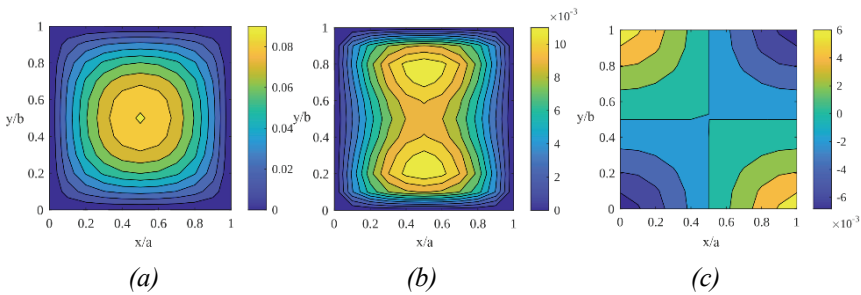


Figure 10 - Moment distribution on the $x - y$ axes for the symmetrical simply supported laminated cylindrical shell ($\rho=10$ and $R=1$) under uniform load, respectively (a) \overline{M}_{xx} distribution (b) \overline{M}_{yy} distribution (c) \overline{M}_{xy} distribution

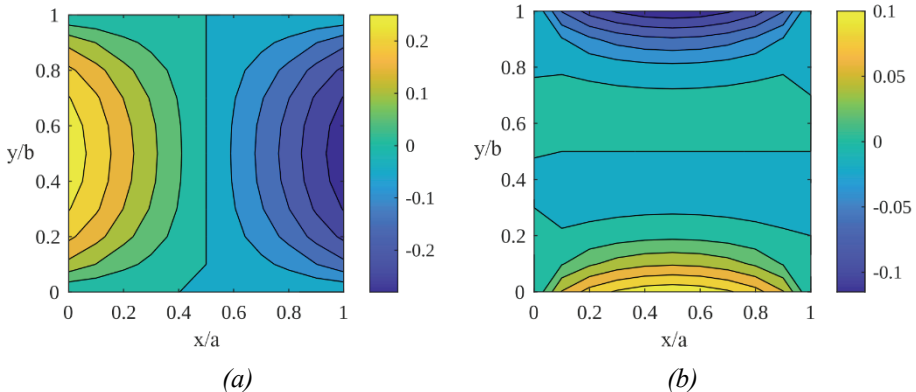


Figure 11 - Shear force distribution on the $x - y$ axes for the symmetrical simply supported laminated cylindrical shell ($\rho=10$ and $R=1$) under uniform load, respectively (a) \overline{Q}_{xz} distribution (b) \overline{Q}_{yz} distribution

3.3. [0/90/0] Simply Supported Spherical Shell under Sinusoidal Load

In this part, simply supported symmetrically laminated [0/90/0] spherical shells are statically investigated applying sinusoidal load ($p(x, y) = p_0 \sin(\pi x/a) \sin(\pi y/b)$). The spherical shell geometries are selected as $\rho = 10$ and $\rho = 100$ and the material is chosen as B (Table 2). R/a ratio is defined as 5, 10 and 100. The finest element mesh (20×20) is employed for the all deflection results. Reddy’s and Touratier’s shear functions are selected for the current analyses. The solutions are compared with PSDT (parabolic shear deformation theory which corresponds Reddy’s shear function) and TSDT (trigonometric shear deformation theory which corresponds Touratier’s shear function) conducted by Sayyad and Ghugal [10], analytical HSDT of Mantari et al. [11], CUF of Giunta et al. [13] and numerical FSDT solution of Hossain et al. [4].

Table 7 - Deflection values for simply supported sinusoidally loaded spherical shell

a/h	R/a	MHST 20×20		Sayyad and Ghugal		Mantari et al.	Giunta et al.	Hossain et al.
		Reddy	Touratier	PSDT	TSDT			
10	5	0.6745	0.6794	0.6769	0.6819	0.6964	0.7312	0.6600
	10	0.7006	0.7060	0.7032	0.7086	0.7244	0.7497	0.6702
100	100	0.7097	0.7152	0.7124	0.7179	0.7341	-	0.6699
	5	0.1031	0.1031	0.1032	0.1032	0.1032	0.1036	0.1035
	10	0.2405	0.2405	0.2410	0.2410	0.2413	0.2416	0.2415
	100	0.4291	0.4292	0.4307	0.4307	0.4318	-	0.4303

It can be concluded from Table 7 that current formulation’s deflection values are match well all referenced solutions. The most consistent results can be mentioned as MHST(Reddy)-PSDT and MHST(Touratier)-TSDT. This is a predictable solution due to the utilization of the same shear functions.

3.4. [0/90/0] Simply Supported Spherical Shell under Uniform Load

In this section, the problem specified in Section 3.3 is solved under uniform loading condition. The spherical shell thickness ratio is selected as $\rho = 10$. $R/a = 20$ and $R/a = 50$ ratios are considered to examine different geometric configurations. In Table 8, the results are compared with Sayyad and Ghugal and the percent differences are specified for MHST(Reddy)-PSDT and MHST(Touratier)-TSDT. The percentage differences in both comparisons are almost identical. A slight difference is observed when the R/a ratio is increased from 20 to 100.

Table 8 - Deflection values for simply supported uniformly loaded spherical shell

a/h	R/a	MHST 20 x 20		Sayyad and Ghugal		Percent Differences	
		Reddy	Touratier	PSDT	TSDT	Reddy-PSDT	Touratier-TSDT
10	5	1.0344	1.0422	1.0333	1.0411	0.11	0.11
	10	1.0763	1.0848	1.0752	1.0837	0.10	0.10
	20	1.0872	1.0959	1.0862	1.0949	0.10	0.09
	50	1.0904	1.0991	1.0894	1.0980	0.09	0.10
	100	1.0908	1.0995	1.0898	1.0985	0.09	0.89

4. CONCLUSION

In this study, the displacement and stress resultant distributions of laminated composite spherical and cylindrical shells under different boundary and loading conditions are examined. For this purpose, a mixed finite element method is adopted based on the Higher Order Shear Theory. Four different shear functions are considered for the Higher Order Theory. Finite element equations obtained using the Hellinger-Reissner variational principle are discretized using two-dimensional four-node elements with C_0 continuity. As an advantage of the mixed finite element method, force and moment components, as well as displacement type field variables can be calculated directly at the nodes. Convergence and comparison analyses are performed on the problems discussed and it was observed that the results are in good agreement with the reference analytical, numerical and 3D solutions. In addition, taking into account different thickness and depth characteristics of the cylindrical composite shell; shear force, moment and higher order moment values are compared. It has been observed that the results obtained for the current formulation are highly compatible with many advanced finite element solutions featured in the literature and sometimes produce better results, especially in moment calculations. It is thought that the proposed formulation offers the opportunity to be developed for many types of analysis in the future and adapted to various problems.

Symbols

$\delta \Pi_{HR}$: First variation of the functional
a	: Shell length
b	: Shell width
$\boldsymbol{\varepsilon}^u$: Strain vector in terms of displacement components
$\boldsymbol{\varepsilon}^\sigma$: Strain vector in terms of the stress components
$\boldsymbol{\sigma}^\sigma$: Stress vector
δ	: Variational operator
$\hat{\mathbf{t}}$: Traction vector
Γ	: Boundary of the structure

E_1, E_2, E_3	: Young's moduli
ν_{ij}	: Poison's ratio
G_α	: Shear moduli ($\alpha = 23, 31, 12$)
$f(z)$: Shear functions
h	: Thickness
z	: Any coordinate along the thickness
$\theta_x(x)$: Shear rotation about y axis
$\theta_y(x)$: Shear rotation about y axis
σ_{ii}	: In-plane stress components
σ_{ij}	: Transverse shear stress components
N_{ii}	: In-plane force resultant of stress components
M_{ii}	: Resultant moment of stress components
M_{ii}^f	: Resultant higher order moment of stress components
Q_{ij}	: Resultants of transverse shear stress components
\mathbf{e}^u	: Strain measures in terms of kinematical variables
\mathbf{E}	: Section stiffness matrix
\mathbf{e}^p	: Strain measures in terms of stress resultants
\mathbf{F}	: External force vector
\mathbf{K}	: System matrix
\mathbf{p}	: Applied load vector
\mathbf{P}	: Stress resultants
\mathbf{X}	: Unknown vector

References

- [1] M. Dorduncu, Peridynamic modeling of delaminations in laminated composite beams using refined zigzag theory, *Theoretical and Applied Fracture Mechanics* 112 (2021) 102832. <https://doi.org/10.1016/j.tafmec.2020.102832>.
- [2] M. Dorduncu, Stress analysis of laminated composite beams using refined zigzag theory and peridynamic differential operator, *Composite Structures* 218 (2019) 193–203. <https://doi.org/10.1016/j.compstruct.2019.03.035>.
- [3] J.N. Reddy, K. Chandrashekhara, Geometrically non-linear transient analysis of laminated, doubly curved shells, *International Journal of Non-Linear Mechanics* 20 (1985) 79–90. [https://doi.org/10.1016/0020-7462\(85\)90002-2](https://doi.org/10.1016/0020-7462(85)90002-2).

- [4] S.J. Hossain, P.K. Sinha, A.H. Sheikh, A finite element formulation for the analysis of laminated composite shells, *Computers & Structures* 82 (2004) 1623–1638. <https://doi.org/10.1016/j.compstruc.2004.05.004>.
- [5] E. Asadi, M.S. Qatu, Static analysis of thick laminated shells with different boundary conditions using GDQ, *Thin-Walled Structures* 51 (2012) 76–81. <https://doi.org/10.1016/j.tws.2011.11.004>.
- [6] A.A. Khdeir, Comparative dynamic and static studies for cross-ply shells based on a deep thick shell theory, *IJVNV* 7 (2011) 306. <https://doi.org/10.1504/IJVNV.2011.043192>.
- [7] S.M. Mousavi, M. Aghdam, Static bending analysis of laminated cylindrical panels with various boundary conditions using the differential cubature method, *J. Mech. Mater. Struct.* 4 (2009) 509–521. <https://doi.org/10.2140/jomms.2009.4.509>.
- [8] B. Sobhaniragh, R.C. Batra, W.J. Mansur, F.C. Peters, Thermal response of ceramic matrix nanocomposite cylindrical shells using Eshelby-Mori-Tanaka homogenization scheme, *Composites Part B: Engineering* 118 (2017) 41–53. <https://doi.org/10.1016/j.compositesb.2017.02.032>.
- [9] J.N. Reddy, C.F. Liu, A higher-order shear deformation theory of laminated elastic shells, *International Journal of Engineering Science* 23 (1985) 319–330. [https://doi.org/10.1016/0020-7225\(85\)90051-5](https://doi.org/10.1016/0020-7225(85)90051-5).
- [10] A.S. Sayyad, Y.M. Ghugal, Static and free vibration analysis of laminated composite and sandwich spherical shells using a generalized higher-order shell theory, *Composite Structures* 219 (2019) 129–146. <https://doi.org/10.1016/j.compstruc.2019.03.054>.
- [11] J.L. Mantari, A.S. Oktem, C. Guedes Soares, Static and dynamic analysis of laminated composite and sandwich plates and shells by using a new higher-order shear deformation theory, *Composite Structures* 94 (2011) 37–49. <https://doi.org/10.1016/j.compstruc.2011.07.020>.
- [12] A. Kumar, A. Chakrabarti, M. Ketkar, Analysis of laminated composite skew shells using higher order shear deformation theory, *Lat. Am. j. Solids Struct.* 10 (2013) 391–919. <https://doi.org/10.1590/S1679-78252013000500003>.
- [13] G. Giunta, F. Biscani, S. Belouettar, E. Carrera, Hierarchical modelling of doubly curved laminated composite shells under distributed and localised loadings, *Composites Part B* 42 (2011) 682–91. <https://doi.org/10.1016/j.compositesb.2011.02.002>.
- [14] E. Asadi, W. Wang, M.S. Qatu, Static and vibration analyses of thick deep laminated cylindrical shells using 3D and various shear deformation theories, *Composite Structures* 94 (2012) 494–500. <https://doi.org/10.1016/j.compstruc.2011.08.011>.
- [15] H.L. Ton-That, H. Nguyen-Van, T. Chau-Dinh, An Improved Four-Node Element for Analysis of Composite Plate/Shell Structures Based on Twice Interpolation Strategy, *Int. J. Comput. Methods* 17 (2020) 1950020. <https://doi.org/10.1142/S0219876219500208>.

- [16] H. Zuo, Y. Chen, F. Jia, Z. Yang, Unified wavelet finite element formulation for static and vibration analysis of laminated composite shells, *Composite Structures* 272 (2021) 114207. <https://doi.org/10.1016/j.compstruct.2021.114207>.
- [17] M. Yaghoubsahi, E. Asadi, S.J. Fariborz, A higher-order shell model applied to shells with mixed boundary conditions, *Proceedings of the Institution of Mechanical Engineers, Part C: Journal of Mechanical Engineering Science* 225 (2011) 292–303. <https://doi.org/10.1243/09544062JMES2050>.
- [18] R.M.J. Groh, P.M. Weaver, Static inconsistencies in certain axiomatic higher-order shear deformation theories for beams, plates and shells, *Composite Structures* 120 (2015) 231–245. <https://doi.org/10.1016/j.compstruct.2014.10.006>.
- [19] K. Bhaskar, T.K. Varadan, A higher-order theory for bending analysis of laminated shells of revolution, *Computers & Structures* 40 (1991) 815–819. [https://doi.org/10.1016/0045-7949\(91\)90310-I](https://doi.org/10.1016/0045-7949(91)90310-I).
- [20] T.N. Doan, D. Van Thom, N.T. Thanh, P. Van Chuong, N.C. Tho, N.T. Ta, H.N. Nguyen, Analysis of stress concentration phenomenon of cylinder laminated shells using higher-order shear deformation Quasi-3D theory, *Composite Structures* 232 (2020) 111526. <https://doi.org/10.1016/j.compstruct.2019.111526>.
- [21] E. Viola, F. Tornabene, N. Fantuzzi, Static analysis of completely doubly-curved laminated shells and panels using general higher-order shear deformation theories, *Composite Structures* 101 (2013) 59–93. <https://doi.org/10.1016/j.compstruct.2013.01.002>.
- [22] I.F. Pinto Correia, C.M. Mota Soares, C.A. Mota Soares, J. Herskovits, Analysis of laminated conical shell structures using higher order models, 62 (2003) 383–390. <https://doi.org/10.1016/j.compstruct.2003.09.009>.
- [23] F. Tornabene, N. Fantuzzi, E. Viola, R.C. Batra, Stress and strain recovery for functionally graded free-form and doubly-curved sandwich shells using higher-order equivalent single layer theory, *Composite Structures* 119 (2015) 67–89. <https://doi.org/10.1016/j.compstruct.2014.08.005>.
- [24] M. Yaqoob Yasin, S. Kapuria, An efficient layerwise finite element for shallow composite and sandwich shells, *Composite Structures* 98 (2013) 202–214. <https://doi.org/10.1016/j.compstruct.2012.10.048>.
- [25] A. Gupta, S. Pradyumna, Geometrically nonlinear bending analysis of variable stiffness composite laminated shell panels with a higher-order theory, *Composite Structures* 276 (2021) 114527. <https://doi.org/10.1016/j.compstruct.2021.114527>.
- [26] G.M. Kulikov, S.V. Plotnikova, Advanced formulation for laminated composite shells: 3D stress analysis and rigid-body motions, *Composite Structures* 95 (2013) 236–246. <https://doi.org/10.1016/j.compstruct.2012.07.020>.
- [27] M.S. Qatu, A. Algothani, Bending analysis of laminated plates and shells by different methods, *Computers & Structures* 52 (1994) 529–539. [https://doi.org/10.1016/0045-7949\(94\)90238-0](https://doi.org/10.1016/0045-7949(94)90238-0).

- [28] E.E. Karataş, R.F. Yükseler, Snap-through Buckling of Shallow Spherical Shells under Ring Loads, *Teknik Dergi* 32 (2021) 10695–10716. <https://doi.org/10.18400/tekderg.565095>.
- [29] A. Sofiyev, A. Deniz, M. Avcar, P. Özyigit, M. Omurtag, Effects of the non-homogeneity and elastic medium on the critical torsional load of the orthotropic cylindrical shell footnotemark, *Acta Physica Polonica A* 123 (2013) 728–730.
- [30] A. Yadav, M. Amabili, S. Kumar Panda, T. Dey, Instability analysis of fluid-filled angle-ply laminated circular cylindrical shells subjected to harmonic axial loading | Elsevier Enhanced Reader, *European Journal of Mechanics - A/Solids* 97 (2023). <https://doi.org/10.1016/j.euromechsol.2022.104810>.
- [31] M.C. Ray, Exact solutions of elasticity theories for static analysis of doubly curved antisymmetric angle-ply composite shells, *Mechanics of Advanced Materials and Structures* (2023) 1–15. <https://doi.org/10.1080/15376494.2023.2246223>.
- [32] Md.I. Alam, M.K. Pandit, A.K. Pradhan, A modified higher-order zigzag theory for predicting flexural behavior of laminated composite and sandwich shell, *Mechanics of Advanced Materials and Structures* (2023) 1–16. <https://doi.org/10.1080/15376494.2023.2231445>.
- [33] A.B. Arumugam, M. Subramani, M. Dalakoti, P. Jindal, R. Selvaraj, E. Khalife, Dynamic characteristics of laminated composite CNT reinforced MRE cylindrical sandwich shells using HSDT, *Mechanics Based Design of Structures and Machines* 51 (2023) 4120–4136. <https://doi.org/10.1080/15397734.2021.1950550>.
- [34] A. Ozutok, E. Madenci, Static analysis of laminated composite beams based on higher-order shear deformation theory by using mixed-type finite element method, *Int. J. Mech. Sci.* 130 (2017) 234–243. <https://doi.org/10.1016/j.ijmecsci.2017.06.013>.
- [35] A. Kutlu, M. Dorduncu, T. Rabczuk, A novel mixed finite element formulation based on the refined zigzag theory for the stress analysis of laminated composite plates, *Composite Structures* 267 (2021) 113886. <https://doi.org/10.1016/j.compstruct.2021.113886>.
- [36] A. Kutlu, Mixed finite element formulation for bending of laminated beams using the refined zigzag theory, *Proceedings of the Institution of Mechanical Engineers, Part L: Journal of Materials: Design and Applications* 235 (2021) 1712–1722. <https://doi.org/10.1177/14644207211018839>.
- [37] A. Kutlu, G. Meschke, M.H. Omurtag, A new mixed finite-element approach for the elastoplastic analysis of Mindlin plates, *J Eng Math* 99 (2016) 137–155. <https://doi.org/10.1007/s10665-015-9825-7>.
- [38] U.N. Aribas, M. Ermis, N. Eratli, M.H. Omurtag, The static and dynamic analyses of warping included composite exact conical helix by mixed FEM | Elsevier Enhanced Reader, *Composites Part B: Engineering* 160 (2019) 285–297. <https://doi.org/10.1016/j.compositesb.2018.10.018>.

- [39] U.N. Aribas, M. Ermis, A. Kutlu, N. Eratli, M.H. Omurtag, Forced vibration analysis of composite-geometrically exact elliptical cone helices via mixed FEM, *Mechanics of Advanced Materials and Structures* (2020) 1–19. <https://doi.org/10.1080/15376494.2020.1824048>.
- [40] U.N. Aribas, M. Ermis, M.H. Omurtag, The static and stress analyses of axially functionally graded exact super-elliptical beams via mixed FEM, *Arch Appl Mech* 91 (2021) 4783–4796. <https://doi.org/10.1007/s00419-021-02033-w>.
- [41] A. Kutlu, M. Hakkı Omurtag, Large deflection bending analysis of elliptic plates on orthotropic elastic foundation with mixed finite element method, *International Journal of Mechanical Sciences* 65 (2012) 64–74. <https://doi.org/10.1016/j.ijmecsci.2012.09.004>.
- [42] M.H. Omurtag, A.Y. Aköz, Isoparametric mixed finite element formulation of orthotropic cylindrical shells, *Computers & Structures* 55 (1995) 915–924. [https://doi.org/10.1016/0045-7949\(94\)00450-H](https://doi.org/10.1016/0045-7949(94)00450-H).
- [43] Y. Bab, A. Kutlu, Mixed finite element formulation based on higher order theory for stress calculation of laminated composite beams, in: *Proceedings 22. National Mechanics Congress, Adana, Turkey, 2021*.
- [44] Y. Bab, A. Kutlu, Stress analysis of laminated HSDT beams considering bending extension coupling, *Turkish Journal of Civil Engineering* 34 (2023) 1–23. <https://doi.org/10.18400/tjce.1206777>.
- [45] M. Touratier, An efficient standard plate theory, *International Journal of Engineering Science* 29 (1991) 901–916. [https://doi.org/10.1016/0020-7225\(91\)90165-Y](https://doi.org/10.1016/0020-7225(91)90165-Y).
- [46] J.N. Reddy, A simple higher-order theory for laminated composite plates, *Journal of Applied Mechanics* 51 (1984) 745–752. <https://doi.org/10.1115/1.3167719>.
- [47] E. Reissner, On transverse bending of plates, including the effect of transverse shear deformation, *International Journal of Solids and Structures* 11 (1974) 569–573.
- [48] H. Nguyen-Xuan, C.H. Thai, T. Nguyen-Thoi, Isogeometric finite element analysis of composite sandwich plates using a higher order shear deformation theory, *Composites Part B: Engineering* 55 (2013) 558–574. <https://doi.org/10.1016/j.compositesb.2013.06.044>.
- [49] J.N. Reddy, *Mechanics of Laminated Composite Plates and Shells*, CRC Press, Boca Raton, 2003.
- [50] Y. Bab, Mixed finite element formulations for laminated beams and plates based on higher order shear deformation theories, Master's Thesis, Istanbul Technical University, 2021.
- [51] A.A. Khdeir, L. Librescu, D. Frederick, A shear deformable theory of laminated composite shallow shell-type panels and their response analysis II: Static response, *Acta Mechanica* 77 (1989) 1–12. <https://doi.org/10.1007/BF01379740>.

A Critical Evaluation of the Coefficient Method, Capacity Spectrum Method and Modal Pushover Analysis for Irregular Steel Buildings in Seismic Zones

Vahid MOKARRAM^{1*}
Mahmoud Reza BANAN²
Mohammad Reza BANAN³
Abdollah KHEYRI⁴



ABSTRACT

Classical design procedures are less advantageous than performance-based seismic design (PBSD) of buildings, which is included in existing standards such as ASCE 41-23 for new buildings or retrofitting. PBSD requires accurate assessment of building seismic responses. Such assessments can be done using either faster nonlinear static procedures (NSPs) or more time-intensive nonlinear time-history analyses (NTHAs). However, the reliability of NSPs can be questionable, as shown by previous research. Practitioners need to conduct further investigations to determine safety margins and the applicability scope of these methods. This is especially important for irregular buildings and near-fault zones. This problem is investigated in this paper by first using 1250 single-degree-of-freedom (SDOF) systems to evaluate the ASCE 41-23's coefficient method and performing 25000 NTHAs for near- and far-fault records. Second, the responses obtained from two alternative approaches, the modal pushover analysis (MPA) and FEMA 440's capacity spectrum method (CSM), are compared with NTHA responses for buildings with significant higher-mode effects. American standards are used to design 96 3D symmetric and asymmetric steel moment-resisting frame (MRF) buildings with different characteristics such as lateral, lateral-torsional, and torsional modes of vibration dominance as well as different stability conditions, which are considered in this paper. The MPA and CSM are compared with NTHAs in this paper. The results show

Note:

- This paper was received on January 21, 2024 and accepted for publication by the Editorial Board on July 25, 2024.
- Discussions on this paper will be accepted by March 31, 2025.
- <https://doi.org/10.18400/tjce.1422919>

1 Jahrom University, Department of Mechanical Engineering, Jahrom, Fars, Iran
mokarram@jahromu.ac.ir - <https://orcid.org/0000-0001-9820-6485>

2 Shiraz University, Department of Civil and Environmental Engineering, Shiraz, Fars, Iran
bananm@shirazu.ac.ir - <https://orcid.org/0000-0002-9763-8283>

3 Shiraz University, Department of Civil and Environmental Engineering, Shiraz, Fars, Iran
banan@shirazu.ac.ir - <https://orcid.org/0000-0002-7150-5343>

4 Shiraz University, Department of Civil and Environmental Engineering, Shiraz, Fars, Iran
abdkeyri@gmail.com - <https://orcid.org/0009-0004-9628-6986>

* Corresponding author

that the ASCE 41-23's coefficient method is unreliable for near-fault zones and that the MPA and CSM are unreliable for seismic evaluation of buildings with dominant lateral-torsional modes of vibration or significant P- Δ effects. The results also revealed that MPA is a conservative approach for seismic evaluation of torsionally dominant buildings while CSM is not.

Keywords: Nonlinear static procedure, modal pushover analysis, capacity spectrum method, performance-based seismic design, irregular buildings, near-fault earthquakes.

1. INTRODUCTION

Regarding the high computational costs of performing NTHA, especially for design purposes where the analysis-design cycle has to be recursively repeated until the designer reaches the desired design, NTHAs are not widely used by designers in the everyday design of buildings. There have been notable attempts (see [1,2]) to bring the NTHA-based design of buildings to a computationally affordable level, but the computational costs of these problems are still a challenge, even with today's modern computers. The computational cost is not the only challenge for engineers, as the expertise required for modelling and designing buildings based on NTHAs also discourages the designers from undertaking such an approach. Thus, in present-day circumstances, NSPs are, in fact, a valuable substitute for NTHA, and are being prescribed by many guidelines including [3-5] to enable designers to adopt the PBSO approach for evaluation and retrofitting of existing buildings as well as designing new ones. The literature contains serious critiques of the accuracy of such approaches and more research is therefore required to determine the applicability scope of NSPs. A brief overview of the problem is therefore given here.

The project initiated by the Federal Emergency Management Agency (FEMA) in 1984 to address the seismic risk of existing buildings marked the beginning of PBSO in building codes and standards. The project resulted in the FEMA 273 [6] report, which established quantitative acceptance criteria for four performance levels: Operational (OP), Immediate Occupancy (IO), Life Safety (LS), and Collapse Prevention (CP). FEMA 273 [6] introduced the fundamental concepts that were adopted by subsequent guidelines such as FEMA 356 [3] and FEMA 440 [4]. The NSP coefficients proposed in FEMA 356 [3] have been continuously revised and enhanced in later guidelines such as FEMA 440 [4]. This method also forms the basis of the codified coefficient method in recent seismic building standards such as ASCE/SEI 41-23 [5]. There are also many other NSPs, including adaptive and multi-mode approaches, available in the literature other than the aforementioned codified procedures. Some of them comprise the N2 method [7,8], the MPA [9,10], the upper-bound pushover analysis (UBPA) [11], the adaptive modal combination (AMC) procedure [12], the adaptive capacity spectrum method (ACSM) [13], the consecutive modal pushover (CMP) [14], the generalized pushover analysis (GPA) procedure [15], and the normalized multi-mode nonlinear static (NMP) procedure [16].

Kalkan and Kunnath [17] evaluated four NSPs, namely MPA, UBPA, AMC, and FEMA 356 NSP methods, for seismic evaluation of buildings using NTHAs with different ground motions, and found that the AMC procedure was the most consistent and accurate. Similarly, Bento et al. [18] assessed four NSPs, namely FEMA 440's CSM, N2, MPA, and ACSM procedures, for seismic assessment of plan-irregular reinforced concrete (RC) buildings using

a full-scale experimental frame and NTHAs, and found that the ACSM performed better than the others in predicting both global and local responses. By considering sixteen 2D frames, Pinho et al. [19] compared five NSPs, namely CSM, N2, MPA, AMC, and ACSM procedures, for seismic assessment of building frames with nonlinear dynamic analysis results, and found that MPA and ACSM performed slightly better than the others. However, Fragiadakis et al. [20] demonstrated that the accuracy of NSPs depends on the building characteristics, the level of inelastic demand and engineering demand parameters. Allahverdizadeh and Gholipour [21] argued that pushover methods have considerable flaws in identifying critical plastic regions. This problem becomes more severe at higher performance levels (i.e., higher nonlinearities). Moreover, Gonzalez-Drigo et al. [22] showed that using NSPs in damage state studies can lead to unconservative estimates. Marino et al. [23] investigated the near-collapse in-plane global response of unreinforced masonry buildings and showed that the European and Italian NSPs did not yield conservative results. Ruggieri and Uva [24] assessed the new NSP in the Italian building code by examining some low-rise RC buildings and inferred that it might produce more accurate results, but it also might yield non-conservative results in contrast to the conventional NSP, and therefore, it requires further validation with NTHA. Daei and Poursha [25] evaluated various NSPs, such as MPA, force-based adaptive pushover, displacement-based adaptive pushover, etc., for estimating the seismic demands of RC buildings and compared them with NTHA. They demonstrated that the accuracy of NSPs varies with the structure's height and the ground motion type. They also revealed that none of the NSPs had a significant advantage over the others and recommended further research and improvements of NSPs.

Some researchers have tried to adopt NSPs for approximating the structural capacity instead of using sophisticated incremental dynamic analysis (IDA). Ferraioli [26] investigated the dynamic increase factor (DIF) for NSP of RC frame buildings against progressive collapse due to sudden column loss. It was found that the DIF depended on the building properties, the location of the removed column, the catenary action of the floor slab, and the plastic dissipation capacity. Ke et al. [27] developed a multi-stage-based NSP based on the energy balance concept and a trilinear kinematic model to estimate the seismic demands of steel MRFs equipped with steel slit walls and compared its performance with NTHA responses. They concluded that the multi-stage-based NSP was able to produce satisfactory and conservative estimates of the peak seismic demands of the considered steel MRFs and that the seismic demand was significantly influenced by the multi-yielding stages of the system. Couto et al. [28] assessed old RC buildings in Lisbon using the N2 method and investigated how aging, smooth rebar, and corrosion affected seismic capacity and fragility. Wang et al. [29] proposed a deformation-based pushover analysis (DPA) method for evaluating the transverse seismic performance of tall inverted Y-shaped pylons in kilometer-span cable-stayed bridges. They applied the DPA to a case study of Sutong Bridge and compared it with other methods such as IDA, conventional NSP, and MPA. They concluded that DPA was efficient and convenient for the preliminary seismic design of inverted Y-shaped bridge pylons.

In addition to the individual application of NSPs and NTHAs, some studies have used them in combination to reduce the computational costs of the problem. For instance, Mokarram and Banan [2] proposed an effective adaptive surrogate multi-objective optimization model called surrogate FC-MOPSO in which optimal automated PBSO of buildings could be performed by simultaneous utilization of NSP and NTHAs such that the final designs were

based on NTHAs. They showed that up to 92% reduction in the required NTHAs could be achieved using their proposed model. Rossetto et al. [30] compared different methods for analyzing building responses under sequential earthquake and tsunami demands. They used a 10-storey RC structure as a case study. They found that a dynamic earthquake analysis followed by a variable depth pushover tsunami analysis was the best alternative to full dynamic analyses.

The frequency spectrum of seismic ground motions, which varies significantly between near-field and far-field events, influences the structural response of buildings. For instance, Bhandari et al. [31] assessed the seismic risk of a base-isolated building under near- and far-field earthquakes and found that the PGV:PGA ratio of near-field earthquakes affected the damage probability. Mokarram et al. [32] demonstrated that the maximum displacement ratio in ASCE/SEI 41-17's coefficient method can yield unconservative results for near-fault sites. Bilgin and Hysenlliu [33] have also shown that response of the masonry buildings under near-field and far-field earthquakes is remarkably different. Caution must be exercised when using NSPs in near-fault zones since they can yield unconservative solutions (see [34,35]).

About the criticisms pointed out in this section, it becomes evident that the NSPs, although widely used by practitioners for performing PBSDs, still have questionable reliability. Furthermore, a significant amount of research on the NSPs has been dedicated to evaluating the seismic vulnerability of regular buildings. Therefore, as confirmed by the review article by Asıkoğlu et al. [36], it is essential to examine their reliability regarding the impact of building irregularity on seismic behavior. This problem is even more magnified by noting that many failures have occurred due to asymmetry and irregularity in structures, during past earthquakes Das et al. [37]. Near-fault earthquakes also pose another concern as stated earlier. Thus, in this paper, ASCE/SEI 41-23's [5] coefficient method is evaluated first as the most practical code-based single-mode NSP for near- and far-fault earthquakes. Secondly, the accuracy of two alternative NSPs, namely FEMA 440's [4] CSM and MPA [9,10], for seismic assessments of symmetric and irregular steel MRF buildings with various characteristics is evaluated. As Najam [38] asserts, MPA method is the most well-known multi-mode NSP in the literature that incorporates the effects of higher modes contributions in system's response. Hassan and Reyes [39] also deduced that MPA is a strong candidate for approximating the inelastic seismic demands for the RC MRFs without dampers, instead of using the more complex NTHA.

2. NONLINEAR SYSTEMS MODELLING

The modified Ibarra-Krawinkler (IK) hysteresis model, proposed by Lignos and Krawinkler [40], in conjunction with the concentrated plastic hinge (CPH) model developed by Zareian and Medina [41], is utilized within the OpenSees [42] library for numerical simulation purposes of SDOF systems. The modified IK model [40], which is based on moment-rotation curves, aligns very well with FEMA documents and ASCE/SEI 41-23 [5] procedures for nonlinear analysis. This makes it highly adaptable for performing NTHA and NSP with a range of structural materials [40,43,44]. It effectively captures the response to cyclic loading, including strength and stiffness degradation in steel structures [40].

Rayleigh damping is commonly employed in dynamic analysis and is expressed by Eq. (1).

$$\mathbf{C} = a_0\mathbf{K} + a_1\mathbf{M} \tag{1}$$

where \mathbf{K} and \mathbf{M} denote initial stiffness and mass of the structure, respectively. a_0 and a_1 are stiffness-proportional and mass-proportional constants, respectively. However, initial stiffness-based Rayleigh damping can result in overestimated damping forces during NTHAs. More precise predictions of inelastic response can be obtained using tangent stiffness proportional damping [45,46], although this approach necessitates continuous updating of damping coefficients in the nonlinear problem. The CPH model, as proposed by Zareian and Medina [41], involves attaching nonlinear springs to the ends of the original six degrees of freedom (DOF) beam element. This creates an equivalent elastic beam element with end nonlinear rotational springs, resulting in eight DOFs. By assigning the stiffness-proportional damping coefficient to the linear beam element (Fig. 1), the model prevents excessively large damping forces that can occur due to system softening in the nonlinear phase. Zareian and Medina [41] demonstrated that this method yields results consistent with those obtained using tangent stiffness methods. When combined with the modified IK material model, the CPH model [41] suggests effectiveness for PBSO of steel MRFs [47]. In case ASCE/SEI 41-23 [5] moment-rotational behaviors are adopted for nonlinear springs, the P-M interactional effects in 2D models can be accounted for since the moment-rotational behaviors are a function of the axial force in the element.

In this study, a 5% damping ratio is applied to define the design spectrum. However, for the execution of NTHA in compliance with ASCE/SEI 41-23 [5], a 3% damping ratio is utilized to establish the Rayleigh damping coefficients.

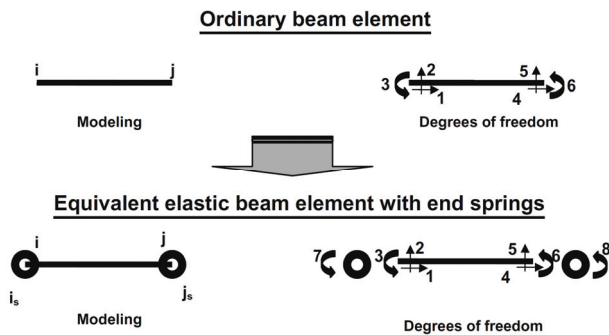


Fig. 1 - Representation of the ordinary nonlinear beam element and its equivalent model comprised of an elastic beam element with nonlinear springs at both ends [41].

3. EVALUATION OF ASCE/SEI 41-23'S [5] COEFFICIENT METHOD THROUGH SDOF SYSTEMS

The ASCE/SEI 41-23's [5] coefficient method is a single-mode NSP, which, as per ASCE/SEI 41-23 [5], is permitted to be used under two conditions: (1) the ratio of the elastic strength demand to yield strength (i.e., μ_{strength}) must be smaller than the maximum strength ratio (i.e., μ_{max}) of the system, and (2) the effects of higher modes must not be significant.

In this section, an investigation will be conducted to determine whether the method is reliable for near-fault sites. The reliability of ASCE/SEI 41-23's [5] coefficient method will be examined by considering 1250 SDOF systems. The coefficient method responses of the SDOF systems are then evaluated using ten near-fault and ten far-fault earthquake records which entails performing 25000 NTHAs.

ASCE/SEI 41-23's [5] coefficient method imposes lateral loads on the multi-degrees-of-freedom (MDOF) system that follow the vertical distribution of the fundamental mode shape of the structure in the direction of analysis. Then, a pushover analysis is performed to determine the force-displacement curve of the structure (i.e., base shear versus control node displacement). The force-displacement curve is used to generate an idealized force-displacement curve according to the procedure in ASCE/SEI 41-23 [5]. Finally, the target displacement, δ_t , of the control node, which represents the system displacement demand for a given hazard level, is computed from Eqs. (2) to (7).

$$\delta_t = C_0 C_1 C_2 S_a \frac{T_e^2}{4\pi^2} g \quad (2)$$

$$C_0 = \phi_{1,r} \frac{\sum_1^N m_i \phi_{i,n}}{\sum_1^N m_i \phi_{i,n}^2} \quad (3)$$

$$C_1 = 1 + \frac{\mu_{\text{strength}}}{a T_e^2} \quad (4)$$

$$C_2 = 1 + \frac{1}{800} \left(\frac{\mu_{\text{strength}} - 1}{T_e} \right)^2 \quad (5)$$

$$\mu_{\text{strength}} = \frac{S_a}{V_y/W} C_m \quad (6)$$

$$T_e = T_i \sqrt{K_i/K_e} \quad (7)$$

Here, C_0 is a modification factor that relates the spectral displacement of an equivalent SDOF system to the roof displacement of the building MDOF system and is equal to unity for an SDOF system. C_1 is the maximum displacement ratio coefficient, which is a modification factor that relates the expected maximum inelastic displacements to the displacements computed for linear elastic response. C_2 accounts for the effect of pinched hysteresis shape, cyclic stiffness degradation, and strength deterioration on the maximum displacement response. m_i , $\phi_{1,r}$, $\phi_{i,n}$ denote the mass at level i , the ordinate of the first mode shape at the roof (control node), and the ordinate of mode shape i at level n of the building, respectively. W , a , g , T_e , and C_m respectively represent, the effective seismic weight, the site class factor, the gravitational acceleration, the effective fundamental period of the building in the direction of interest, and the effective mass factor which is equal to unity for an SDOF system. T_i , K_i and K_e are the elastic fundamental period, elastic lateral stiffness, and effective lateral stiffness of the system, respectively. S_a is the spectral acceleration at the effective fundamental period and damping ratio of the building in the direction of interest.

According to Eq. (1), ASCE/SEI 41-23's [5] coefficient method depends on the design response spectrum of the chosen site. In this section, a site located in Northridge, California

(34°14'17.9"N, 118°31'59.8"W) with Class D soil is considered. The 5% damped design spectrum for this site, as specified in ASCE/SEI 41-23 [5], is employed for the BSE-2N hazard level in this study. Earthquake records for each SDOF system were scaled to align with the design spectrum, in accordance with ASCE 7-22's [48] amplitude scaling method. A period range from $0.2T_i$ to $1.5T_i$ was selected for this scaling process. Coefficient method evaluations are also derived from the same design spectrum. Newmark average acceleration method is adopted for conducting nonlinear time-history analyses. In addition, a Rayleigh damping ratio of 3% was applied for nonlinear time-history analyses, as per the ASCE/SEI 41-23 [5] provisions for NTHA.

To evaluate the reliability of the coefficient method, SDOF systems with various fundamental periods and force-displacement behaviors are considered. The mass of each SDOF system was adjusted to achieve a fundamental period of 0.1, 0.2, ..., or 2.5 sec. Additionally, 50 different values of effective yield strength, V_y , ranging from 155 kN to 4700 kN were used for the SDOF systems. Therefore, a total of 1250 SDOF systems were obtained. For each of these SDOF systems, a nonlinear material behavior should also be defined. Hence, a recursive analysis was performed to adjust the yield stress of the material such that the evenly distributed values of effective yield strengths could be obtained. Moreover, the recursive analysis included identifying matching W-sections. Specifically, a W-section was assigned to each yield stress such that if the W-section were used in a 3.66 m (12 ft) high cantilever column with a concentrated mass at its top, and the column were analyzed using the ASCE/SEI 41-23 [5] coefficient method, the system would yield the required fundamental period and effective yield strength corresponding to one of the 1250 SDOF systems. Once the W-section with its specific yield stress is identified, the nonlinear material behavior of the SDOF system, based on ASCE/SEI 41-23 [5], is also established. This is because, in the recursive analysis, the moment-rotation behavior of the W-sections is derived from ASCE/SEI 41-23 [5] and assigned to the nonlinear spring at the base of the column, as described in Section 2. For instance, it was found that if a W 12×120 section is assigned to an SDOF column with a concentrated 141.15 kg mass at the top and an elastic element, and the backbone curve of this section with $F_y = 186.16$ MPa is assigned to the nonlinear spring at the base, performing the ASCE/SEI 41-23 [5] coefficient method would result in $V_y = 154.93$ kN and $T_i = 0.101$ sec, which matches one of the considered SDOF systems (i.e., with $V_y = 154$ kN and $T_i = 0.1$ sec). Therefore, the backbone curves obtained from the ASCE/SEI 41-23 [5] tables for a W 12×120 section with $F_y = 186.16$ MPa in steel moment-resisting frames are used for this specific SDOF system.

The nonlinear time-history response of each system was evaluated according to the ASCE/SEI 41-23's [5] nonlinear dynamic procedure (NDP) under ten far-fault (Table 1) and ten near-fault (Table 2) ground motion records. Near-fault and far-fault records adopted in this study are those that have distances to the fault rupture (i.e., R_{rup} in Tables 1 and 2) that are less than and greater than ten kilometers, respectively. All records were recommended by FEMA 440 [4] for Class D soils. The average system responses under near-fault or far-fault ground motion records were used to assess the performance of the SDOF systems. Furthermore, for each fundamental period, the system responses were averaged over the responses of fifty SDOF systems with different shear yield strengths but the same fundamental period.

Table 1 - Far-fault ground motion records employed in this paper for evaluation of ASCE/SEI 41-23's [5] coefficient method using SDOFs.

Event Name	Year	Station	RSN ⁽¹⁾	Mechanism	Magnitude	R _{jb} ⁽²⁾ (km)	R _{rup} ⁽³⁾ (km)	I _s ⁽⁴⁾ (m/s)
San Fernando	1971	Cholame-Shandon Array #2	RSN60_SFERN_C02DWN	Reverse	6.6	217.5	218.1	184.8
San Fernando	1971	LA-Hollywood Stor FF	RSN68_SFERN_PEL090	Reverse	6.6	22.8	22.8	316.4
Morgan Hill	1984	Gilroy Array #2	RSN456_MORGAN_G02000	Strike Slip	6.2	13.7	13.7	270.8
Whittier Narrows-01	1987	Downey-Birchdale	RSN614_WHITTIER_A_A-BIR090	Reverse Oblique	6.0	14.9	20.8	245.1
Whittier Narrows-01	1987	LA-116th St School	RSN626_WHITTIER_A_A-116270	Reverse Oblique	6.0	18.2	23.3	301.0
Loma Prieta	1989	Gilroy-Historic Bldg.	RSN764_LOMAP_GOF160	Reverse Oblique	6.9	10.3	11.0	308.6
Landers	1992	North Palm Springs	RSN882_LANDERS_FHS000	Strike Slip	7.3	26.8	26.8	344.7
Landers	1992	Yermo Fire Station	RSN900_LANDERS_YER270	Strike Slip	7.3	23.6	23.6	353.6
Northridge-01	1994	Garden Grove-Santa Rita	RSN973_NORTHR_GAR000	Reverse	6.7	63.7	66.6	301.1
Northridge-01	1994	Los Angeles-7-story Univ Hospital (FF)	RSN1007_NORTHR_UNI005	Reverse	6.7	32.4	34.2	322.3

⁽¹⁾Record Sequence Number, which is a unique identifier for each ground motion record in the PEER ground motion database.

⁽²⁾The Joyner-Boore distance.

⁽³⁾Closest distance to the fault rupture.

⁽⁴⁾Average shear wave velocity over the top 30 meters of the subsurface.

Table 2 - Near-fault ground motion records employed in this paper for evaluation of ASCE/SEI 41-23's [5] coefficient method using SDOFs.

Event Name	Year	Station	RSN ⁽¹⁾	Mechanism	Magnitude	R _{jb} ⁽²⁾ (km)	R _{sup} ⁽³⁾ (km)	V _s ⁽⁴⁾ (m/s)
Loma Prieta	1989	Los Gatos-Lexington Dam	RSN3548_LOMAP_LEX000	Reverse Oblique	7.0	3.2	5.0	1070.3
Kobe	1995	Takatori	RSN1120_KOBE_TAK000	Strike Slip	6.9	1.5	1.5	256.0
Kobe	1995	Kobe University	RSN1108_KOBE_KBU090	Strike Slip	6.9	0.9	0.9	1043.0
Kobe	1995	Port Island (0 m)	RSN1114_KOBE_PRI000	Strike Slip	6.9	3.31	3.31	198.0
Erzican	1992	Erzican	RSN821_ERZINCAN_ERZ-EW	Strike Slip	6.7	0.0	4.38	352.1
Northridge-01	1994	Rinaldi Receiving Sta		Reverse	6.7	0.0	6.5	282.3
Northridge-01	1994	LA-Sepulveda VA Hospital	RSN1004_NORTH_SPV270	Reverse	6.7	0.0	8.44	380.1
Northridge-01	1994	Newhall-Fire Sta	RSN1044_NORTH_NWH090	Reverse	6.7	3.16	5.92	269.1
Imperial Valley-06	1979	El Centro-Meloland Geot. Array	RSN171_IMPVALL_H_H_EMO000	Strike Slip	6.5	0.07	0.07	264.6
Duzce	1999	Duzce	RSN1599_DUZCE_ATS030	Strike Slip	7.1	0.0	6.6	281.9

⁽¹⁾Record Sequence Number, which is a unique identifier for each ground motion record in the PEER ground motion database.

⁽²⁾The Joyner-Boore distance.

⁽³⁾Closest distance to the fault rupture.

⁽⁴⁾Average shear wave velocity over the top 30 meters of the subsurface.

Figs. 2(a) and (b) show the base shear demands obtained from the 1250 considered SDOF systems for far-fault and near-fault records, respectively.

Fig. 3 compares the relative errors of coefficient method estimations with NTHA responses. It reveals that the base shear demands from the coefficient method can be unreliable for near-fault sites, with errors up to 30%. For far-fault regions and structures with small fundamental periods (i.e., low-rise structures), the coefficient method provides conservative estimations of base shear demand of the system with errors that can reach 15%. Fig. 3 also suggests that the coefficient method can be a non-conservative method for medium to high-rise buildings in far-fault regions.

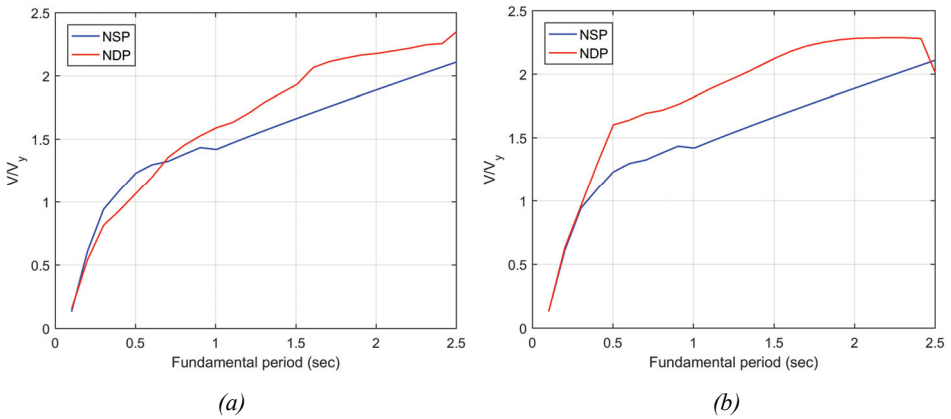


Fig. 2 - Normalized base shear demands from ASCE/SEI 41-23's [5] NSP (i.e., the coefficient method) and NDP for (a) far-fault, and (b) near-fault sites.

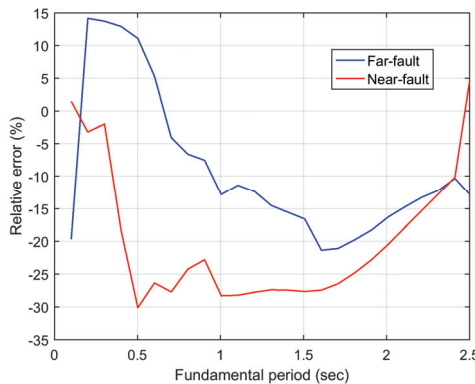


Fig. 3 - Relative error of ASCE/SEI 41-23's [5] coefficient method with respect to the NDP in predicting base shear demands for far-fault and near-fault sites

4. EVALUATION OF CSM AND MPA PROCEDURES FOR IRREGULAR BUILDINGS

In this section, it is examined whether FEMA 440's [4] CSM and MPA [9,10] procedures can be safely applied for seismic design and evaluation of irregular buildings. 96 3D buildings, of which 12 are symmetrical and the remaining 84 are unsymmetrical will be considered. The 84 unsymmetrical models are generated by modifying the first 12 symmetrical buildings to create 36 buildings with plan asymmetry and 48 buildings with different stability statuses.

4.1. Procedure

The 12 symmetrical buildings consist of 6 five-story and 6 ten-story buildings with either 5 m (Fig. 4(a)) or 10 m (Fig. 4(b)) bay spans. The buildings were designed to meet the requirements of ANSI/AISC 360-22 [49] and following the equivalent lateral force method and the load combinations of ASCE/SEI 7-22 [48] in three different categories: (1) ordinary steel MRFs, (2) special MRFs, and (3) designed for gravity loads only. The list of these 12 basic models is given in Table 3. It is noted the response modification factor (R -factor) for ordinary and special steel MRFs are equal to 3.5, and 8 as per ASCE/SEI 7-22 [48], respectively. Story heights in all models are equal to 3.6 m.

The dead load of the floors was taken equal to 4.1 kN/m^2 and an additional evenly distributed dead load of 1.5 kN/m^2 was applied to the floors to account for the loads of building partitions. The live load on building floors and the roofs were respectively taken equal to 2 kN/m^2 and 1.5 kN/m^2 . The density, modulus of elasticity, yield, and ultimate strength of steel material were assumed to be 7850 kg/m^3 , 200 GPa, 240 MPa, and 360 MPa, respectively. The configurations for the 12 basic building designs are given in Table A1 and Figs. A1, A2, A3, A4 and A5 of Appendix 1.

Force-based fiber elements in OpenSees [42], utilizing the Gauss-Lobatto integration method with five integration points, are employed in this section. For detailed discussions on the preference for force-based elements over displacement-based elements, refer to [50,51]. The Steel02 material in OpenSees [42] is used to model the uniaxial elasto-plastic behavior of the fibers. To ensure a more robust numerical analysis, a small strain hardening value of 1% was also incorporated. The 40-fiber discretization scheme, as discussed by Kostic and Filippou [52], was adopted. Kostic and Filippou [52] noted that even a 24-fiber scheme would achieve remarkable accuracy for I-shaped steel sections. In fiber element-based evaluation of the buildings the effects of rigid end zones are not accounted for.

The 36 buildings with asymmetrical plans were created by changing the mass distribution of 12 symmetrical buildings in three different ways. A part of the floor on the north-west panel was removed, and subsequently added some additional masses to points B2, B3, C2, and C3 of the plans of the basic buildings given in Fig. 4. This resulted in 36 buildings with three types of plan asymmetry, as explained below. Type 1 buildings have 9 times the removed mass added to each point B2, B3, C2 and C3. Type 2 buildings have 1.5 times the removed mass added to each point A1, A4, D1 and D4 and 2 times the removed mass added to each point where frames A, B, C, D intersect with frames 1 and 2. Type 3 buildings have 9 times the removed mass added to each point A1, A4, D1 and D4. The extra masses on the frames

were also adjusted so that the center of mass and the center of rigidity are 15% of the plan's dimension apart. Fig. 5 serves as an example, depicting the modification of model M1's plan. This alteration involves excising the shaded region from the plan and augmenting the mass at each of the four designated locations by a factor of nine, as shown in Fig. 5. To shift the building's center of mass by 2.7 meters (equivalent to 15% of the plan's dimensions) away from its center of rigidity, the masses placed on the frames along axes 2 and 3 are adjusted

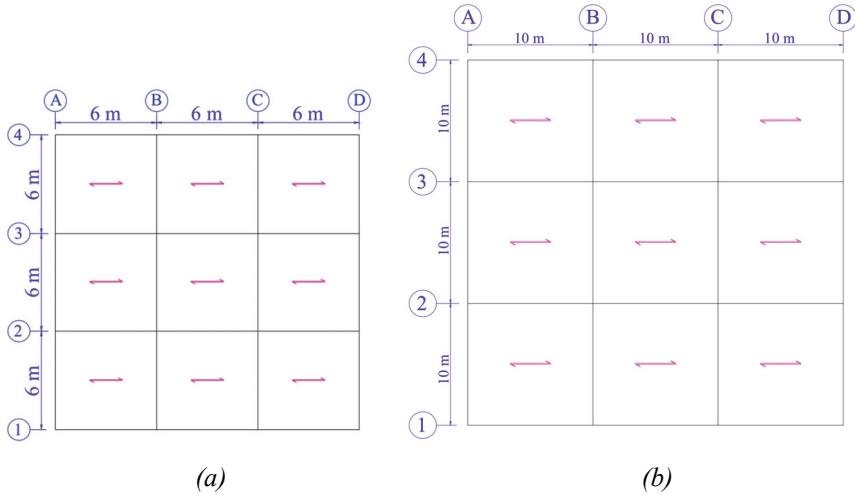


Fig. 4 - The two basic plans used for generating 96 symmetric and asymmetric five- and ten-story buildings with (a) 6 m bay spans, and (b) 10 m bay spans.

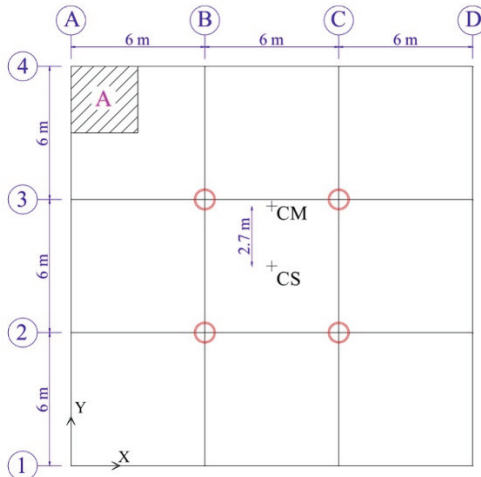


Fig. 5 - Model M1's plan modified to generate its corresponding Type 1 asymmetric building (i.e., model M13).

by factors of 0.1 and 1.9, respectively. Figs. 6 (a), (b), and (c) show the vibrational modes of three 5-story buildings with plan asymmetry, which were obtained by modifying model M1 of Table 3. The number of modes in these figures corresponds to the number of modes that achieved 90% mass participation. As an example, Table 4 lists the periods and effective mass participation factors for the initial modes of vibration in Type 1, Type 2, and Type 3 buildings (models M13, M25, and M36, respectively). It is ensured that the modes included in Table 4 provide at least 90% mass participation

Ultimately, buildings exhibiting different stability conditions were derived from eight of the basic symmetric buildings listed in Table 3 (i.e., models M1, M2, M4, M5, M7, M8, M10, and M11). To achieve this, the moments of inertia of the columns were changed in the north-south direction so that stability coefficients of 0.1 and 0.2 could be obtained. This was done for the first story, middle story, and top story of the 12 buildings. As a result, a suite of $8 \times 2 \times 3 = 48$ buildings with different stability coefficients, as listed in Table 5, were generated. The sections of the columns that were modified due to stability conditions are detailed in Table A2 within Appendix 1. The stability coefficient is obtained from Eq. (8) as per ASCE/SEI 7-22 [48].

$$\theta = \frac{P_x/h_{sx}}{V_x/\Delta_{xe}} \quad (8)$$

where P_x is the total vertical design load at and above level x , V_x/Δ_{xe} is the story stiffness at level x calculated as the ratio of the seismic design shear, V_x , divided by the corresponding elastic story drift, Δ_{xe} , and h_{sx} is the story height below level x . The selected value of $\theta = 0.1$ in this study is critical because the ASCE/SEI 7-22 [48] standard states that P- Δ effects on story shears and moments, the resulting member forces and moments, and the story drift induced by these effects can be ignored when the stability coefficient is equal to or less than 0.10. Furthermore, according to the ASCE/SEI 7-22 [48] standard, if $\theta > \theta_{max}$, the building is potentially unstable and must be redesigned. Since θ_{max} cannot exceed 0.25, $\theta = 0.2$ was chosen to represent buildings with high stability problems. The stability coefficient in Eq. (8), which represents the impact of gravitational forces on stability, is linked to the building's story stiffness, represented by the story stiffness ratio V_x/Δ_{xe} . By adjusting the columns' moments of inertia, this coefficient can be manipulated to highlight stability concerns at various building levels. Although this coefficient can be calculated for each story, this study demonstrates stability issues at the lower, middle, and upper stories of the building. Evidently, the stability issues included in the buildings of this section are explicitly accounted for in NTHA evaluations. Thus, NTHA analyses can be considered as the reference method to which FEMA 440's [4] CSM, MPA [9,10] methods can be compared.

Based on the discussions in Section 2, the 96 buildings described in this section were modelled using OpenSees [42]. Then, the seismic responses of the buildings were evaluated using FEMA 440's [4] CSM, MPA [9,10], and the rigorous NTHA method. The NTHA was performed for the buildings using 14 horizontal records, scaled to the considered design spectrum, from the first seven earthquakes in Table 1. It is noted that each earthquake in Table 1 represents two horizontal records for a 3D building. A brief description of FEMA 440's [4] CSM and MPA [9,10] procedures is given below.

Table 3 - List of the first 12 basic symmetric models.

Model No.	R-factor	Bays span (m)	Number of stories
M1	3.5		
M2	8.0	6	
M3	N/A*		5
M4	3.5		
M5	8.0	10	
M6	N/A*		
M7	3.5		
M8	8.0	6	
M9	N/A*		10
M10	3.5		
M11	8.0	10	
M12	N/A*		

*Not applicable because the model was designed for gravitational loads only.

Table 4 - Period and effective mass participation factors of three 5-story buildings with plan asymmetries of (a) Type 1 (model M13), (b) Type 2 (model M25), and (c) Type 3 (model M37).

Model	The mode of vibration	Period (sec)	Mass participation factor (%)	
			X-direction	Y-direction
M13	1	1.00	0.00	79.12
	2	0.95	73.23	0.00
	3	0.33	0.00	12.27
	4	0.32	0.75	0.00
	5	0.26	14.35	0.00
	Sum:			88.33
M25	1	1.07	39.15	0.00
	2	1.00	0.00	79.34
	3	0.78	35.48	0.00
	4	0.33	0.00	12.21
	5	0.31	6.05	0.00
	6	0.22	8.42	0.00
Sum:			89.10	91.55
M36	1	1.38	10.12	0.00
	2	1.00	0.00	79.40
	3	0.86	64.44	0.00
	4	0.40	1.53	0.00
	5	0.33	0.00	12.16
	6	0.24	12.14	0.00
Sum:			88.23	91.56

Table 5 - List of the 48 buildings with stability issues.

Model No.		R-factor	Bays span (m)	Number of stories	Location of stability issue
$\theta = 0.1$	$\theta = 0.2$				
M49	M73	3.5	6	5	First story
M50	M74	8.0			
M51	M75	3.5	10		
M52	M76	8.0			
M53	M77	3.5	6		
M54	M78	8.0			
M55	M79	3.5	10		
M56	M80	8.0			
M57	M81	3.5	6	5	Middle story
M58	M82	8.0			
M59	M83	3.5	10		
M60	M84	8.0			
M61	M85	3.5	6		
M62	M86	8.0			
M63	M87	3.5	10		
M64	M88	8.0			
M65	M89	3.5	6	5	Top story
M66	M90	8.0			
M67	M91	3.5	10		
M68	M92	8.0			
M69	M93	3.5	6		
M70	M94	8.0			
M71	M95	3.5	10		
M72	M96	8.0			

FEMA 440's [4] CSM is a way of estimating the maximum inelastic deformation of a nonlinear structure under earthquake ground motion. It involves converting the force-deformation relationship of the structure and the seismic demand into acceleration-displacement response spectrum (ADRS) format, which plots acceleration versus displacement as depicted in Fig. 7. The method then finds an equivalent linear system that has a larger period and damping than the original nonlinear system. The equivalent period and damping depend on the displacement, the post-yield stiffness, and the hysteretic behavior of the structure. The method uses an iterative process to find the intersection of the capacity curve and the reduced demand curve, which is called the performance point as depicted in Fig. 8. The method also imposes limits on the equivalent damping to account for strength and stiffness degradation. The method uses different parameters and formulas for different types of structures, such as reinforced concrete buildings.

The MPA [9,10] method is a way of estimating the seismic demands for a multistorey building. It involves computing the linear elastic modes and frequencies of the building and performing a nonlinear static analysis for each mode using a force distribution that depends on the mode shape. In this method, the pushover curve in the dominant direction of motion

is converted to an idealized force-deformation ($F_{sn}/L_n - D_n$) relation for the n^{th} mode for an equivalent SDOF system. The SDOF system is idealized as a bilinear curve with a post-yield stiffness that may be negative due to P- Δ effects. The peak deformation of the SDOF system is computed from a nonlinear response history analysis, an inelastic design spectrum, or an elastic design spectrum with empirical equations. The peak roof displacement associated with each mode is obtained by multiplying the peak deformation by the mode shape value at the roof. The peak responses due to gravity and lateral loads are extracted from the pushover database. The dynamic response due to each mode is calculated by subtracting the gravity response from the combined response. The total response is determined by combining the modal responses using the CQC rule.

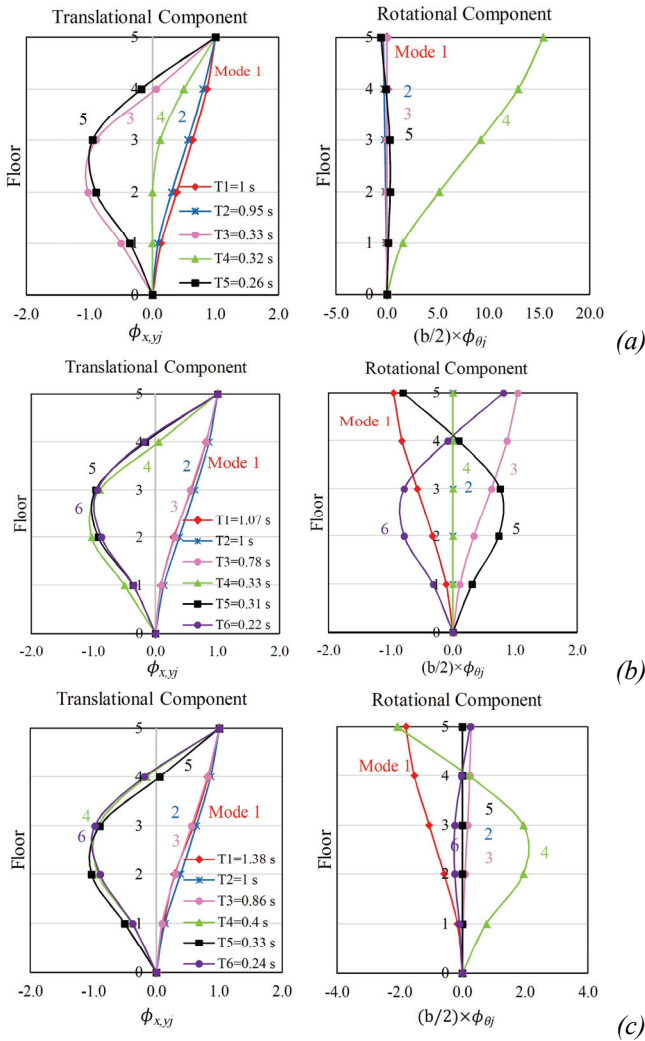


Fig. 6 - Vibrational modes of three 5-story buildings with plan asymmetries of (a) Type 1 (model M13), (b) Type 2 (model M25), and (c) Type 3 (model M37).

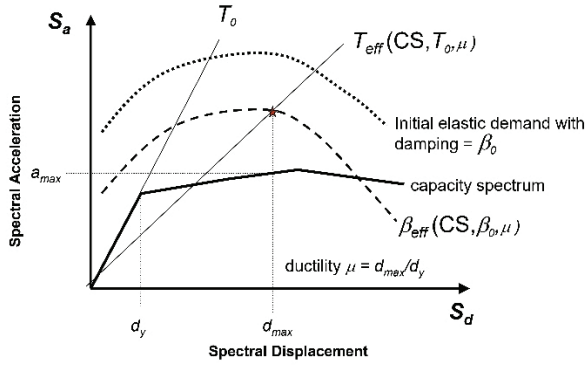


Fig. 7 - Schematic of ADRS showing effective period and damping parameters of equivalent linear system, along with a capacity curve [4].

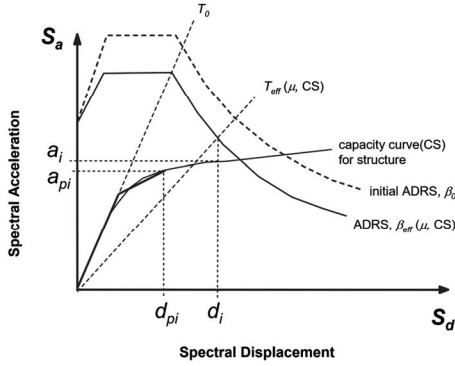


Fig. 8 - Determination of estimated maximum displacement using direct iteration [4].

4.2. Discussion of Results

The relative errors of inter-story drift ratios and base shears, evaluated using Eq. (9), obtained from CSM and MPA approaches for the 12 symmetric buildings with respect to the NTHA evaluations are given in Table 6.

$$e = \frac{R_{Approximation} - R_{NTHA}}{R_{NTHA}} \quad (9)$$

where e represents the relative error, R_{NTHA} denotes the target NTHA response of the system (such as drifts and base shears) averaged across seven earthquake records. $R_{Approximation}$ refers to the corresponding system response estimated using either the CSM or MPA methods. Consequently, negative errors indicate unconservative approximations, while positive errors suggest conservative approximations. Moreover, correlation values and medians of relative errors of the data obtained from analyzing the 96 considered buildings

are reported in Table 7. Since almost all errors are positive, it can be concluded that both methods can be regarded as conservative for symmetric buildings. The results of Table 6 along with the median errors and correlation values given in Table 7 suggest that both CSM and MPA give conservatively correlated approximations of the responses of symmetric buildings. It was also observed that CSM and MPA could overestimate base shears up to 42% and 21% for symmetric buildings, respectively. The overestimation for inter-story drifts could be up to 104% and 96% in worst cases, respectively.

Fig. 9 depicts the base shear relative errors of CSM and MPA procedures with respect to NTHA evaluations corresponding to the 36 asymmetric buildings. The three types of buildings (i.e., Type 1, 2, and 3) are also categorized in this figure. Type 1 buildings were intended to represent asymmetric buildings in which the lateral modes of vibrations are dominant while Type 2 and 3 were intended to represent asymmetric buildings in which lateral-torsional, and torsional modes of vibrations are dominant, respectively. Fig. 9 reveals that although CSM and MPA may yield errors up to 32% and 42% in base shear estimations, respectively, the results lie on the conservative side and are thus safe to use. A similar conclusion can also be drawn from Fig. 10 for inter-story drift responses. Moreover, Table 7 confirms that the base shear responses obtained from CSM and MPA procedures for the 36 asymmetric buildings are highly correlated with those obtained from the NTHAs and thus the results given in Fig. 9 are meaningful. Hence, it may be concluded that both CSM and MPA can be used for conservative seismic evaluation of asymmetric buildings in which lateral modes of vibration are dominant but, regarding the error fluctuations of Figs. 9 and 10 as well as medians of Table 5, it cannot be prescribed which one performs better. Finally, although both methods are conservative for Type 1 buildings, it must be noted that, according to Fig. 9, CSM and MPA might overestimate the base shear up to 31% and 42%, respectively. For inter-story drifts, according to Fig. 10, the overestimations can be up to 90% and 114%, respectively.

For Type 2 buildings, however, Fig. 9 reveals that the base shear responses of CSM and MPA in the X-direction of the buildings were on the unconservative side with relative errors up to -36% and -30% for these methods, respectively. Furthermore, Fig. 10 shows that MPA estimations for inter-story drift ratios were on the conservative side in most cases. According to Table 7, the median of relative errors corresponding to inter-story drifts obtained from MPA was equal to 22% and 39% for X- and Y-directions, respectively. CSM procedure, however, was totally unreliable and unconservative for estimating the inter-story drift-ratios of such buildings because Fig. 10 shows that the responses in one direction of the buildings (i.e., X-direction) were always between -50% and -66% with a median of relative errors, according to Table 7, equal to -59% for that direction. The correlation plot for the inter-story drift ratios of the CSM method in the X-direction is given in Fig. 13 (a), which evidently confirms this conclusion. Hence, it could be concluded that firstly, CSM was unconservative and thus unreliable for seismic demand evaluations of buildings in which lateral-torsional modes of vibrations are dominant, and secondly, due to the incorporation of higher modes effects, MPA gave conservative solutions for the evaluation of displacement demands of such buildings but it was still unreliable for estimating the global response (including both displacement and force demands) of Type 2 buildings.

Regarding Type 3 buildings, Fig. 9 reveals that base shear approximations obtained from CSM and MPA were conservative for most buildings with at most -23% relative error in

unconservative cases. The medians of relative errors in Table 7 also support this conclusion. Regarding inter-story drift ratios, however, Fig. 10 demonstrates that MPA gave conservative approximations while CSM totally underestimated inter-story drift ratios with unconservative errors ranging from -37% to -59%. This conclusion can also be confirmed by the median errors in Table 7 and the correlation plot given in Fig. 13 (a). Thus, it can be concluded that MPA can be regarded as a conservative tool for seismic evaluations of asymmetric buildings in which torsional modes of vibration are dominant while the CSM should be considered an unreliable method. However, it is added that, according to Figs. 9 and 10, MPA can overestimate base shear and inter-story drifts up to 20% and 112%, respectively.

Figs. 11 and 12 illustrate the relative errors of the base shear and inter-story drift ratios of the 48 buildings with different stability coefficients, respectively. The stability coefficients were considered as a code-based indicator of the effects of geometric nonlinearity (i.e., P-Δ effects) on the seismic response of buildings. By investigating Figs. 11 and 12 along with Table 7, which shows high correlations between the results of the approximation techniques and those from NTHA, it can be concluded that the stability issue has an inverse impact on the reliability of CSM and MPA procedures. In other words, in buildings where P-Δ effects are insignificant (i.e., $\theta \leq 1$), both CSM and MPA approximations are relatively reliable (with up to -40% errors on the unconservative side and the medians of the errors ranging from -1.3% to 29%), though it must be emphasized that, in this case, CSM can overestimate base shears and inter-story drifts up to 23% and 26%, while these values for MPA are 35% and 46%, respectively. For buildings where P-Δ effects are significant (i.e., $\theta > 1$), however, both CSM and MPA procedures are unreliable since they yield unconservative approximations with errors up to more than -50% and medians of the errors ranging from -17% to 8%. As an example, the correlation plot for the Y-direction inter-story drift ratios of the CSM approximations is given in Fig. 13(b), where it can be evidently observed that the method yields unconservative solutions for most of the cases.

Table 6 - Relative errors of CSM and MPA responses vs. NTHA evaluations for the 12 symmetric buildings in Y-dir.

Model No.	Average inter-story drifts relative error (%)		Base shear relative error (%)	
	CSM	MPA	CSM	MPA
M1	11.45	13.23	2.98	5.12
M2	16.34	19.34	0.45	8.65
M3	95.76	103.56	12.23	18.23
M4	13.94	21.76	4.53	5.97
M5	4.78	6.44	7.95	9.34
M6	66.65	89.52	17.45	43.21
M7	10.56	25.19	13.29	7.45
M8	32.09	51.36	17.25	10.56
M9	46.70	35.38	-3.98	7.75
M10	37.28	31.34	7.90	6.43
M11	34.68	60.23	13.87	11.87
M12	18.14	13.38	13.98	20.13

Table 7 - Data correlation and median relative errors of 97 building responses from CSM and MPA vs. NTHA in both directions.

Models	Approximation method	Buildings characteristics	Inter-story drifts ratios				Base shears			
			Median of relative error (%)		Correlation		Median of relative error (%)		Correlation	
			X-direction	Y-direction	X-direction	Y-direction	X-direction	Y-direction	X-direction	Y-direction
The 12 symmetric buildings (models M1–M12)	MPA	Symmetric	2.43	28.27	0.93	0.85	5.33	9.00	0.98	0.99
	CSM		11.32	25.12	0.91	0.81	4.43	10.09	0.97	0.99
The 36 buildings with asymmetric plans (models M13–M48)	MPA	Type 1	15.23	42.22	0.84	0.87	2.12	9.22	0.97	0.99
		Type 2	22.14	39.39	0.81	0.85	-5.34	9.41	0.97	0.99
		Type 3	18.08	29.35	0.93	0.84	2.98	8.30	0.97	0.99
	CSM	Type 1	34.24	20.19	0.75	0.84	9.95	13.50	0.95	0.99
		Type 2	-59.43	0.45	0.89	0.68	-15.46	16.11	0.97	0.99
		Type 3	-48.12	13.43	0.90	0.81	5.45	14.48	0.97	0.99
The 48 buildings with different stability conditions (models M48–M96)	MPA	$\theta = 0.1$	3.33	29.33	0.91	0.93	5.88	-1.27	0.98	0.96
		$\theta = 0.2$	2.67	3.67	0.91	0.97	6.66	-17.19	0.98	0.92
	CSM	$\theta = 0.1$	8.66	28.32	0.90	0.93	8.67	9.67	0.97	0.97
		$\theta = 0.2$	8.33	6.33	0.88	0.88	8.33	-14.66	0.96	0.93

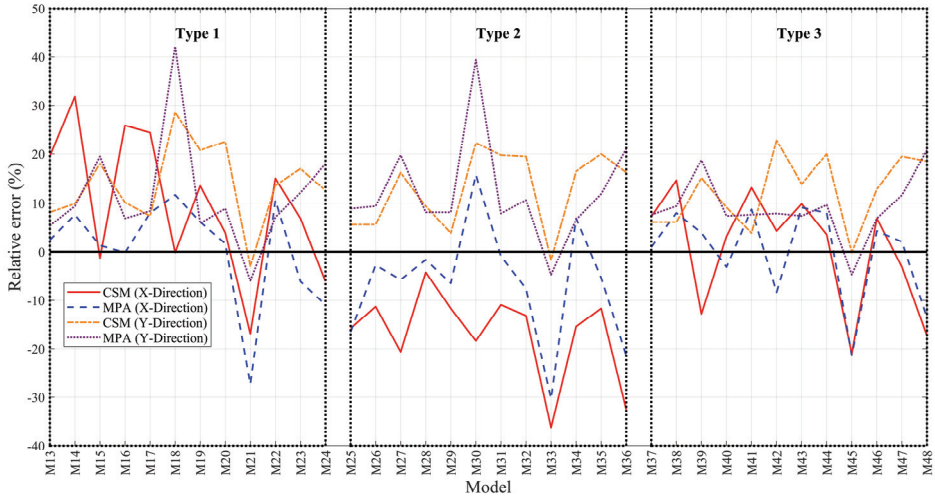


Fig. 9 - Base shear relative errors of CSM and MPA vs. NTHA for the 36 asymmetric buildings.

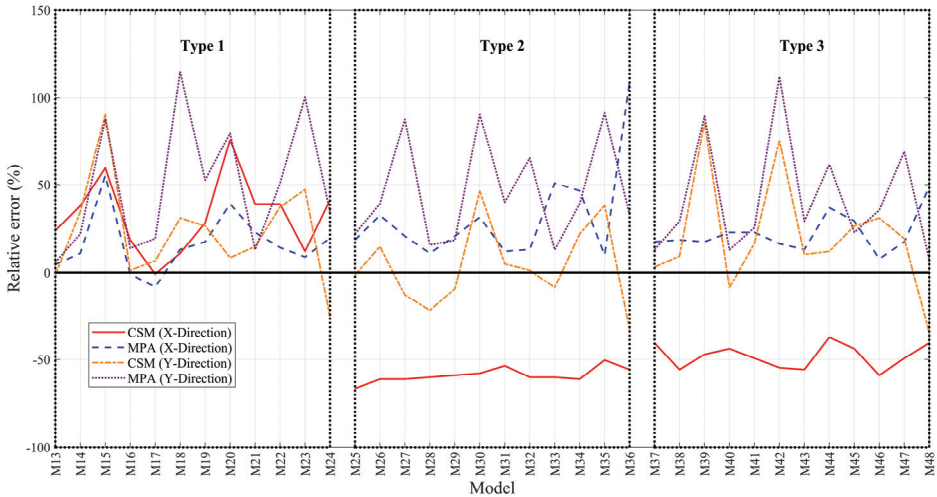


Fig. 10 - Inter-story drift relative errors of CSM and MPA vs. NTHA for the 36 asymmetric buildings.

The impact of stability issue location can be explored using Figs. 11 and 12. Significant P- Δ effects ($\theta > 1$) lead to a trend. This trend shows in both figures. As stability issues move to higher stories, errors in estimations grow. These errors lean towards unconservative results for both CSM and MPA methods. When P- Δ effects are minor ($\theta < 1$), the trend persists.

However, there's a distinction. The MPA method shows more unconservative errors than CSM. This is especially true when the stability issue is at the top story.

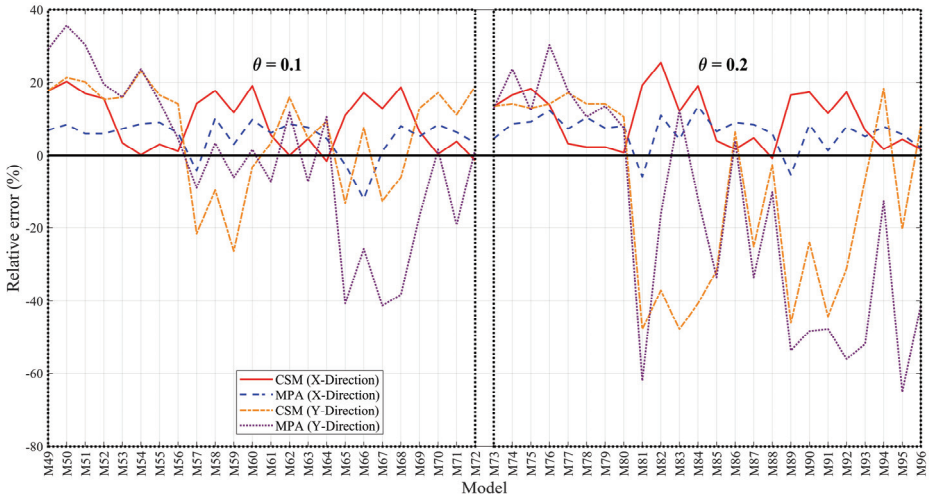


Fig. 11 - Base shear relative errors of CSM and MPA vs. NTHA for the 48 buildings with different stability conditions.

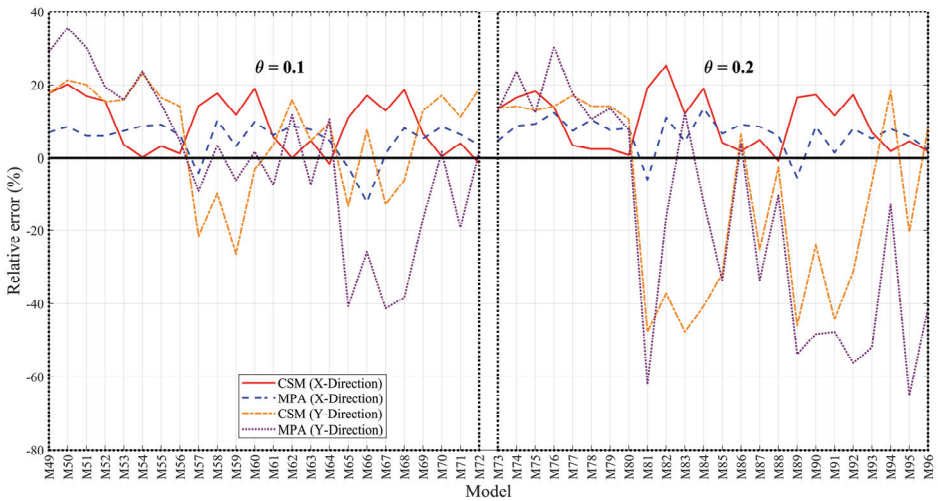


Fig. 12 - Inter-story drift ratio relative errors of CSM and MPA vs. NTHA for the 48 buildings with different stability conditions.

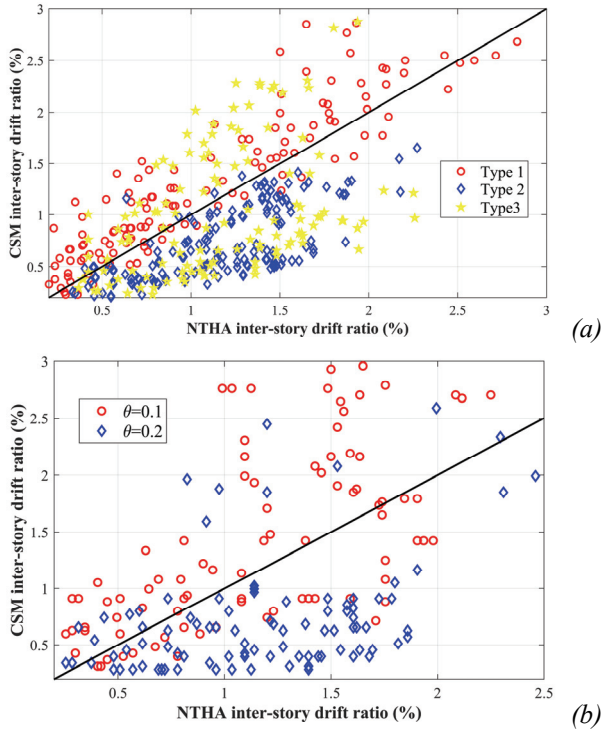


Fig. 13 - Correlation between CSM approximations and NTHA of inter-story drift ratios for (a) the X-dir responses of the 36 asymmetric buildings, and (b) the Y-dir responses of the 48 buildings with different stability conditions.

5. SUMMARY AND CONCLUSIONS

ASCE/SEI 41-23's [5] coefficient method is a viable codified tool for practitioners to perform the PBSD of buildings. It is true that, compared to linear procedures, the coefficient method can better describe the performance of a structure. However, it is not precise and it does not have the ability to capture the changes in dynamic response as the structure loses stiffness. Also, it cannot handle higher mode effects for multi degree of freedom systems. ASCE/SEI 41-23 [5] restricts the application of the method for two situations: (1) if the effects of higher modes are not negligible (e.g., in irregular buildings), and (2) if the building experiences severe stiffness degradation. In this paper, 1250 SDOF systems were considered to compare their responses from the coefficient method for near- and far-fault sites with the responses obtained from ASCE/SEI 41-23 [5] NDP procedure. It was shown that the method is unreliable for near-fault zones. The errors of base-shear evaluations can be non-conservative by up to 40%. Regarding far-fault zones, it was demonstrated that the method was conservative for systems with small fundamental periods and non-conservative for those with higher fundamental periods (i.e., mid- to high-rise buildings). Hence, it is concluded that further limitations on the applicability of ASCE/SEI 41-23's [5] coefficient method is needed.

Furthermore, for systems with significantly higher mode contributions, the applicability of two approaches, FEMA 440's [4] CSM and MPA [9,10], was investigated. 96 3D buildings were considered, including 12 symmetrical buildings, 36 irregular buildings and 48 buildings with different stability conditions (i.e., stability coefficients of 0.1 or 0.2). The 36 buildings consisted of three types of buildings in which lateral, lateral-torsional, or torsional modes of vibrations were dominant.

Comparing the responses of the 12 symmetric buildings analyzed using the CSM and MPA procedures to those analyzed with NTHAs, it was shown that the median of the errors ranged from 2% to 29%. Both methods were found to be conservative and reliable for the seismic evaluation of symmetric buildings.

The results demonstrated that both CSM and MPA could conservatively be used for approximating the response of irregular buildings in which the lateral modes of vibration were dominant. However, for irregular buildings in which the combination of lateral-torsional modes of vibration was dominant both methods underestimated the responses, resulting in non-conservative errors of up to -66% and -30%, respectively. It was also observed that MPA could yield relatively conservative solutions for the inter-story drift approximations but could not give satisfactory approximations of the base shear of such buildings. The MPA approach could conservatively predict the response of irregular buildings in which torsional modes of vibrations were more dominant but the CSM substantially underestimated the response with non-conservative errors ranging from -37% to -59%.

Finally, regarding the 48 buildings with different stability conditions, it was concluded that if the impact of P- Δ effects on system responses are negligible (i.e., $\theta \leq 1$), both CSM and MPA approximations are relatively conservative, but if the impact of P- Δ effects on system responses is significant (i.e., $\theta > 1$), both CSM and MPA procedures non-conservatively underestimate the building responses. The results also suggest that when the stability issue of the building is shifted to upper stories, response estimations obtained from both methods tend to lean toward the unconservative side.

It could be emphasized that although CSM and MPA can be conservatively adopted in some cases as discussed in preceding paragraphs, it was shown that the overestimation errors could be very large such that it undermines the applications of these methods from the economical viewpoint. Thus, it is recommended that at least the final design be cross-checked using NTHAs.

Symbols

a	Site class factor
a_0	Constant stiffness coefficient
a_1	Constant mass coefficient
C_0	Spectral displacement modification factor
C_1	Maximum displacement ratio coefficient
C_2	Hysteresis modification factor

C_m	Effective mass factor
F_u	Ultimate stress
F_y	Yield stress
g	Gravitational acceleration
h_{sx}	Story height below level x
\mathbf{K}	Initial stiffness matrix
K_e	Effective lateral stiffness
K_i	Elastic lateral stiffness
\mathbf{K}_t	Tangential stiffness matrix
\mathbf{M}	Mass matrix
m_i	Mass at the i^{th} story of the building
P_x	Vertical design load at and above level x
R_{jb}	Joyner-Boore distance
R_{rup}	Closest distance to the fault rupture
S_a	Spectral response acceleration
T_e	Effective fundamental period
T_i	Elastic fundamental period
V_s	Average shear wave velocity
V_x	Seismic design shear
W	Effective seismic weight
β	Damping ratio
δ_t	Target displacement
Δ_{xe}	Elastic story drift below level x
θ	Stability coefficient
μ	Ductility
μ_{strength}	Elastic strength demand to yield strength ratio
$\phi_{1,r}$	Ordinate of the first mode shape at the roof
$\phi_{i,n}$	Ordinate of mode shape i at level n of the building

References

- [1] V. Mokarram, A novel PSO-based multi-objective optimization methodology toward NTH analysis-based design of steel structures, PhD Dissertation, Shiraz University, 2018.
- [2] V. Mokarram, M.R. Banan, An improved multi-objective optimization approach for performance-based design of structures using nonlinear time-history analyses, Appl Soft Comput 73 (2018) 647–665. <https://doi.org/10.1016/J.ASOC.2018.08.048>.

- [3] FEMA 356, Prestandard and commentary for the seismic rehabilitation of buildings, Washington, D.C., 2000.
- [4] FEMA 440, Improvement of nonlinear static seismic analysis procedures, Washington, D.C., 2005.
- [5] ASCE/SEI 41-23, ASCE standard ASCE/SEI 41-23 Seismic evaluation and retrofit of existing buildings, American Society of Civil Engineers, Reston, Virginia, 2023.
- [6] FEMA 273, NEHRP guidelines for the seismic rehabilitation of buildings, Washington, D.C., 1997.
- [7] P. Fajfar, A nonlinear analysis method for performance-based seismic design, *Earthquake Spectra* 16 (2000) 573–592. <https://doi.org/10.1193/1.1586128>.
- [8] P. Fajfar, M. Fischinger, N2-A method for non-linear seismic analysis of regular buildings, in: *Proceedings of the Ninth World Conference in Earthquake Engineering*, 1988: pp. 111–116.
- [9] A.K. Chopra, R.K. Goel, A modal pushover analysis procedure to estimate seismic demands for unsymmetric-plan buildings, *Earthq Eng Struct Dyn* 33 (2004) 903–927. <https://doi.org/10.1002/EQE.380>.
- [10] A.K. Chopra, R.K. Goel, A modal pushover analysis procedure for estimating seismic demands for buildings, *Earthq Eng Struct Dyn* 31 (2002) 561–582. <https://doi.org/10.1002/EQE.144>.
- [11] T.S. Jan, M.W. Liu, C. Kao Ying Chieh, An upper-bound pushover analysis procedure for estimating the seismic demands of high-rise buildings, *Eng Struct* 26 (2004) 117–128. <https://doi.org/10.1016/J.ENGSTRUCT.2003.09.003>.
- [12] E. Kalkan, S.K. Kunnath, Adaptive modal combination procedure for nonlinear static analysis of building structures, *Journal of Structural Engineering* 132 (2006) 1721–1731. [https://doi.org/10.1061/\(ASCE\)0733-9445\(2006\)132:11\(1721\)](https://doi.org/10.1061/(ASCE)0733-9445(2006)132:11(1721)).
- [13] C. Casarotti, R. Pinho, An adaptive capacity spectrum method for assessment of bridges subjected to earthquake action, *Bulletin of Earthquake Engineering* 5 (2007) 377–390. <https://doi.org/10.1007/S10518-007-9031-8/METRICS>.
- [14] M. Poursha, F. Khoshnoudian, A.S. Moghadam, A consecutive modal pushover procedure for estimating the seismic demands of tall buildings, *Eng Struct* 31 (2009) 591–599. <https://doi.org/10.1016/J.ENGSTRUCT.2008.10.009>.
- [15] H. Sucuoğlu, M.S. Günay, Generalized force vectors for multi-mode pushover analysis, *Earthq Eng Struct Dyn* 40 (2011) 55–74. <https://doi.org/10.1002/EQE.1020>.
- [16] M. Zarrin, A. Daei, T. Heydari, A simplified normalized multi-mode nonlinear static procedure (NMP) for seismic performance evaluation of building structures, *Bulletin of Earthquake Engineering* 19 (2021) 5711–5741. <https://doi.org/10.1007/S10518-021-01185-Y/METRICS>.
- [17] E. Kalkan, S.K. Kunnath, Assessment of current nonlinear static procedures for seismic evaluation of buildings, *Eng Struct* 29 (2007) 305–316. <https://doi.org/10.1016/J.ENGSTRUCT.2006.04.012>.

- [18] R. Bento, C. Bhatt, R. Pinho, Using nonlinear static procedures for seismic assessment of the 3D irregular SPEAR building, *Earthquakes and Structures* 1 (2010) 177–195.
- [19] R. Pinho, M. Marques, R. Monteiro, C. Casarotti, R. Delgado, Evaluation of nonlinear static procedures in the assessment of building frames, *Earthquake Spectra* 29 (2013) 1459–1476. <https://doi.org/10.1193/100910EQS169M>.
- [20] M. Fragiadakis, D. Vamvatsikos, M. Aschheim, Application of nonlinear static procedures for the seismic assessment of regular RC moment frame buildings, *Earthquake Spectra* 30 (2014) 767–794. <https://doi.org/10.1193/111511EQS281M>.
- [21] R. Allahvirdizadeh, Y. Gholipour, Reliability evaluation of predicted structural performances using nonlinear static analysis, *Bulletin of Earthquake Engineering* 15 (2017) 2129–2148. <https://doi.org/10.1007/s10518-016-0062-x>.
- [22] R. Gonzalez-Drigo, J. Avila-Haro, L.G. Pujades, A.H. Barbat, Non-linear static procedures applied to high-rise residential URM buildings, *Bulletin of Earthquake Engineering* 15 (2017) 149–174. <https://doi.org/10.1007/s10518-016-9951-2>.
- [23] S. Marino, S. Cattari, S. Lagomarsino, Are the nonlinear static procedures feasible for the seismic assessment of irregular existing masonry buildings?, *Eng Struct* 200 (2019) 109700. <https://doi.org/10.1016/J.ENGSTRUCT.2019.109700>.
- [24] S. Ruggieri, G. Uva, Accounting for the spatial variability of seismic motion in the pushover analysis of regular and irregular RC buildings in the new Italian building code, *Buildings* 2020, Vol. 10, Page 177 10 (2020) 177. <https://doi.org/10.3390/BUILDINGS10100177>.
- [25] A. Daei, M. Poursha, On the accuracy of enhanced pushover procedures for seismic performance evaluation of code-conforming RC moment-resisting frame buildings subjected to pulse-like and non-pulse-like excitations, *Structures* 32 (2021) 929–945. <https://doi.org/10.1016/J.ISTRUC.2021.03.035>.
- [26] M. Ferraioli, Dynamic increase factor for nonlinear static analysis of RC frame buildings against progressive collapse, *International Journal of Civil Engineering* 17 (2019) 281–303. <https://doi.org/10.1007/s40999-017-0253-0>.
- [27] K. Ke, F. Wang, M.C.H. Yam, L. Deng, Y. He, A multi-stage-based nonlinear static procedure for estimating seismic demands of steel MRFs equipped with steel slit walls, *Eng Struct* 183 (2019) 1091–1108. <https://doi.org/10.1016/J.ENGSTRUCT.2019.01.029>.
- [28] R. Couto, M. V. Requena-García-Cruz, R. Bento, A. Morales-Esteban, Seismic capacity and vulnerability assessment considering ageing effects: case study—three local Portuguese RC buildings, *Bulletin of Earthquake Engineering* 19 (2021) 6591–6614. <https://doi.org/10.1007/s10518-020-00955-4>.
- [29] J. Wang, X. Wang, A. Ye, Z. Guan, Deformation-based pushover analysis method for transverse seismic assessment of inverted Y-shaped pylons in kilometer-span cable-stayed bridges: Formulation and application to a case study, *Soil Dynamics and Earthquake Engineering* 169 (2023) 107874. <https://doi.org/10.1016/J.SOILDYN.2023.107874>.

- [30] T. Rossetto, C. De la Barra, C. Petrone, J.C. De la Llera, J. Vásquez, M. Baiguera, Comparative assessment of nonlinear static and dynamic methods for analysing building response under sequential earthquake and tsunami, *Earthq Eng Struct Dyn* 48 (2019) 867–887. <https://doi.org/10.1002/EQE.3167>.
- [31] M. Bhandari, S.D. Bharti, M.K. Shrimali, T.K. Datta, Seismic fragility analysis of base-isolated building frames excited by near- and far-field earthquakes, *Journal of Performance of Constructed Facilities* 33 (2019) 04019029. [https://doi.org/10.1061/\(ASCE\)CF.1943-5509.0001298](https://doi.org/10.1061/(ASCE)CF.1943-5509.0001298).
- [32] V. Mokarram, M.R. Banan, M.R. Banan, Reliability of the maximum displacement ratio in nonlinear static procedure for near-fault sites, in: *International Conference on Civil Engineering, Architecture and Urban Management in Iran, Tehran, Iran, 2018*: pp. 1–6. <https://civilica.com/doc/846835/> (accessed August 25, 2023).
- [33] H. Bilgin, M. Hysenliu, Comparison of near and far-fault ground motion effects on low and mid-rise masonry buildings, *Journal of Building Engineering* 30 (2020) 101248. <https://doi.org/10.1016/J.JOBE.2020.101248>.
- [34] A. Mortezaei, H.R. Ronagh, A. Kheyroddin, G.G. Amiri, Effectiveness of modified pushover analysis procedure for the estimation of seismic demands of buildings subjected to near-fault earthquakes having forward directivity, *The Structural Design of Tall and Special Buildings* 20 (2011) 679–699. <https://doi.org/10.1002/TAL.553>.
- [35] A.V. Bergami, G. Fiorentino, D. Lavorato, B. Briseghella, C. Nuti, Application of the incremental modal pushover analysis to bridges subjected to near-fault ground motions, *Applied Sciences* 2020, Vol. 10, Page 6738 10 (2020) 6738. <https://doi.org/10.3390/APP10196738>.
- [36] A. Asıkoğlu, G. Vasconcelos, P.B. Lourenço, Overview on the nonlinear static procedures and performance-based approach on modern unreinforced masonry buildings with structural irregularity, *Buildings* 2021, Vol. 11, Page 147 11 (2021) 147. <https://doi.org/10.3390/BUILDINGS11040147>.
- [37] P.K. Das, S.C. Dutta, T.K. Datta, Seismic behavior of plan and vertically irregular structures: state of art and future challenges, *Nat Hazards Rev* 22 (2020) 04020062. [https://doi.org/10.1061/\(ASCE\)NH.1527-6996.0000440](https://doi.org/10.1061/(ASCE)NH.1527-6996.0000440).
- [38] F.A. Najam, Nonlinear static analysis procedures for seismic performance evaluation of existing buildings – evolution and issues, *Sustainable Civil Infrastructures* (2018) 180–198. https://doi.org/10.1007/978-3-319-61914-9_15/FIGURES/9.
- [39] W.M. Hassan, J.C. Reyes, Assessment of modal pushover analysis for mid-rise concrete buildings with and without viscous dampers, *Journal of Building Engineering* 29 (2020) 101103. <https://doi.org/10.1016/J.JOBE.2019.101103>.
- [40] D.G. Lignos, H. Krawinkler, Deterioration modeling of steel components in support of collapse prediction of steel moment frames under earthquake loading, *Journal of Structural Engineering* 137 (2011) 1291–1302. [https://doi.org/10.1061/\(ASCE\)ST.1943-541X.0000376](https://doi.org/10.1061/(ASCE)ST.1943-541X.0000376).

- [41] F. Zareian, R.A. Medina, A practical method for proper modeling of structural damping in inelastic plane structural systems, *Comput Struct* 88 (2010) 45–53. <https://doi.org/10.1016/j.compstruc.2009.08.001>.
- [42] S. Mazzoni, F. McKenna, M.H. Scott, G.L. Fenves, The open system for earthquake engineering simulation (OpenSees) user command-language manual, (2006).
- [43] D.G. Lignos, H. Krawinkler, A steel database for component deterioration of tubular hollow square steel columns under varying axial load for collapse assessment of steel structures under earthquakes, in: 7th International Conference on Urban Earthquake Engineering (7CUEE) & 5th International Conference on Earthquake Engineering (5ICEE) Conf. on Urban Earthquake Engineering (7CUEE), Tokyo: Center for Urban Earthquake Engineering, Tokyo Institute of Technology., 2010.
- [44] D.G. Lignos, H. Krawinkler, Sidesway collapse of deteriorating structural systems under seismic excitations, Report No. 177, The John A. Blume Earthquake Engineering Center, Stanford University, Stanford, CA, 2012.
- [45] J.F. Hall, Problems encountered from the use (or misuse) of Rayleigh damping, *Earthq Eng Struct Dyn* 35 (2006) 525–545. <https://doi.org/10.1002/eqe.541>.
- [46] L. Petrini, C. Maggi, M.J.N. Priestley, G.M. Calvi, Experimental verification of viscous damping modeling for inelastic time history analyzes, *Journal of Earthquake Engineering* 12 (2008) 125–145. <https://doi.org/10.1080/13632460801925822>.
- [47] V. Mokarram, M.R. Banan, Modeling considerations for performance based seismic design of steel moment resisting frames, in: International Conference on Civil Engineering, Architecture and Urban Management in Iran, Tehran, Iran, 2018: pp. 1–14. <https://civilica.com/doc/846834/>.
- [48] ASCE/SEI 7-22, ASCE standard ASCE/SEI 7-22 Minimum design loads for buildings and other structures, American Society of Civil Engineers, Reston, Virginia, 2022.
- [49] ANSI/AISC 360-22, ANSI/AISC 360-22 An American national standard specification for structural steel buildings, American Institute of Steel Construction, Chicago, Illinois, 2022.
- [50] A. Neuenhofer, F.C. Filippou, Evaluation of nonlinear frame finite-element models, *Journal of Structural Engineering* 123 (1997) 958–966. [https://doi.org/10.1061/\(ASCE\)0733-9445\(1997\)123:7\(958\)](https://doi.org/10.1061/(ASCE)0733-9445(1997)123:7(958)).
- [51] B.N. Alemdar, D.W. White, Displacement, flexibility, and mixed beam–column finite element formulations for distributed plasticity analysis, *Journal of Structural Engineering* 131 (2005) 1811–1819. [https://doi.org/10.1061/\(ASCE\)0733-9445\(2005\)131:12\(1811\)](https://doi.org/10.1061/(ASCE)0733-9445(2005)131:12(1811)).
- [52] S.M. Kostic, F.C. Filippou, Section discretization of fiber beam-column elements for cyclic inelastic response, *Journal of Structural Engineering* 138 (2012) 592–601. [https://doi.org/10.1061/\(ASCE\)ST.1943-541X.0000501](https://doi.org/10.1061/(ASCE)ST.1943-541X.0000501).

Appendix 1

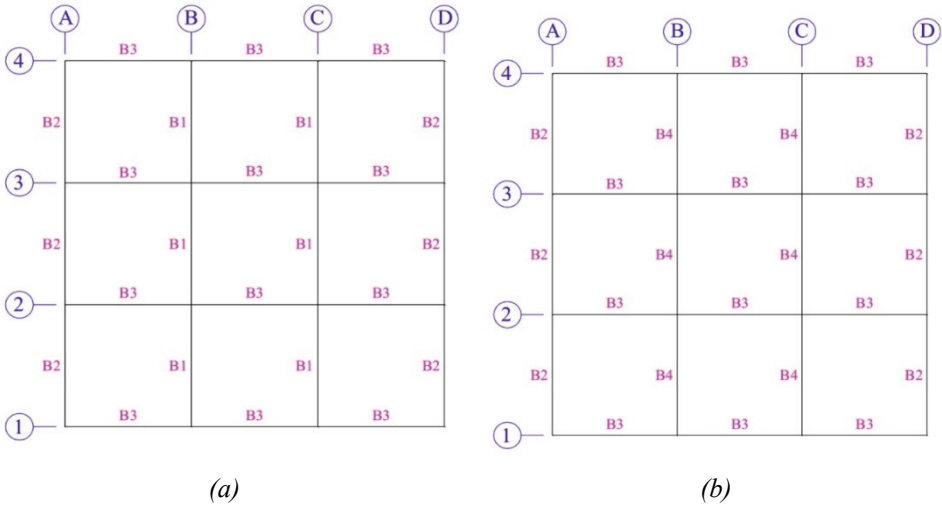


Fig. A1 - Grouping of the beams of the basic 5-story buildings: (a) 1st and 2nd stories, and (b) 3rd, 4th, and 5th stories.

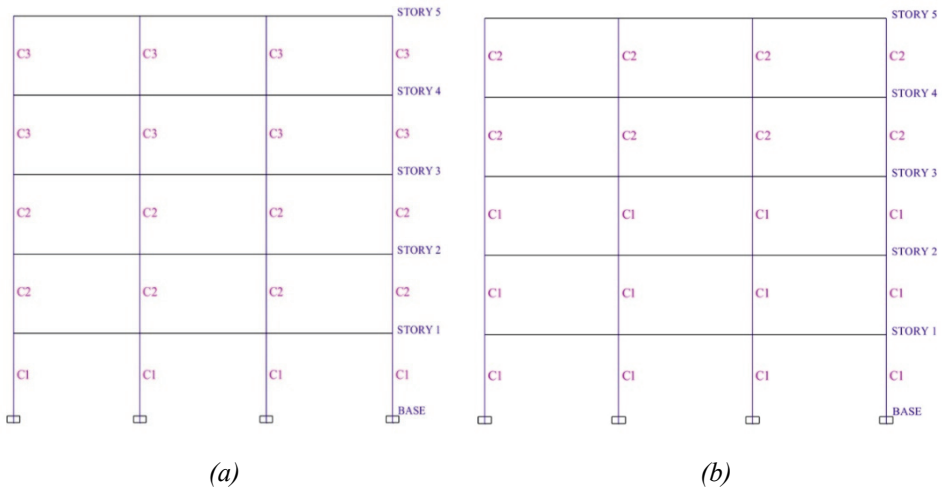


Fig. A2 - Grouping of the columns of the basic 5-story buildings: (a) axis 1, and 4, and (b) axis 2, and 3.

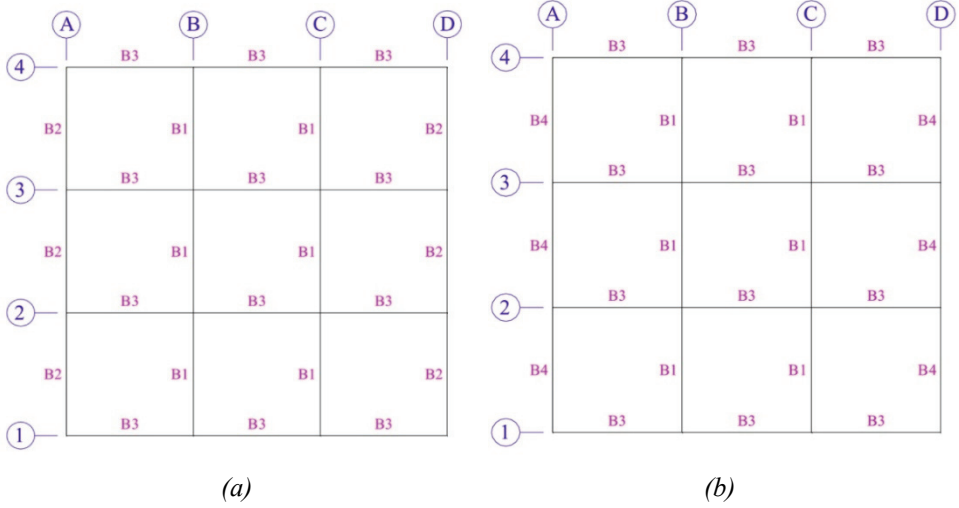


Fig. A3 - Grouping of the beams of the basic 10-story buildings: (a) 1st, 2nd, and 3rd stories, and (b) 4th, and 5th stories.

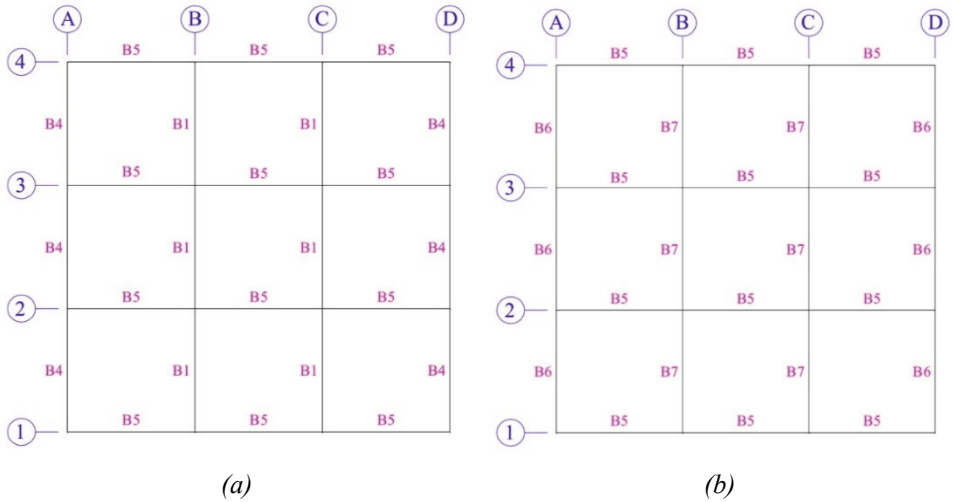


Fig. A4 - Grouping of the beams of the basic 10-story buildings: (a) 6th, and 7th stories, and (b) 8th, 9th, and 10th stories.

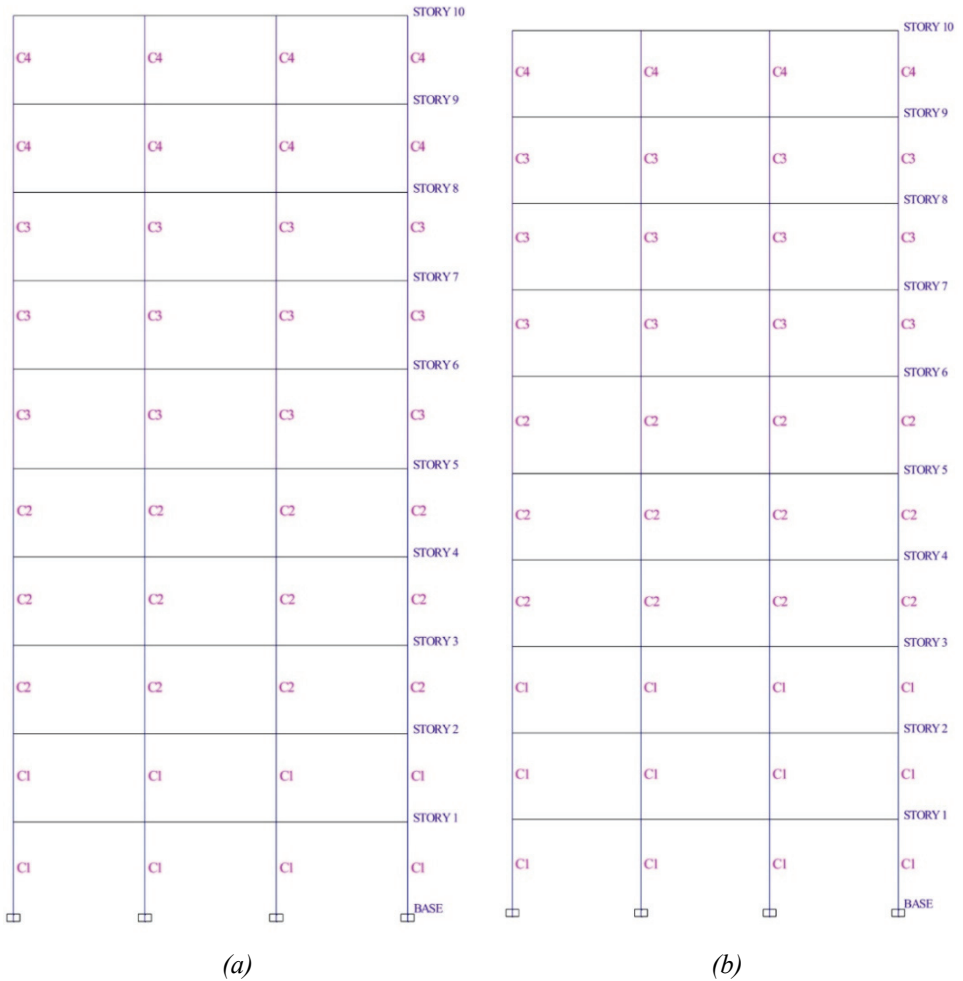


Fig. A5 - Grouping of the columns of the basic 10-story buildings: (a) axis 1, and 4, and (b) axis 2, and 3.

Table A1 - List of sections of the 12 basic buildings.

Model No.	C1	C2	C3	C4	B1	B2	B3	B4	B5	B6	B7
M1	70×55×2	55×45×2	45×35×2	N/A	45×25×2	40×20×1	40×20×1	45×25×1.5	N/A	N/A	N/A
M2	55×45×2	50×40×2	45×35×2	N/A	50×30×2	40×20×1	40×20×1	40×20×1	N/A	N/A	N/A
M3	50×35×2	45×35×2	40×30×2	N/A	35×20×1	30×15×1	30×15×1	35×20×1	N/A	N/A	N/A
M4	85×60×4	75×50×4	65×40×4	N/A	75×40×2	60×30×2	50×30×2	70×30×2	N/A	N/A	N/A
M5	70×50×4	60×45×4	55×35×3	N/A	60×35×2	60×35×2	30×30×2	60×35×2	N/A	N/A	N/A
M6	60×45×2	60×45×2	60×45×2	N/A	55×30×2	45×25×2	45×25×2	55×30×2	N/A	N/A	N/A
M7	60×45×4	50×40×4	45×35×3	40×30×2	55×30×2	50×20×2	50×20×2	45×25×2	40×20×2	45×25×1	40×20×2
M8	50×40×3	450×35×3	45×35×2	40×30×2	45×25×2	45×20×1	45×20×1	40×20×1	40×20×1	40×20×1	40×20×1
M9	45×35×2	40×30×2	30×20×2	30×20×2	40×20×1	30×15×1	30×15×1	30×15×1	30×15×1	30×15×1	40×20×1
M10	85×65×6	80×60×6	65×50×5	50×40×4	70×35×4	65×35×2	70×35×2	60×35×2	60×35×2	55×30×2	70×30×2
M11	70×55×5	65×55×5	60×50×5	50×40×4	70×35×2	60×35×2	65×30×2	50×30×2	50×20×2	50×30×2	50×30×2
M12	65×45×4	60×40×4	55×35×4	45×35×4	50×30×2	40×20×2	50×30×1	40×20×2	45×25×1	50×30×2	40×20×2

Note: All sections are I-shaped and are designated in the format: height × width × thickness (in centimeters). "N/A" stands for Not Applicable.

Table A2 - Sections of columns of the story with stability issue in each building.

Model No.	Sections of columns	Model No.	Sections of columns	Model No.	Sections of columns	Model No.	Sections of columns
M49	70×27×2	M61	50×26×4	M73	70×21×2	M85	50×20×4
M50	55×27×2	M62	45×31×3	M74	55×21×2	M86	45×24×3
M51	85×30×4	M63	80×35×6	M75	85×23×4	M87	80×28×6
M52	70×40×4	M64	65×42×5	M76	70×24×4	M88	65×29×5
M53	60×27×4	M65	45×18×2	M77	60×21×4	M89	45×14×2
M54	50×30×3	M66	45×18×2	M78	50×24×3	M90	45×14×2
M55	85×33×6	M67	65×20×4	M79	85×26×6	M91	65×15×4
M56	70×37×5	M68	55×22×3	M80	70×29×5	M92	55×18×3
M57	55×26×2	M69	40×19×2	M81	55×20×2	M93	40×15×2
M58	50×26×2	M70	40×18×2	M82	50×20×2	M94	40×15×2
M59	75×28×4	M71	50×21×4	M83	75×22×4	M95	50×21×2
M60	60×30×4	M72	50×22×4	M84	60×22×4	M96	50×21×2

Note: All columns in the story addressing the stability issue in each building possess identical cross-sectional dimensions, as specified in this table. All sections are I-shaped and are designated in the format: height × width × thickness (in centimeters).

Determination of Ungated Ogee Spillway Length so as to Pass Design Flood Safely

Tefaruk HAKTANIR¹



ABSTRACT

Because the flowrate over an ungated ogee spillway depends on the net head of the water conveyed in the approach channel and because the energy losses depend on the flowrate, computation of the spillway discharge for a given gross head of water in the reservoir entering the approach channel necessitates a trial-and-error procedure. For the given information of (a) the elevations of the lake water surface and of the spillway apex, (b) the energy loss coefficient at the entrance, the side wall inclination, the length, and the roughness coefficient of the trapezoidal approach channel, an iterative method for computing the discharge over an ungated ogee spillway is presented. Next, for the given information of (a) the (volume) ↔ (water surface elevation) relationship of the reservoir, (b) the spillway apex elevation, (c) the maximum allowed lake water surface elevation, and (d) the design flood hydrograph, an iterative method for computing simultaneously both the length of the ungated ogee spillway and the outflow hydrograph such that the maximum water surface elevation reached during routing of the design flood hydrograph becomes equal to the maximum allowed elevation is presented. Matching of the maximum water surface elevation reached in the reservoir while routing of the design flood hydrograph to the pre-specified maximum lake elevation requires a trial-and-error procedure of reservoir routing computations over many different-length spillways. The iterative method presented in this study which is executed in a single run of the coded computer program is a short-cut alternative to the long approach. The developed method is applied to Catalan Dam, which is one of the large dams in Türkiye from reservoir capacity, flood attenuation, and hydroelectricity production aspects, as a case study. The length of an ungated spillway is computed by the method presented here as an alternative to that of the existing radial-gated spillway. The reservoir routing computations done using the given design flood hydrograph produced fairly close maximum lake water surface elevations and the outflow hydrographs for ungated and gated spillways,

Keywords: Ogee profile ungated spillway, reservoir flood routing.

Note:

- This paper was received on January 28, 2024 and accepted for publication by the Editorial Board on July 24, 2024.
- Discussions on this paper will be accepted by March 31, 2025.
- <https://doi.org/10.18400/tjce.1427060>

¹ Erciyes University, Department of Civil Engineering, Kayseri, Türkiye
thaktan@erciyes.edu.tr - <https://orcid.org/0000-0002-8111-4557>

1. INTRODUCTION

The book *Design of Small Dams* [1] is a commonly used classical reference for design of dams; Yedigöze and Bayramhacılı Dams are just two of such cases [2, 3]. The method for computing the discharge passing over an ogee profile ungated (free flow) spillway for a given gross head over the spillway crest is described in detail with a couple of examples in that book. The spillway height is determined based on topographic conditions of the spillway site and on the experience of the designer. Conventionally, the design flood is the probable maximum flood for earth-fill dams. It may be a smaller magnitude flood like that having an average return period of 10,000 years [4]. The flood spillway will rout the design flood from the reservoir such that the maximum water surface elevation reached in the surcharge storage is below the dam crest elevation by a predetermined freeboard. The maximum water surface elevation in the lake is a critical value calculated by the economic cost incurred by inundation of the areas upstream of the dam. The dead storage is computed by the volume of sediment expected to settle behind the dam over a service life of about 100 years. The needed volume of the active storage above the dead storage is determined by a simulation operation model based on the projected yield from the dam, which can be as high as 90 % of the long-term average inflow, either in monthly or daily time steps over a critical dry period of 3 or 4 years.

There have been a few theoretical and experimental studies about the hydraulics of flow over free flow ogee spillways [e.g., 5, 6, 7, 8, 9, 10, 11, 12, 13]. Savage and Johnson [5] performed an experimental study with 10 different free flow conditions ranging from 7 % up to 120 % of the design head over an ogee-crested spillway model having a length of 1.83 m and a height of 0.80 m constructed with Plexiglas molded so as to conform to the exact shape of the designed ogee profile. And, they [5] concluded that there was reasonably good agreement among (1) the experimentally observed flowrates, (2) theoretically obtained flowrates from the FLOW-3D package program, and (3) the flowrates computed using the pertinent design charts from the book: *Design of Small Dams*. Chatilla and Tabbara [6] applied the ADINA-F software package which employs the free surface flow over an ogee spillway by $k-\epsilon$ turbulent flow model to a few experimentally observed flows created in a long flume with glass side walls in their hydraulics laboratory and reported good agreement between the experimental and computational flowrates and the surface profiles. Alhashimi [7] performed experiments on the laboratory model of the ungated ogee spillway of Mandali Dam in Iraq and compared the experimental results with the theoretical values given by the FLUENT software package which modeled the spillway flow by $k-\epsilon$ turbulent flow, and found that the computational and experimental values differed by 3.7 % and 7.4 %. Goharrizi and Moghadam [8] analyzed the data obtained from experiments with various different heads and flowrates on a spillway model made of Plexiglas in the hydraulics laboratory. They also computed the relevant flow parameters by the ANSYS CFX software package applying the $k-\epsilon$ turbulent flow model and they concluded that both the experimental and theoretical values were close to each other and also the relevant charts in *Design of Small Dams* yielded close values to the experimentally observed ones. Salmasi and Abraham [9] performed experiments on a 22 cm high ogee spillway model in a 10 m long and 25 cm wide glass channel in the Hydraulics Laboratory of Tabriz University with various configurations of flowrates and heads, and they found that the main spillway discharge coefficient was a function of P/H_e (where, P is the spillway height and H_e is the net head over the spillway crest) similar to the main chart for this coefficient in *Design of Small Dams*, and their experimentally determined magnitudes for the discharge coefficient were close to those in

the relevant chart in *Design of Small Dams*. Kocaer and Yerar [10] performed experiments in a laboratory on an ogee spillway model with various flowrates and heads and compared the magnitudes of the experimentally measured quantities with those given by two software packages of ANSYS-Fluent and OpenFOAM using two different turbulence models, namely, $k-\varepsilon$ and $k-\omega$, and concluded that these detailed finite-element models yielded close values to the experimentally observed ones. Fadafan and Kermani [11] applied the Moving Particle Semi-implicit (MPS) method, which is basically solution of partial differential equations of continuity and momentum with the help of some analytical arrangements, along with the software package FLOW-3D to the experimentally observed flows over a spillway model and they indicated that their MPS approach gave results close to both the experimental values and those given by FLOW-3D. Yildiz et al [12] performed experiments on a 7 cm high ogee spillway model in a laboratory flume of 7.5 cm width with various heads and flowrates, and they applied an adaptive neuro-fuzzy inference system (ANFIS) model along with the software package FLOW-3D to the flows over the spillway and they concluded that both the ANFIS and FLOW-3D models yielded values close to the experimentally observed ones. Yildiz et al [12] also concluded that the relevant charts in *Design of Small Dams* gave values close to the experimentally observed values. Kumcu et al [13] after having performed detailed experimental studies on the 1/50 scale ogee spillway model of Kavşak Dam on Seyhan River in Türkiye in the Hydraulics Model Laboratory of the Research and Quality Control Department of the General Directorate of State Water Works concluded that for the free flow case the experimentally determined stage \leftrightarrow discharge relationship covering all magnitudes of flowrates up to the maximum design discharge was very close to the theoretically computed relationship using the relevant charts in *Design of Small Dams*. Although spillways other than ogee-crested ones such as labyrinth weirs are designed and constructed for some dams as mentioned by Daneshfaraz et al [14], ogee spillways, still, are more frequently used.

Quite a few experimental and theoretical studies related to flow over ungated ogee spillway are summarized above. Some of those studies used one of the popular finite-element software packages simulating the spillway flow by thousands of meshes. Naturally, they are respectable but mostly academic studies. Usage of the mentioned software packages requires special training and most of design engineers do not know how to use them. And yet, some of those studies indicated that the relevant design charts in the book: *Design of Small Dams* gave close values to the experimentally observed flows. The objective of our study is computation of both the length of the ungated ogee spillway and the outflow hydrograph from that spillway simultaneously for given four peculiarities: (1) the incoming design flood hydrograph, (2) the spillway apex elevation, (3) the maximum allowed elevation of the surcharge storage, (4) the (valley volume) \leftrightarrow (water surface elevation) relationship of the reservoir. The developed method and the computer program executing it presents both the length of the designed spillway and the outflow hydrograph of the incoming design flood routed over the reservoir simultaneously such that the maximum water surface elevation reached equals the maximum allowed surcharge storage elevation. The difference between the approaches of the aforementioned studies and the work presented here is what makes it novel.

2. METHOD

2.1. Review of Discharge from Ungated Ogee Spillway by Design of Small Dams

Figure 9-23 in the *Spillways* chapter of *Design of Small Dams* presents the discharge coefficient, C_0 , versus the term P/H_0 , where P is the height of spillway and H_0 is the design head (including the velocity head) over the spillway apex elevation [1]. Figures 9-24, 9-25, and 9-27 give the charts for correction coefficients accounting for the effects of a water head different from the design head, inclination of the upstream face of the spillway, and the apron effect caused by the supercritical flow at the downstream toe of the spillway, respectively [1]. In *Design of Small Dams* and in some other relevant publications [1, 15], the equation below is given for the discharge passing over an ungated (free flow) ogee profile spillway.

$$Q = C_{\text{net}} \cdot L_e \cdot H_e^{1.5} \quad (1)$$

Here, Q is the spillway discharge in ft^3/s , C_{net} is the net discharge coefficient, H_e is the total head (including the velocity head) at the downstream end of the approach channel with respect to the spillway apex elevation in ft, and L_e is the effective spillway length in ft, which equals the net spillway length excluding the widths of the piers if any minus a correction value due to the contraction effect by the piers and the approach abutments. Equation (1) is not dimensionally homogeneous, and C_{net} has the units of $\text{ft}^{0.5} \cdot \text{s}^{-1}$. Therefore, when equation (1) is used in metric system, C_{net} of the foot-pound-second system must be divided by 1.811309 which is equal to $(3.28084)^{0.5}$.

Mostly there is a fairly long chute channel having a rather steep slope conveying the spilled discharge down to the energy dissipating structure. Rarely for some small dams, there is not a chute channel and the spilled flow discharges directly into a stilling basin. For such small structures usually a drowned hydraulic jump occurs at the downstream face of the spillway and a correction factor depicted by Figure 9-28 of *Design of Small Dams* is needed. As seen in this figure however, even for cases of small submergence the effect on discharge is negligible. Hence, for spillways having steep chute channels, the net discharge coefficient, C_{net} , of equation (1) is computed by

$$C_{\text{net}} = C_0 \cdot C_{H_e/H_0} \cdot C_{\text{incl}} \cdot C_{\text{aprn}} \quad (2)$$

Here, C_0 is the major discharge coefficient for ogee spillways having vertical upstream faces and it depends on the ratio of (height of the ogee spillway)/(design head), P/H_0 . The second coefficient, C_{H_e/H_0} , gives the correction factor for any head, H_e , other than the design head, H_0 . The third coefficient, C_{incl} , gives the correction factor for the inclination of the upstream face of the spillway. The fourth coefficient, C_{aprn} , gives the correction factor for the apron effect of the supercritical flow at downstream toe of the spillway, which is determined as a function of the ratio: (flow depth + velocity head at downstream end)/ H_e . The overall ranges of the three correction coefficients vary in the intervals of: $0.8 < C_{H_e/H_0} < 1.08$, $0.99 < C_{\text{incl}} < 1.04$, $0.77 < C_{\text{aprn}} < 1.00$ [1]. The major coefficient, C_0 , and the correction factor, C_{incl} , have fixed values for a particular spillway structure for any head, H_e . The other two correction factors, C_{H_e/H_0} and C_{aprn} , take on different magnitudes for every different head, H_e , and therefore, the net discharge coefficient, C_{net} , also assumes different magnitudes for different H_e 's.

2.2. Spillway Discharge under a Given Head

If the head loss due to entrance into the approach channel and the friction loss along the channel were neglected, then H_e in equation (1) would be: $H_e = (\text{lake water surface elevation at that instant}) - (\text{spillway apex elevation})$. Accurately however, H_e should be computed by

$$H_e = \text{WSE} - \text{SAE} - (h_{\text{entrance}} + h_{\text{friction}}) \quad (3)$$

Here, WSE is the lake water surface elevation at that moment, SAE is the spillway apex elevation, h_{entrance} is the head loss incurred during entrance into the approach channel, and h_{friction} is the total friction loss from the beginning to the end of the approach channel. h_{entrance} is computed as a fraction of the velocity head in the channel by

$$h_{\text{entrance}} = C_{\text{entr}} \cdot [Q^2 / (A_{\text{approch}}^2 \cdot 2g)] \quad (4)$$

where, C_{entr} is the entrance loss coefficient, recommended range is between 0.1 and 0.3 [1], A_{approch} is the cross-sectional area of the approach channel while conveying the spilled discharge Q , and g is the acceleration of gravity. h_{friction} is computed with the help of the Manning equation by

$$h_{\text{friction}} = L_{\text{approch}} \cdot (Q \cdot n \cdot P_{\text{approch}}^{2/3} / A_{\text{approch}}^{5/3})^2 \quad (5)$$

Here, L_{approch} is the length of the approach channel, P_{approch} and A_{approch} are the wetted perimeter and the flow area in the channel, and n is the Manning roughness coefficient of the channel. Equation (5) in this form is valid in metric system of units, and n should be replaced by $(1.49) \cdot n$ if it is to be used in foot-pound-second system.

If the approach channel is not short and if its abutments have dull shapes, the head losses, h_{entrance} and h_{friction} , will assume non-negligible magnitudes. Usually, their sum is of the order of a couple of decimeters at most. In the realistic case of accounting for the approach channel head losses, because Q depends on H_e by equation (1), while H_e is related to Q according to equations (3), (4), and (5), computation of the spillway discharge at any lake water surface elevation necessitates a trial-and-error procedure. The iterative numerical algorithm as a practical alternative put forth in this study is summarized in the following.

- (i) Assume $(h_{\text{entrance}} + h_{\text{friction}}) = 0$ and compute an initial estimate for H_e denoting it by $H_{e,1}$.
- (ii) Inserting $H_{e,1}$ for H_e , compute an initial estimate for the spillway discharge, Q , by equations (3), (2), and (1), executing them in this order.
- (iii) With Q computed at previous step, compute h_{entrance} and h_{friction} by equations (4) and (5).
- (iv) Inserting the magnitudes of h_{entrance} and h_{friction} in equation (3) compute the improved magnitude for $H_{e,i}$ denoting it by $H_{e,i+1}$.
- (v) Compute the absolute relative difference between $H_{e,i+1}$ and $H_{e,i}$ by:

$$\text{ARD} = \left| (H_{e,i+1} - H_{e,i}) / H_{e,i+1} \right| .$$

- (vi) If $\text{ARD} \leq 1 \cdot 10^{-6}$, then $H_{e,i+1} = H_{e,i}$ and the spillway discharge at that lake water surface elevation equals the magnitude of Q computed at step (ii), and the iterations stop here.

(vii) If $RD > 1 \cdot 10^{-6}$, then set $i = i+1$, $H_{e,i} = H_{e,i+1}$ (assign the improved head at the last iteration as the new estimate of the next iteration) and go to step (ii) above and repeat the iterations.

This algorithm converges in two or three iterations and Q under that WSE is hence computed.

2.3. Spillway Length for Given Design Flood Hydrograph and Spillway Design Head

Determination of the length of the free flow spillway such that when the design inflow hydrograph is routed over the reservoir, the maximum water surface elevation reached in the reservoir be close to a pre-specified maximum allowed elevation requires a trial-and-error approach involving a few reservoir routing computations with many different-length spillways [e.g., 1, 15]. In this study, we propose a numerical approach which eliminates this long method of trials. Our method simultaneously determines (a) the length of that free flow spillway such that the maximum water surface elevation reached in the reservoir is equal to the pre-specified maximum allowed elevation and (b) the outflow hydrograph resulting from routing of the incoming design flood hydrograph. In the following, the method devised in this study is explained.

The dead storage and the active storage capacity of the reservoir of a dam are computed by the known methods. The apex elevation of the ungated flood spillway equals the elevation of the top of full active storage. The maximum allowed water surface elevation to occur during passage of the design flood from the reservoir is determined beforehand independently from reservoir routing computations based on comprehensive economic analyses to maximize the financial difference of benefits on account of water releases from the active storage and costs due to the inundated upstream areas. And, the spillway design head, H_0 , is computed by

$$H_0 = MWSE - SAE \quad (6)$$

Here, MWSE is the maximum allowed lake water surface elevation, SAE is the spillway apex elevation. Next, the length of the spillway whose design head is H_0 is computed by an iterative procedure. The initial estimate of the spillway length is made by equation (1) assuming the maximum discharge of the outflow hydrograph, which is the same as the maximum spillway discharge, equals 70 % of the peak of the incoming design flood hydrograph. The spillway length which makes the spillway discharge equal to the peak of the outflow hydrograph under the design head of H_0 is computed by a recursive algorithm. At the last one of the iterations, the outflow hydrograph is also determined along with the correct spillway length.

The shape of the downstream face of an ogee spillway with a design head of H_0 closely resembles the lower surface of the nappe of the freely shooting flow over a sharp-crested weir [1, 15]. Hence, the water flowing over the ogee profile spillway is not carried by its downstream part and the efficiency of spillage becomes almost as high as that of the free flow over the sharp-edge spillway of the same height. If it were not a free jet but rather an open channel flow carried by the downstream part of the spillway, the discharge in that case would be smaller than the free jet due to wall friction losses. Because it is almost a freely shooting nappe the hydrostatic pressure of the spilled water on the bottom of the downstream face of the spillway is close to zero. For a flowrate smaller than the design discharge, the nappe profile of the spilling water is shorter than that of the design discharge, and the

downstream face of the spillway begins acting like a channel causing a reduction in the discharge coefficient C_0 hence in C_{net} . In this case, the pressure on the downstream face is positive, and the spilling water does not have a tendency to separate from the crest curve, which is an advantage actually along with the disadvantage of reduction in C_{net} . According to Figure 9-24 of *Design of Small Dams*, the highest drop in C_{net} is $C_{He/H_0} = 0.80$. In other words, alleviation of the possibility of cavitation damage versus a reduction in discharge efficiency of at most 20 % actually is an advantage rather than a disadvantage. Again, according to the same figure, for heads greater than the design head ($H_e > H_0$) the discharge efficiency increases as much as 8 %. This is because the spilling jet shoots farther away under a head greater than the design head and the suction induced by the negative pressure incites a higher flow. This slight increase in discharge efficiency may seem to be advantageous; but, along with it cavitation damage to the concrete material of the spillway may take place. Therefore, in this study, the maximum discharge over the spillway is not allowed to exceed the design discharge, and the head forming at the maximum spillway discharge during routing of the design flood hydrograph is taken equal to the spillway design head, H_0 .

The volume of the valley upstream from the dam between the maximum allowed water surface elevation and the top of full active pool is known as the surcharge storage. The ratio of the surcharge storage to the total volume of the design flood hydrograph is directly effective on abating the peak of the outflow hydrograph. The surcharge storage for dams whose service objectives do not include flood damage reduction is usually small, and the peak of the outflow hydrograph becomes close to the peak of the inflow hydrograph of the design flood. In this study, the peak of the outflow hydrograph is made equal to the discharge of the spillway occurring under the design head, and this condition is satisfied by an iterative method, which is summarized in the following step by step.

(1) At the arrival of the design flood to the reservoir, the lake water surface elevation equals the spillway apex elevation ($WSE = SAE$). First, the incremental time step, Δt , is chosen. For dams having large reservoirs, Δt may be taken as 1 hour, and small or large for any dams, it could be chosen as small as 0.2 hr or even 0.1 hr. The ordinates of the design flood hydrograph at Δt time steps throughout its time base should be computed and stored in a file beforehand. And, the length ($L_{approch}$) and the Manning roughness coefficient (n) of the approach channel are determined considering the area upstream from the spillway and the channel material.

(2) The spillway design head, H_0 , is determined by equation (6).

(3) The spillway height with respect to the bottom of the approach channel can be taken as

$$P \approx (0.5) \cdot H_0 \quad (7)$$

This yields a reasonable value for P (spillway height) because, as seen in Figure 9-23 of *Design of Small Dams*, the major spillway discharge coefficient, C_0 , rapidly drops down to very low values for spillways whose heights are smaller than half of the design head. Yet, equation (7) is not a strict rule, and another value for P dictated by the topography of the area where the spillway is situated may be taken.

(4) The angle of inclination of the upstream face of the spillway is determined. Recently, an inclination of $45^\circ \sim 33^\circ$ with the vertical is commonplace [e.g. 2, 3].

(5) The elevation difference between the upstream and downstream toes of the spillway is determined, basically by topographic factors. This value is usually of the order of 1 m ~ 3 m.

(6) The initial estimate for the peak of the outflow hydrograph, Q_{poutf} , is made as:

$$Q_{poutf} = (0.7) \cdot Q_{pinf} \quad (8)$$

Here, Q_{pinf} is the peak of the design flood hydrograph. And, the initial estimate of the design spillway discharge, Q_{design} , is made as:

$$Q_{design} = Q_{poutf} \cdot 1 \quad (9)$$

(7) Assigning $H_e = H_0$, the coefficients: C_0 , C_{incl} , and C_{aprn} are taken from Figures 9-23, 9-25, and 9-27 of *Design of Small Dams* [1], and C_{net} is computed by equation (2).

(8) The effective spillway length is computed by equation (10) below, which is another form of equation (1)

$$L_e = Q_{design} / (C_{net} \cdot H_0^{1.5}) \quad (10)$$

(9) The net spillway length, L , is computed by adding the contraction effects of the piers and of the approach abutments to L_e .

(10) The width of the approach channel is equal to the gross spillway length ($b = L$).

(11) In routing computations, the spilled discharge at the end of each Δt time step is computed by an iterative numerical method. The algorithm used here and in some other studies [e.g. 16] is briefly summarized in the following. The initial estimate for the spillway discharge at the end of any Δt time step is made by extrapolation using the second-degree polynomial passing through discharges at the ends of the three preceding Δt 's. Beginning with this initial estimate, by two or three iterations, the lake water surface elevation and the spillway discharge at the end of that Δt is computed to six significant digits. At each iteration, the discharge passing over the ogee spillway is computed by the recursive method summarized in subsection: 2.2. Spillway Discharge under a Given Head.

(12) When the routing computations at Δt time steps all over the time base of the design flood hydrograph are completed, the peak of the outflow hydrograph, Q_{poutf} , is determined by finding its maximum ordinate. If the absolute relative difference between Q_{poutf} and the previous design spillway discharge, Q_{design} , is not smaller than $1 \cdot 10^{-6}$, then the new spillway design discharge is taken as $Q_{design} = Q_{poutf}$, the computations are sent back to the 8th step above, and the iterations between the 8th and 12th steps are repeated until convergence to six significant digits is achieved. Ultimately, the length of the ogee spillway computed at the 9th step is the searched length of the spillway such that (a) its design discharge is equal to the peak of the outflow hydrograph routed by it, (b) the maximum lake water surface elevation is equal to the pre-specified value, MWSE, and (c) the outflow hydrograph computed at the 11th step of the last iteration is the final outflow hydrograph. A computer program is coded performing this iterative procedure. The program can be rerun with a spillway height different from the one at the 3rd step.

3. AN EXAMPLE: SPILLWAYS OF CATALAN DAM ON SEYHAN RIVER

3.1. Length of Ungated Spillway

Catalan Dam exists on a cross-section of Seyhan River in the Mediterranean Region of Anatolia. This dam serves for both energy production and flood abatement. The capacities of its active storage and surcharge storage are 990 hm³ and 590 hm³. Its flood spillway is a radial-gated ogee spillway having a net length of 66 meters with six gates [17]. The data of Catalan Dam about (a) its flood spillway, (b) the probable maximum flood (PMF), which has a peak flowrate of 10,055 m³/s, (c) the maximum allowed water surface elevation of the surcharge storage, which is 126.5 m, (d) the top elevation of the full active storage, which is 118.6 m, and (e) the (reservoir volume, hm³)↔(water surface elevation, m) relationship are taken from its final project documents (Sheets HD-001, HD-002, HD-003 in [17]). The numerical details of the routing of the PMF through the flood spillway are not given in the final project, except for a table of 5-step operation of releases from the existing radial-gated ogee spillway (HD-003 in [17]). The operation steps given in that table are rewritten here in Table 1.

Table 1 - Discharges to be released during routing of the PMF from Catalan Dam given in Sheet HD-003 in [17]

Range of water surface elevation (WSE) (m)	Spillway discharge to be released (m ³ /s)
118.60 < WSE ≤ 125.15	1200
125.15 < WSE ≤ 125.30	2500
125.30 < WSE ≤ 125.45	4000
125.45 < WSE ≤ 125.60	6000
125.60 < WSE ≤ 126.50	6500

Next, using the developed computer program, the length of the alternative ungated ogee spillway is computed. The flowrates of the PMF are taken from its final project at 4 hour steps, and the intermediate discharges at time steps of 0.2 hour are computed by third-degree polynomials fitted to every four sequential values surrounding the interpolated value and typed in the input data file. Although the initial estimate for the design discharge of the spillway is equal to $(0.7) \times 10,055$, which is 7038 m³/s, the final spillway design discharge turns out to be: $Q_{\text{design}} = 6629$ m³/s, and the length of the ungated ogee spillway is computed to be 141 m. The water surface elevation at the arrival of the design flood hydrograph, which is the PMF for this dam, is 118.6 m and the spillway design head is 8.0 m. The maximum water surface elevation reached during routing of the PMF from the reservoir with the design spillway of length of 141 m turns out to be 126.46 m.

3.2. Outflow Hydrographs from Ungated Spillway and from Radial-Gated Spillway

Along with the design of the ungated ogee spillway alternative to the existing radial-gated ogee spillway for Catalan Dam, the 15-stage operation model put forth by Haktanir et al [16]

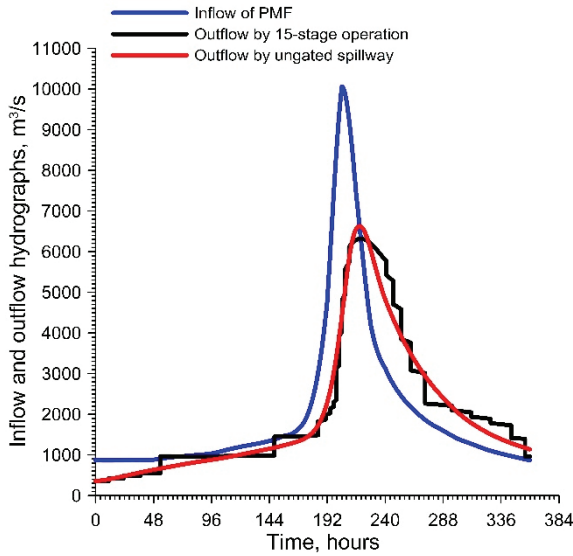


Figure 1 - Hydrographs of the incoming PMF and of the outflows (1) by the ungated ogee spillway and (2) by the existing radial-gated ogee spillway by the 15-stage operation model for Catalan Dam

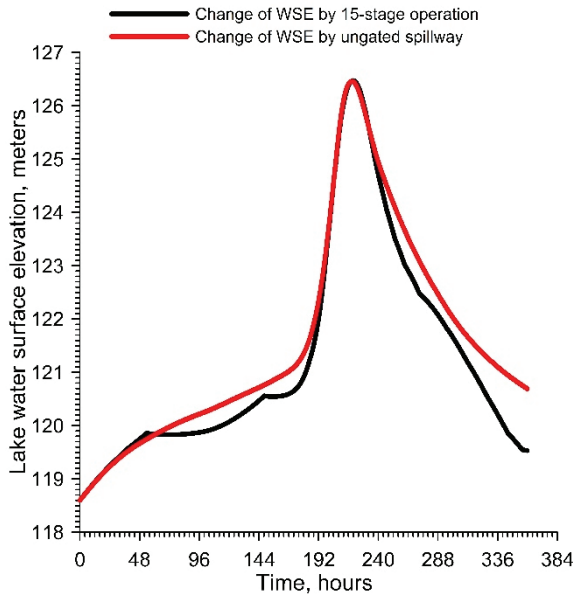


Figure 2 - Variations of the lake water surface elevations during routing of the PMF (1) by the ungated ogee spillway and (2) by the existing radial-gated ogee spillway by the 15-stage operation model for Catalan Dam

has been applied to Catalan Dam for routing of its PMF, also. The hydrographs of the PMF and of the outflows by the alternative ungated spillway and by the existing radial-gated spillway operated by the 15-stage operation model for Catalan Dam are given in Figure 1. The variations of the lake water surface elevation by routing of the PMF both by the ungated spillway and by the 15-stage operation model over the time base of the PMF are given in Figure 2. Coincidentally, routings of the PMF both by the ungated spillway and by the existing radial-gated spillway by the 15-stage operation model turn out to be fairly close to each other. The peaks of the outflow hydrographs by the ungated spillway and by the existing radial-gated spillway operated by the 15-stage operation model are $6629 \text{ m}^3/\text{s}$ and $6315 \text{ m}^3/\text{s}$, and the maximum lake water surface elevations are 126.46 m and 126.48 m, respectively. In sheet HD-003 in its final project [17], these values are given as $6500 \text{ m}^3/\text{s}$ and 126.44 m. We have not been able to superpose the outflow hydrograph to form by the operation policy mentioned in the final project of Catalan Dam (Table 1) in Figure 1 because the relevant quantitative data are not given in the final project sheets [17].

4. CONCLUSION AND DISCUSSION

Using the charts for the spillway discharge coefficients in the *Spillways* chapter of the book: *Design of Small Dams* [1], a new iterative method is developed to determine the length of the ungated ogee spillway such that the maximum lake elevation reached during routing of the design flood hydrograph becomes equal to the pre-specified maximum allowed water surface elevation. This method simplifies the conventional trial-and-error procedure for computation of the spillway length because it yields both the spillway length and the outflow hydrograph in a single run of the coded computer program.

As for the limitations of the proposed methods, the correction factor for the negative effect of a possible submergence due to a drowned hydraulic jump for those cases where a chute channel downstream of the spillway does not exist and the hydraulic jump of the spilled water forms right at the toe of the spillway is missing for the spillway discharge of an ogee spillway of given length. Symbolizing this coefficient by C_{submrgnc} , actually C_{submrgnc} should be the fifth coefficient next to C_{aprn} in equation (2). Figure 9-28 of the book: *Design of Small Dams* [1] gives the chart for C_{submrgnc} . Lack of this factor from equation (2) should not be a serious drawback of the proposed method because most of the dams in Türkiye have long chute channels between the toe of the spillway and the energy dissipating structure and hence $C_{\text{submrgnc}} = 1.0$ for most dams, anyway. Yet, for slight submergences $C_{\text{submrgnc}} = 1.0$ also. In short, missing of C_{submrgnc} in equation (2) should not be a worrisome issue. However, it should be kept in mind that for small dams having no chute channels the first method presented here may yield slightly greater magnitudes for ogee spillway discharge.

It is a known fact that because of the existence of the gates, the apex elevation of a gated spillway is much lower than the top of the full active storage (maximum operation elevation for water supply purposes), and hence when the gates are opened and begun to be operated the net head over the spillway crest is already very high and in parallel with that the discharge of the spilled water also becomes a high value. Therefore, gated spillways discharge high magnitudes of flowrates because of high net heads, and consequently they need smaller lengths for higher discharges. The apex elevation of a free flow (ungated) spillway however must necessarily be equal to the top of the full active storage. The developed method and the

computer program executing it can be used to compare the financial costs of the ungated spillway and of the radial-gated spillway. For dams whose surcharge storages are fairly large, the length of the ungated spillway may not be too long. Hence, the total cost of the ungated spillway may become smaller than that of the shorter radial-gated spillway, because the sum of the costs of the concrete spillway unit, the steel gates, the motors, the hoisting mechanisms, the trunnion pins, and the anchorages and the support piers of the trunnions may outweigh the total cost of the ungated spillway. Besides, the operation and maintenance cost of a radial-gated spillway will also be much greater than that of an ungated spillway. A third advantage of the ungated spillway is that it does not require finding an optimum operation rule of gate openings during floods of any magnitudes.

The developed approach is applied to Catalan Dam on Seyhan River in Türkiye which yields accurate and reasonable results.

References

- [1] USBR (1987) *Design of Small Dams, Chapter 9 Spillways, C. Hydraulics of Control Structures*, 3rd edition, U.S. Department of the Interior, Bureau of Reclamation, U.S. Government Printing Office, Washington DC.
- [2] Sanko (2007) *Final Feasibility Report of Yedigöze Dam ve Hydro-Power Plant* (in Turkish), *Appendix-4: Hydraulic Design of the Flood Spillway*. Sanko Engineering and Consulting Company, Çetin Emeç Boulevard, 6th Street, No: 61/7, 06520 Balgat, Ankara, Turkey.
- [3] Temelsu (2007) *Final Design Project of the Bayramhacılı Dam (Civil Engineering Works), Chapter 3.1 Hydraulic Computations, 4. Flood Spillway* (in Turkish). Temelsu International Engineering Services Company, Çankaya, Ankara, Turkey.
- [4] DSİ (2006) *Circular 2006/1 Criteria for Determining Design Flood for Spillways of Dams* (In Turkish). General Directorate of State Water Works, Department of Dams and Hydropower Plants, Ankara, Türkiye.
- [5] Savage B M and Johnson M C (2001) Flow over Ogee Spillway: Physical and Numerical Model Case Study. *Journal of Hydraulic Engineering - ASCE*, 127(8), 640–649. [https://doi.org/10.1061/\(ASCE\)0733-9429\(2001\)127:8\(640\)](https://doi.org/10.1061/(ASCE)0733-9429(2001)127:8(640))
- [6] Chatila J G and Tabbara M (2004) Computational modeling of flow over an ogee spillway. *Computers & Structures*, 82(22), 1805–1812. <https://doi.org/10.1016/j.compstruc.2004.04.007>
- [7] Alhashimi S A (2013) CFD Modeling of Flow over Ogee Spillway by Using Different Turbulence Models. *International Journal of Scientific Engineering and Technology Research*, 02(15), 1682–1687.
- [8] Goharrizi F Z and Moghadam M A (2010) Evaluation of a Numerical Modeling for Flow over an OGEE Spillway. 8th *International River Engineering Conference, Shahid Chamran University*, 26–28 January 2010, Ahwaz, Iran, 1–10.
- [9] Salmasi F and Abraham J (2022) Discharge coefficients for ogee spillways. *Water Supply*, 22(5), 5376–5392. doi: 10.2166/ws.2022.129

- [10] Kocaer Ö and Yarar A (2020) Experimental and numerical investigation of flow over ogee spillway. *Water Resources Management*, 34(13), 3949–3965. <https://doi.org/10.1007/s11269-020-02558-9>
- [11] Fadafan M A and Kermani M-R H (2015) Modeling of flow over an ogee spillway using moving particle semi-implicit method. *E-proceedings of the 36th IAHR World Congress, 28 June – 3 July 2015, The Hague, The Netherlands*.
- [12] Yildiz A, Yarar A, Kumcu S Y, Marti A I (2020) Modeling of flow over an ogee spillway using moving particle semi-implicit method. *Applied Water Science*, 10:90. <https://doi.org/10.1007/s13201-020-1177-4>
- [13] Kumcu Ş Y, Kocabeyler M F, Özaydın V, Kökpınar M A (2010) *Physical Modeling Test Report of the Flood Spillway of Kavşak Dam (In Turkish)*. Publication number: 1005, Research and Quality Control Department, General Directorate of State Water Works, Ankara, Türkiye.
- [14] Daneshfaraz R, Ghaderi A, Abraham J, Torabi M (2021) Effect of Different Channels on Discharge Coefficient of Labyrinth Weirs. *Teknik Dergi*, 32(4), 11081–11096. <https://doi.org/10.18400/tekderg.629128>
- [15] Şentürk F (1994) *Hydraulics of Dams and Reservoirs*. Water Resources Publications, PO Box 260026, Highlands Ranch, Colorado, 80126-0026, USA.
- [16] Haktanir T, Citakoglu H, Acanal N (2013) Fifteen-stage operation of gated spillways for flood routing management through artificial reservoirs. *Hydrological Sciences Journal*, 58(5), 1013–1031. <http://dx.doi.org/10.1080/02626667.2013.796431>
- [17] DSİ (1987) *Final Project of Catalan Dam (In Turkish)*. General Directorate of State Water Works, Department of Dams and Hydropower Plants, Ankara, Türkiye.

Seismic Assessment of Electrical Equipment in Power Substations: A Case Study for Circuit Breakers[†]

Discussion by Eray BARAN*



ABSTRACT

Remarks are provided on the paper “Seismic assessment of electrical equipment in power substations: a case study for circuit breakers” by Kaatsız et al. on how allowable stresses are determined for steel framing members forming the support structure as well as the connection elements used in various parts of electrical devices.

Keywords: Seismic assessment, electrical equipment, seismic qualification.

INTRODUCTION

In their paper [1], the authors present a case study on seismic assessment of electrical equipment according to the new Turkish regulation. There are two issues in the paper that need further discussion. The first issue relates to the structural capacity of steel members that make up the device’s support structure, while the second one concerns the capacity of connection elements, i.e., bolts and anchor rods. The subject paper is intended to serve as a guide for those who will use the new national code for seismic qualification assessment of electrical equipment. Therefore, it is crucial to clarify the issues related to the methods employed in the paper to ensure that such assessments are performed correctly.

CAPACITY OF STEEL MEMBERS

The paper adopts an approach where the stresses generated in various parts of the device under seismic and other applicable load effects are compared to the stress limits of the respective materials. While this approach is generally consistent with the allowable stress design method, it is crucial to understand how the allowable stress limits are determined. The authors seem to use the yield strength, reduced by a safety factor, as the allowable stress. Although this approach is correct for strength limit states associated with material yielding, it does not represent the actual strength of members in cases where other strength limit states are more critical. Therefore, it may lead to unsafe decisions regarding the seismic qualification of the device under evaluation. In the paper, the allowable stress for the steel members that make up the device’s support structure are determined by dividing the material yield strength by a safety factor of 1.67, by referring to the Turkish Steel Design Code [2]. With the assumptions that these members are subjected to only axial load and have bolted

[†] Kaan KAATSIZ, Fırat Soner ALICI, Murat Altuğ ERBERİK, Turkish Journal of Civil Engineering, Volume 35, Issue 4, July 2024. 49-68, Paper 775.

* Middle East Technical University, Department of Civil Engineering, Ankara, Türkiye
erayb@metu.edu.tr - <https://orcid.org/0000-0002-0240-803X>

connections at their ends, other applicable strength limit states that could determine the load capacity of such members are buckling, net section fracture, block shear, bearing, and tear out [2,3]. If there are additional bending moments present in members and/or if the members have welded connections at their ends, a different set of strength limit states would apply. In such cases, capacity corresponding to each limit state should be calculated for each steel member in the support structure. The smallest of these capacities, combined with the correct safety factor, should be used as the capacity of each member in seismic qualification assessment of the device.

Procedures to determine the capacity of steel structural members are provided in the Turkish Steel Design Code [2]. Chapter 7 relates to axial tensile capacity, Chapter 8 relates to axial compressive capacity, Chapter 9 relates to bending moment capacity, and Chapter 11 relates to the interaction between axial force and bending moment. For tensile members nominal axial force capacity corresponding to the limit state of net section fracture is determined with Eqn. 1. Nominal axial force capacity of compression members is determined with Eqn. 2. In these equations, F_u is tensile strength of steel, A_e is effective net section area, F_{cr} is critical buckling stress, and A_g is gross cross sectional area.

$$T_n = F_u \cdot A_e \quad (1)$$

$$P_n = F_{cr} \cdot A_g \quad (2)$$

For members under combined axial force and bending moment, interaction between these effects should be considered by using Eqn. 3. In this equation F_{ca} is the axial stress capacity determined according to Eqn. 1 for tensile axial force and Eqn. 2 for compressive axial force, F_{cbw} and F_{cbz} represent, respectively the strong axis and weak axis bending stress capacities. Nominal bending moment capacity of members with a single angle cross section is taken as the smaller of the capacities from Eqns. 4-6. In these equations, M_y is yield moment capacity and M_{cr} is elastic lateral torsional capacity.

$$\left| \frac{f_{ra}}{F_{ca}} + \frac{f_{rbw}}{F_{cbw}} + \frac{f_{rbz}}{F_{cbz}} \right| \leq 1.0 \quad (3)$$

$$M_n = 1.5M_y \quad (4)$$

$$M_n = \left[1.92 - 1.17 \sqrt{\frac{M_y}{M_{cr}}} \right] M_y \quad (5)$$

$$M_n = \left[0.92 - 0.17 \sqrt{\frac{M_y}{M_{cr}}} \right] M_{cr} \quad (6)$$

CAPACITY OF STEEL CONNECTION ELEMENTS

The second issue that needs to be addressed concerns the allowable stress of connection elements, i.e., bolts and anchor rods. In the paper allowable stress values for these elements are determined by dividing the material yield strength by a safety factor of 2.0. However, as

stated in current steel design codes [2,3], material yielding is not considered a strength limit state for these elements; instead, their capacities should be determined based on the fracture limit state. Furthermore, for the type of electrical equipment studied in the paper, significant shear forces usually develop in connection elements, in addition to tensile axial force. In such cases, evaluating the structural safety of these elements considering only tensile forces would lead to unsafe conclusions. The correct approach to determine the safety of connection elements should account for the interaction between shear and tensile axial forces and consider the fracture limit state under both effects.

Structural capacity calculation of steel connection elements and connected parts is outlined in Chapter 13 of the Turkish Steel Design Code [2]. Accordingly, nominal tensile and shear force capacities for bolts and anchor rods are determined with Eqns. 7 and 8, respectively. In the presence of combined tension and shear force, interaction defined by Eqn. 9 should be utilized. In these equations, F_{nt} is nominal tensile strength, F_{nv} is nominal shear strength, f_{rt} and f_{rv} are, respectively tensile and shear stresses on the bolt, A_b is unthreaded cross-sectional area, and Ω is factor of safety, which has a value of 2.

$$R_{nt} = F_{nt} \cdot A_b \quad (7)$$

$$R_{nv} = F_{nv} \cdot A_b \quad (8)$$

$$\frac{\Omega \cdot f_{rt}}{F_{nt}} + \frac{\Omega \cdot f_{rv}}{F_{nv}} \leq 1.3 \quad (9)$$

Block shear, bearing and tear out are other connection related strength limit states that should be taken into account when determining the axial force capacity of steel members. Nominal block shear capacity is determined with Eqn. 10, where A_{gv} , A_{nv} and A_{nt} are respectively gross shear area, net shear area and net tension area, U_{bs} is shear lag coefficient. Capacity corresponding to bearing and tear out around bolt holes is determined with Eqn. 11. In this equation, l_c is clear distance in the direction of force between two holes or between a hole and edge of the member, t is thickness of the member, d is bolt diameter.

$$R_n = 0.6F_u \cdot A_{nv} + U_{bs} \cdot F_u \cdot A_{nt} \leq 0.6F_y \cdot A_{gv} + U_{bs} \cdot F_u \cdot A_{nt} \quad (10)$$

$$R_n = 1.2l_c \cdot t \cdot F_u \leq 2.4d \cdot t \cdot F_u \quad (11)$$

References

- Kaatsız K., Alıcı F.S., Erberik M.A. Seismic assessment of electrical equipment in power substations: a case study for circuit breakers. Turkish Journal of Civil Engineering, 49-68, 2024.
- Code on Design, Calculation, and Construction Principles of Steel Structures. Republic of Türkiye Ministry of Environment and Urbanization, 2018.
- ANSI/AISC 360-22 Specification for Structural Steel Buildings. American Institute of Steel Construction, 2022.

Authors' Closure

ABSTRACT

This reply provides clarification following comments by Eray Baran on our recent paper in Turkish Journal of Civil Engineering, 49-68 [2024] titled as “Seismic Assessment of Electrical Equipment in Power Substations: A Case Study for Circuit Breakers”.

Keywords: Seismic assessment, electrical equipment, power station, circuit breaker, seismic qualification.

1. INTRODUCTION

First, the authors of the article would like to thank Dr. Eray Baran for his comments on the paper titled “*Seismic Assessment of Electrical Equipment in Power Substations: A Case Study for Circuit Breakers*” [1].

Baran [2] stated that there are two issues in the paper that need further discussion. The first issue relates to the structural capacity of steel members that make up the device’s support structure, while the second concerns the capacity of connection elements, i.e., bolts and anchor rods. The next two sections in the paper are devoted to responding to the issues raised by the author. The last section gives the final remarks. We hope that the replies clarify the issues related to the methods employed in the paper, ensure that such assessments are performed correctly, and serve as an additional guide for those who will use the new national code for the seismic qualification assessment of electrical equipment [3].

The scope of our paper [1] is primarily focused on calculations performed for the seismic qualification of the high-voltage hardware itself rather than the structural system. To maintain focus and brevity, we concentrated our discussion on the stress demands of these critical components. It should be noted that the seismic qualification study was performed for all the subcomponents of the circuit breakers presented in the paper by considering the failure modes for steel members and anchors. In this reply, the discussion is expanded to include these calculations to address the issues raised by Baran [2].

2. CAPACITY OF STEEL MEMBERS

In response to the statements in Kaatsiz et al. [1], Baran [2] stated that, although employing the yield strength reduced by a safety factor as the allowable stress is correct for strength limit states associated with material yielding, it does not represent the actual strength of members in cases where other strength limit states are more critical. Therefore, this approach may lead to unsafe decisions regarding the seismic qualification of the device under evaluation. Other applicable strength limit states that can determine the load capacity of such members have been listed as buckling, net section fracture, block shear, bearing, and tear-out. The author defines the appropriate procedure as follows: First, the capacity corresponding to each limit state should be calculated for each steel member in the support

structure. Then, the smallest of these capacities, combined with the correct safety factor, should be used as the capacity of each member in the seismic qualification assessment of the device.

As discussed, the capacity checks for the steel members constituting the support structure were performed during the seismic qualification study; however, the obtained results were omitted from the paper [1] for reasons previously explained. For explanatory purposes, we present the results for the 1-pole circuit breaker. The allowable tensile strength and the computed maximum tensile load demands on the steel members constituting the support structure are provided in Table 1.

Table 1 - Comparison of allowable tensile strength and maximum loads of steel members in the support structure

Steel Member	Allowable Tensile Strength (kN)	Maximum Tensile Load (kN)
80x80x8 mm	171.7	141.8
65x65x5 mm	60.0	27.1
60x8 mm	31.1	9.6

Similarly, maximum compressive load demands on these members are compared with their corresponding capacities in Table 2. It was determined that inelastic buckling behavior is expected for the steel sections given in Table 2 due to the relatively short spans of the support structure. It should be noted that 60x8 mm steel members exhibit negligible compressive load demands; hence, allowable compressive load comparisons were not performed for these members. The compressive load demands were determined to be well under the calculated allowable capacities.

Table 2 - Comparison of allowable compressive strength and maximum loads of steel members in the support structure

Steel Member	Allowable Compressive Load Capacity (kN)	Maximum Compressive Load (kN)
80x80x8 mm	159.8	132.7
65x65x5 mm	168.6	52.1

The combined effects of axial load and bending moment demands calculated according to the Turkish Steel Design Code [4] were also computed, and their interaction was evaluated as discussed by Baran [2]. The results are presented in Table 3 for the most critical angle sections of the steel support structures (80x80x8 mm), where the bending moment demands are greatest. The tensile load and compression load effects were considered separately. Consequently, the investigated members are determined to be safe under the combined interaction of axial loads and bending moments.

Table 3 - Evaluation for the effects of combined axial load and bending moment (≤ 1.0) on 80x80x8 mm angle section steel members in the support structure

Steel Member	For Tensile Axial Force	For Compressive Axial Force
80x80x8 mm	0.8	0.9

The force demands presented in Tables 1–3 were calculated by considering the most critical load demands determined according to the load combinations utilized in our paper [1]. They represent the combined effect of seismic, service, and dead loads acting on the hardware. It can be deduced that the structural members of the steel support are safe when analyzed using the allowable stress design approach, as detailed in contemporary steel design codes [4, 5]. This conclusion is expected in light of the results detailed in our study such that the highest stress demands are observed in the terminal regions of high voltage hardware due to the cantilever behavior of the whole system under seismic action [1]. The steel support structures experience lower strain compared to the porcelain equipment.

3. CAPACITY OF STEEL CONNECTION ELEMENTS

The second issue raised by the author that needs to be addressed relates to the allowable stress of connection elements, i.e., bolts and anchor rods. Dr. Baran states that material yielding is not considered a strength limit state for steel connection elements; instead, their capacities should be determined based on the fracture limit state, as stated in current steel design codes [4, 5]. Furthermore, for the type of electrical equipment studied in the paper, significant shear forces usually develop in connection elements, in addition to tensile axial forces. The author adds that, in such cases, evaluating the structural safety of these elements while considering only tensile forces could lead to unsafe conclusions. Hence, the author proposes the correct approach to determine the safety of connection elements as accounting for the interaction between shear and tensile axial forces and considering the fracture limit state under both effects.

The bolts connecting the sections in the steel support structure are of the M16-8.8 type. Shear forces predominantly act on the connections within the support structure due to the response characteristics of the system under the applied loads. Therefore, shear capacities for the bolts and block shear capacities for the bolted connections in the support structure were checked, and the results are given in Tables 4-5. As shown in the comparison of demands and shear force capacities, the bolted connections of the support structure are determined to be safe under the considered loading.

The circuit breaker hardware (porcelain isolator) is attached to the steel support structure via a connection plate secured by four M24-8.8 type bolts at its four edges, as detailed in our paper [1]. The circuit breaker mechanism and the porcelain isolator hardware are connected to each other and deform as a cantilever structure under the considered loading. As a result, axial and shear forces develop in the M24-8.8 bolts due to bending moment demands at the base of the hardware. The resulting loads and the corresponding capacities for these bolts are compared in Table 6. The computed coefficient representing the interaction between these

loads [2] is also provided in Table 6. Based on the results, the seismic performance of the connection bolts is determined to be satisfactory.

Table 4 - Capacity evaluation of M16-8.8 connection bolts in the support structure

Connection	Allowable Shear Capacity (kN)	Maximum Shear Load (kN)
Between 80x80x8 mm and 65x65x5 mm steel members	144.8	52.1
Between 80x80x8 mm and 60x8 mm steel members	36.2	20.9

Table 5 - Evolution of block shear capacity of M16-8.8 connection bolts in the support structure

Connected Steel Member	R _n (kN)	Maximum Load (kN)
80x80x8mm	109.6	10.0
65x65x5 mm	29.2	27.0

Table 6 - Capacity evaluation of M24-8.8 bolts in the isolator connection plate

Connection	R _{nt} (kN)	R _{nv} (kN)	f _{rt} (kN)	f _{rv} (kN)	Check (≤ 1.3)
Isolator connection plate	271.4	162.9	5.91	74.4	0.96

We consider that the capacity checks presented in Tables 4-6 are expected to be satisfied for a structure that is designed through a structural design by considering the contemporary steel design codes and associated seismic load requirements. The failure modes for connections and bolts are checked for possible failure modes and the resulting bolt dimensions are determined accordingly during the design phase of the high voltage hardware. Therefore, the satisfactory performance in terms of seismic qualification requirements is within the expectations of the authors.

4. FINAL REMARKS

Following the discussions in the previous sections, we would like to conclude that the seismic performance of the circuit breakers inspected in the scope of our study is satisfactory in light of the issues raised in the discussion paper [2]. It should also be noted that structural components, such as steel sections or connections of high-voltage equipment, are designed by utilizing contemporary steel design codes under the combined action of several load cases, such as dead, service, wind, and seismic action. Therefore, it is reasonable to expect that these components will easily satisfy the seismic qualification criteria. The same conclusion may not apply to high-voltage hardware, such as porcelain insulators or circuit breaker

mechanisms, as they are designed and manufactured for electromechanical requirements rather than load cases such as seismic action. Hence, evaluating the stress demands on this hardware under seismic loads may deserve a priority over regular capacity checks for structural steel components from seismic qualification perspective. Otherwise, this may shift the focus away from the critical components while performing a seismic qualification study.

We acknowledge that the allowable capacity controls stated in the discussion paper [2] should indeed be performed for structural components of high-voltage equipment. We also consider that the main focus of a seismic qualification study, from an academic point of view, is the investigation of the stress demands on high-voltage components under the considered seismic actions. In light of this perspective, the main objective of our paper [1] was to document a systematic approach, as outlined in TEC-PS [3], to compute and compare the seismicity induced stress demands on electromechanical hardware with allowable capacities within the limited length of the manuscript. We would like to extend our thanks again to the author of the discussion paper [2] for giving us the opportunity to provide further results from our study and clarify specific points about our research.

References

- [1] Kaatsız K., Alıcı F.S., Erberik M.A. Seismic assessment of electrical equipment in power substations: a case study for circuit breakers. *Turkish Journal of Civil Engineering*, 49-68, 2024.
- [2] Baran E. Comment on Seismic assessment of electrical equipment in power substations: a case study for circuit breakers. *Turkish Journal of Civil Engineering*, to be published.
- [3] General Directorate of Highways. Sector B2-B3: Distribution Facilities and Systems. Electricity Power Transmission and Telecommunication Systems. Technical Report prepared by Yuksel Project and submitted to Turkish Republic Ministry of Transport and Infrastructure General Directorate of Highways Department of Structures, Ankara Turkey, 2019.
- [4] Code on Design, Calculation, and Construction Principles of Steel Structures. Republic of Türkiye Ministry of Environment and Urbanization, 2018.
- [5] ANSI/AISC 360-22 Specification for Structural Steel Buildings. American Institute of Steel Construction, 2022.

Turkish Journal of Civil Engineering (formerly Teknik Dergi)

Manuscript Drafting Rules

1. The whole manuscript (text, charts, equations, drawings etc.) should be arranged in Word and submitted in ready to print format. The article should be typed on A4 (210 x 297 mm) size paper using 10 pt (main title 15 pt) Times New Roman font, single spacing. Margins should be 40 mm on the left and right sides and 52.5 mm at the top and bottom of the page.
2. Including drawings and tables, articles should not exceed 25 pages, technical notes 10 pages.
3. Your contributed manuscript must be sent over the DergiPark system. (<http://dergipark.gov.tr/tekderg>)
4. The text must be written in a clear and understandable language, conform to the grammar rules. Third singular person and passive tense must be used, and no inverted sentences should be contained.
5. Title must be short (10 words maximum) and clear, and reflect the content of the paper.
6. Sections should be arranged as: (i) abstract and keywords, (ii) title, abstract and keywords in the other language, (iii) main text, (iv) symbols, (v) acknowledgements (if required) and (vi) references.
7. Both abstracts should briefly describe the object, scope, method and conclusions of the work and should not exceed 100 words. If necessary, abstracts may be re-written without consulting the author. At least three keywords must be given. Titles, abstracts and keywords must be fitted in the first page leaving ten line space at the bottom of the first page and the main text must start in the second page.
8. Section and sub-section titles must be numbered complying with the standard TS1212.
9. Symbols must conform to the international rules; each symbol must be defined where it appears first, additionally, a list of symbols must be given in alphabetic order (first Latin, then Greek alphabets) at the end of the text (before References).
10. Equations must be numbered and these numbers must be shown in brackets at the end of the line.
11. Tables, drawings and photographs must be placed inside the text, each one should have a number and title and titles should be written above the tables and below the drawings and photographs.
12. Only SI units must be used in the manuscripts.
13. Quotes must be given in inverted commas and the source must be indicated with a reference number.
14. Acknowledgement must be short and mention the people/ institutions contributed or assisted the study.
15. References must be numbered (in brackets) in the text referring to the reference list arranged in the order of appearance in the text. References must include the following information:

If the reference is an article: Author's surname, his/her initials, other authors, full title of the article, name of the journal, volume, issue, starting and ending pages, year of publication.

Example : Naghdi, P. M., Kalnins, A., On Vibrations of Elastic Spherical Shells. J. Appl. Mech., 29, 65-72, 1962.

If the reference is a book: Author's surname, his/her initials, other authors, title of the book, volume number, editor if available, place of publication, year of publication.

Example : Kraus. H., Thin Elastic Shells, New York. Wiley, 1967.

If the reference is a conference paper: Author's surname, his/her initials, other authors, title of the paper, title of the conference, location and year.

If the source is a thesis: Author's surname, his/her initials, thesis title, level, university, year.

If the source is a report: Author's surname, his/her initials, other authors, title of the report, type, number, institution it is submitted to, publication place, year.
16. Discussions to an article published in Turkish Journal of Civil Engineering (formerly Teknik Dergi) should not exceed two pages, must briefly express the addressed points, must criticize the content, not the author and must be written in a polite language. Authors' closing remarks must also follow the above rules.
17. A separate note should accompany the manuscript. The note should include, (i) authors' names, business and home addresses and phone numbers, (ii) brief resumes of the authors and (iii) a statement "I declare in honesty that this article is the product of a genuinely original study and that a similar version of the article has not been previously published anywhere else" signed by all authors.
18. Copyright has to be transferred to UCTEA Turkish Chamber of Civil Engineers. The standard copyright form signed by the authorised author should therefore be submitted together with the manuscript.

CONTENTS

RESEARCH ARTICLE

Comparative Analysis of Frequency Ratio, Logistic Regression and Deep Learning Methods for Landslide Susceptibility Mapping in Tokat Province on the North Anatolian Fault Zone (Turkey) 1

Ayhan BAŞALAN, Gökhan DEMİR

Earthquake Performance Analysis of a Masonry School Building's Retrofitted State by the Equivalent Frame Method 29

Vefa OKUMUS, Atakan MANGİR

Mixed Finite Elements for Higher-order Laminated Cylindrical and Spherical Shells 51

Yonca BAB, Akif KUTLU

A Critical Evaluation of the Coefficient Method, Capacity Spectrum Method and Modal Pushover Analysis for Irregular Steel Buildings in Seismic Zones 75

Vahid MOKARRAM, Mahmoud Reza BANAN, Mohammad Reza BANAN, Abdollah KHEYRI

TECHNICAL NOTE

Determination of Ungated Ogee Spillway Length so as to Pass Design Flood Safely 109

Tefaruk HAKTANIR

DISCUSSION

Seismic Assessment of Electrical Equipment in Power Substations: A Case Study for Circuit Breakers 123

Discussion by Eray BARAN



UCTEA Turkish Chamber of Civil Engineers
TMMOB İnşaat Mühendisleri Odası
Necatibey St. No: 57, Kızılay, Ankara / Türkiye
Tel: +90.312.294 30 00 - Faks: 294 30 88
imo@imo.org.tr - www.imo.org.tr